

N 70 28729

SPACE RESEARCH COORDINATION CENTER



NASA CR 110189

DEFORMATION OF THE GROUPS IVB
AND VB MONOCARBIDES

CASE FILE
COPY
BY

WILLIAM F. BRIZES

DEPARTMENT OF
METALLURGICAL/MATERIALS ENGINEERING

SRCC REPORT NO. 117

NG1-39-011-002
✓ UNIVERSITY OF PITTSBURGH

PITTSBURGH, PENNSYLVANIA

6 FEBRUARY 1970

The Space Research Coordination Center, established in May, 1963, has the following functions: (1) it administers predoctoral and postdoctoral fellowships in space-related science and engineering programs; (2) it makes available, on application and after review, allocations to assist new faculty members in the Division of the Natural Sciences and the School of Engineering to initiate research programs or to permit established faculty members to do preliminary work on research ideas of a novel character; (3) in the Division of the Natural Sciences it makes an annual allocation of funds to the interdisciplinary Laboratory for Atmospheric and Space Sciences; (4) in the School of Engineering it makes a similar allocation of funds to the Department of Metallurgical and Materials Engineering and to the program in Engineering Systems Management of the Department of Industrial Engineering; and (5) in concert with the University's Knowledge Availability Systems Center, it seeks to assist in the orderly transfer of new space-generated knowledge in industrial application. The Center also issues periodic reports of space-oriented research and a comprehensive annual report.

The Center is supported by an Institutional Grant (~~NSG-416~~) from the National Aeronautics and Space Administration, strongly supplemented by grants from the A. W. Mellon Educational and Charitable Trust, the Maurice Falk Medical Fund, the Richard King Mellon Foundation and the Sarah Mellon Scaife Foundation. Much of the work described in SRCC reports is financed by other grants, made to individual faculty members.

DEFORMATION OF THE GROUPS IVB AND VB MONOCARBIDES

by

William F. Brizes

B.S. in Met.E., Case Institute of Technology, 1962

M.S. in Met.E., University of Pittsburgh, 1968

Submitted to the Graduate Faculty
of the School of Engineering
in partial fulfillment of
the requirements for the degree of
Doctor
of
Philosophy
University of Pittsburgh
1969

The author grants permission
to reproduce single copies.

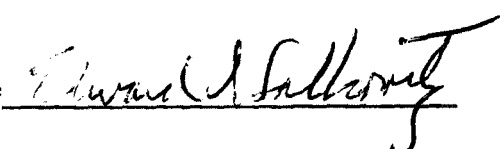
William F. Brizes

Signed

ACKNOWLEDGEMENTS

The author expresses his appreciation to the Bevier Fund which financially supported his fellowship, to E.F.Vandergrift and P.S.Gaal who assisted in the acquisition of mechanical and thermal expansion data and to Dr.E.I.Salkovitz, Chairman of the Department of Metallurgical and Materials Engineering, who was his dissertation advisor.

ABSTRACT

Signature 

DEFORMATION OF THE GROUPS IVB AND VB MONOCARBIDES

William F. Brizes, Ph.D.

University of Pittsburgh, 1969

The creep behavior of the Groups IVB and VB carbides was studied in terms of a stress dependent activation energy on one hundred percent dense samples made by liquid state carburization. The stress corrected activation energy for NbC was determined to be 155 kcal per mole in agreement with the estimated activation energy for self-diffusion of niobium in NbC. Internal stresses were determined from stress relaxation measurements and the ratio of the internal stress to the applied stress was 0.78 for steady state creep at 2220°C. For constant strain rate experiments internal stress increased in proportion to the square root of strain. Activation areas were approximately equal to $80\bar{b}^2$ and $400\bar{b}^2$ at 0.6m.p. and 0.9m.p. respectively. Other properties investigated were thermal expansion, yield stress and room temperature hardness as a function of stoichiometry.

DESCRIPTORS

Activation Energy, Carbides, Creep, Hardness, Thermal Expansion
Yield Stress

TABLE OF CONTENTS

ACKNOWLEDGEMENTS.....	ii
ABSTRACT.....	iii
LIST OF FIGURES.....	vii
LIST OF TABLES.....	x
LIST OF SYMBOLS.....	xii
1.0 INTRODUCTION.....	1
2.0 MATERIALS.....	3
2.1 Preparation.....	3
2.2 Apparatus.....	7
2.21 Graphite Mold.....	7
2.22 Graphite Crucible.....	12
2.23 Induction Furnace.....	12
2.24 Radio-Frequency Power Source.....	14
3.0 CARBIDE CHARACTERIZATION.....	16
3.1 Structure.....	16
3.2 Room Temperature Hardness.....	25
3.3 Thermal Expansion.....	30
3.31 Sample Preparation.....	30
3.32 Apparatus.....	33
3.33 Results and Discussion.....	33
3.4 Long-Range Ordering.....	43

4.0 HIGH TEMPERATURE DEFORMATION.....	46
4.1 Introduction.....	46
4.2 Yield Stress Behavior.....	46
4.21 Introduction.....	46
4.22 Apparatus and Procedure.....	49
4.23 Results and Discussion.....	50
4.3 Activation Area.....	61
4.31 Introduction.....	61
4.32 Apparatus and Procedure.....	63
4.33 Results and Discussion.....	64
4.4 Constant Load Creep.....	76
4.41 Introduction.....	76
4.42 Apparatus and Procedure.....	77
4.43 Results and Discussion.....	77
5.0 MODEL FOR CONSTANT STRESS CREEP.....	83
6.0 APPLICATION OF MODEL TO NbC.....	91
6.1 Creep of NbC at Constant Stress.....	91
6.11 Introduction.....	91
6.12 Apparatus and Procedure.....	92
6.13 Results and Discussion.....	93
6.2 Determination of the Internal Stress.....	97
6.21 Introduction.....	97

6.22 Apparatus and Procedure.....	98
6.23 Results and Discussion.....	100
6.3 Determination of the Activation Energy ΔH	105
6.31 Results and Discussion.....	105
7.0 CONCLUSIONS.....	108
8.0 SUGGESTIONS FOR FUTURE WORK.....	111
APPENDIX A.....	112
BIBLIOGRAPHY.....	116

LIST OF FIGURES

Figure	Page
1. Parabolic Growth Constants for the Groups IVB and VB Monocarbides	6
2. Transmission Electron Micrograph of a Sub-Boundary in As-Grown Zirconium Carbide	10
3. Six Rod Crucible Assembly	11
4. Schematic of Carburization Furnace	13
5. Titanium-Carbon Phase Diagram	17
6. Zirconium-Carbon Phase Diagram	18
7. Hafnium-Carbon Phase Diagram	19
8. Vanadium-Carbon Phase Diagram	20
9. Niobium-Carbon Phase Diagram	21
10. Tantalum-Carbon Phase Diagram	22
11. The B1 Structure of MeC	23
12. The B8 Structure of Me ₂ C	24
13. Hardness of the Groups IVB and VB Monocarbides as a Function of Composition	27
14. Photomicrograph of Hardness Impressions in TaC Showing a Precipitation Phenomena Associated with Impressions Made at Low Stoichiometries	29
15. Electron Micrograph of Hardness Impression at Low Stoichiometry	29
16. Schematic of Brazing Apparatus	31
17. Thermal Expansion Test Specimen Configuration	32

LIST OF FIGURES CONTINUED

Figure	Page
18. Linear Thermal Expansion vs. Temperature for VC	34
19. Linear Thermal Expansion vs. Temperature for TiC	36
20. Linear Thermal Expansion vs. Temperature for ZrC	37
21. Linear Thermal Expansion vs. Temperature for HfC	38
22. Linear Thermal Expansion vs. Temperature for NbC	39
23. Linear Thermal Expansion vs. Temperature for TaC	40
24. Photomicrograph of a Portion of a Diffusion Couple between Vanadium Metal and Graphite Showing a Region of Long-Range Order in VC	44
25. Critical Resolved Shear Stress in VC as a Function of Carbon Composition from Hollox	48
26. Yield Stress of the Groups IVB and VB Monocarbides as a Function of Temperature	51
27. Temperature Dependence of the Log of Yield Stress from Hollox	53
28. Log of Yield Stress vs. Reciprocal Temperature for the Group IVB Monocarbides	55
29. Log of Yield Stress vs. Reciprocal Temperature for the Group VB Monocarbides	56
30. Log of Yield Stress vs. Temperature for the Group IVB Monocarbides	57
31. Log of Yield Stress vs. Temperature for the Group VB Monocarbides	58
32. Schematic of a Stress vs. Strain Curve for Determining Activation Areas	65

LIST OF FIGURES CONTINUED

Figure	Page
33. Activation Area for NbC Determined from Yield Stress Data	72
34. Determination of m from Yield Stress Data	75
35. Minimum Creep Rate after One Hour at Constant Load as a Function of Temperature	79
36. Minimum Creep Rate for VC after One Hour at Constant Load as a Function of Temperature	80
37. Total Creep Rate after One Hour at Constant Load as a Function of Temperature	81
38. Total Creep Rate for VC after One Hour at Constant Load as a Function of Temperature	82
39. Force vs. Distance for a Dislocation Showing Long-Range and Short-Range Stresses	85
40. Force vs. Distance Curve for a Dislocation	86
41. Force vs. Distance for a Dislocation as a Function of Strain	88
42. Schematic of a Differential Creep Test for NbC	94
43. Shear Modulus of NbC as a Function of Temperature	99
44. Stress Relaxation Curve for NbC	101
45. Determination of τ_i from Stress Relaxation Curve	102
46. Internal Stress as a Function of Strain	104
1A. Force Versus Distance Curve Showing Relationship Between ΔF , ΔQ and $V^* \gamma^*$	114
2A. Force Versus Distance Curve Showing the Stress Dependence of the Activation Volume	115

LIST OF TABLES

Table	Page
1. Carbon, Oxygen, Nitrogen and X-ray Analysis after Mechanical Testing	8
2. Spectrographic Analysis after Mechanical Testing	9
3. Least Squares Equation for Thermal Expansion of the Groups IVB and VB Monocarbides as a Function of Temperature	41
4. Average Coefficient of Thermal Expansion for the Groups IVB and VB Monocarbides	42
5. Yield Stress of TaC and TiC as a Function of Composition	60
6. Activation Areas as a Function of Temperature and Applied Stress for TiC	66
7. Activation Areas as a Function of Temperature and Applied Stress for ZrC	67
8. Activation Areas as a Function of Temperature and Applied Stress for HfC	68
9. Activation Areas as a Function of Temperature and Applied Stress for VC	69
10. Activation Areas as a Function of Temperature and Applied Stress for NbC	70
11. Activation Areas as a Function of Temperature and Applied Stress for TaC	71
12. Constant m Relating Stress and Strain Rate	74
13. Apparent Activation Energies for NbC Determined from Instantaneous Temperature Changes at Constant Stress	95

LIST OF TABLES CONTINUED

Table	Page
14. Internal Stresses in NbC Determined from Stress Relaxation Experiments	103

LIST OF SYMBOLS

\bar{b}	= Burgers vector
R	= rate constant
$\bar{\alpha}$	= average coefficient of thermal expansion
v	= dislocation velocity
v_o	= constant
γ	= shear stress
m	= constant
U	= activation energy
k	= Boltzmann constant
T	= temperature
K_1	= constant
A	= constant
B	= constant
ΔF_f	= change in free energy in the forward direction
ΔF_o	= total free energy
ΔF_b	= change in free energy in the backward direction
V^*	= activation volume
γ^*	= thermal component of the applied shear stress
P	= hydrostatic pressure
A^*	= activation area
L	= length of dislocation held up at a barrier

LIST OF SYMBOLS CONTINUED

d	= distance a dislocation must move to overcome a barrier
$\dot{\gamma}$	= strain rate
τ_A	= applied shear stress
K_2	= constant
K_3	= constant
τ_o	= constant
m^*	= constant
K_4	= constant
$\dot{\epsilon}$	= creep rate
ΔH	= stress independent activation energy
N	= number of pieces of dislocation likely to slip at any moment
A	= area swept out by a dislocation when it slips
ν	= frequency of vibration of the dislocation
ΔQ	= stress dependent activation energy
τ_i	= internal stress
ϵ	= strain
ρ	= dislocation density
θ	= slope of stress relaxation curve

1.0 INTRODUCTION

The transition metal carbides (TiC, ZrC, HfC, VC, NbC and TaC) are characterized by their extremes in melting temperatures, hardness, brittleness and high temperature strength. Melting temperatures of most of the carbides are in excess of 3000°C making them the most refractory materials known to man. Their room temperature hardness is exceeded only by a few materials such as diamond, boron carbide, aluminum boride and silicon carbide. Related to their unusual room temperature hardness is their extreme brittleness which persists up to approximately 1000°C . Above this temperature the carbides are the strongest materials currently available with the possible exceptions of graphite and tungsten-thoria alloys.

Brittleness, difficulty of fabrication, poor oxidation resistance and lack of reliable property data have limited their acceptance. However because of their unusual properties carbides are beginning to find useful applications in industry. They are widely used in cutting tools and extrusion dies where thoroughly characterized materials are not required. Chemical and nuclear rocket propulsion industries are using and developing uses for carbides as structural and cladding materials in applications where conventional materials would be molten. It is expected that carbides will play a more significant role

in high temperature technology as the efficiency of current processes is increased and as the aerospace industry develops.

This dissertation describes the mechanical behavior of the Groups IVB and VB carbides from room temperature to near their melting points. Unlike most of the previous investigations, this study was done on theoretically dense, high purity and well characterized specimens. This study investigated high temperature deformation of all the carbides, but was primarily concerned with the creep behavior of niobium carbide. Because high quality samples of carbides were available other properties were investigated such as hardness, thermal expansion and yield stress in order to develop an understanding of the behavior of the transition metal carbides.

2.0 MATERIALS

2.1 Preparation

There is little high quality mechanical property data available on transition metal carbides due primarily to lack of unsuitable test specimens. Presently there are six methods of producing carbide test specimens; (1) cold pressing and sintering, (2) hot pressing, (3) Verneuil technique, (4) zone melting, (5) solid state carburization and (6) liquid state carburization. Most of the early survey data on carbides were obtained in bending tests using cold pressed and sintered specimens and hot pressed specimens containing iron, free carbon, and greater than one percent porosity. It has been shown by Ryshkewitch^{(1)*} that a small amount of porosity in a ceramic has a major effect on strength; for example, ten percent porosity in Al_2O_3 reduces the strength by one-half. Thus specimens containing even a small amount of porosity are not completely satisfactory for measuring deformation properties of carbides. The first four methods usually involve starting with a fine powder which produces specimens susceptible to high impurity contents. The Verneuil technique can produce single crystals but they are imperfect and can contain free

*Parenthetical references placed superior to the line of text refer to the bibliography.

carbon. Zone melting has been shown⁽²⁾ to be an excellent method for producing some carbides of various compositions. The major difficulty associated with this method is vaporization during melting. It has been demonstrated⁽²⁾ that this difficulty can be overcome in vanadium and titanium carbide but it is not known whether high melting carbides such as tantalum and hafnium can be made by this technique. Solid state carburization appears novel in that complex test specimens can be made from premachined metal shapes. This method is limited to wire or thin sheet specimens because diffusion times for thicker specimens would be prohibitive. A major fault associated with this method is that the specimen surface usually contains cracks resulting from an approximately four percent linear expansion when converting the metal to a carbide. The last method, liquid state carburization, has the benefit of low impurity content since crystal bar or electron beam processed metal can be used directly. Surface cracks observed in specimens made by the solid state carburization method do not occur since the annealing temperature is high enough for stresses in the carbide to be relieved by plastic flow. An added advantage of liquid state carburization is that all six of the Groups IVB and VB monocarbides can be readily fabricated with one apparatus. Thus this method was chosen for fabrication of test specimens used in this study.

Specimens were made by heating transition metal rods in a mold made of ZTA graphite. During heating the metal rods melt and conform to the geometry of the mold. At the melting temperature the diffusivity of carbon in the melt is quite high so that the liquid metal becomes saturated with carbon from the mold wall in a few minutes. After the melt becomes saturated, carbon reacts with the liquid to form a solid layer of carbide at the graphite-liquid interface. The growth rate of the carbide layer is controlled by carbon diffusion. The parabolic rate constants, R , describing the growth rate as a function of temperature are given and defined in Figure 1. The rate constants can be used to approximate the time needed for complete carburization. Normally one to two weeks are needed at approximately 200°C below the carbide-carbon eutectic temperature to attain the desired stoichiometry. The carbide rods were easily removed from the mold due to recession of the graphite interface during the diffusion anneal. The resulting rods (six rods $3/8$ inch diameter by $2\frac{1}{2}$ inches long) were coarse grain, i.e., three to four grains across the diameter except for hafnium carbide which had approximately six grains. The rods were mounted in a hard wax and cut with a diamond cutoff wheel into compression specimens ($3/8$ inch diameter by $3/4$ inch long). Because specimens were made in a carbonaceous atmosphere, they had the highest possible carbon content in agreement

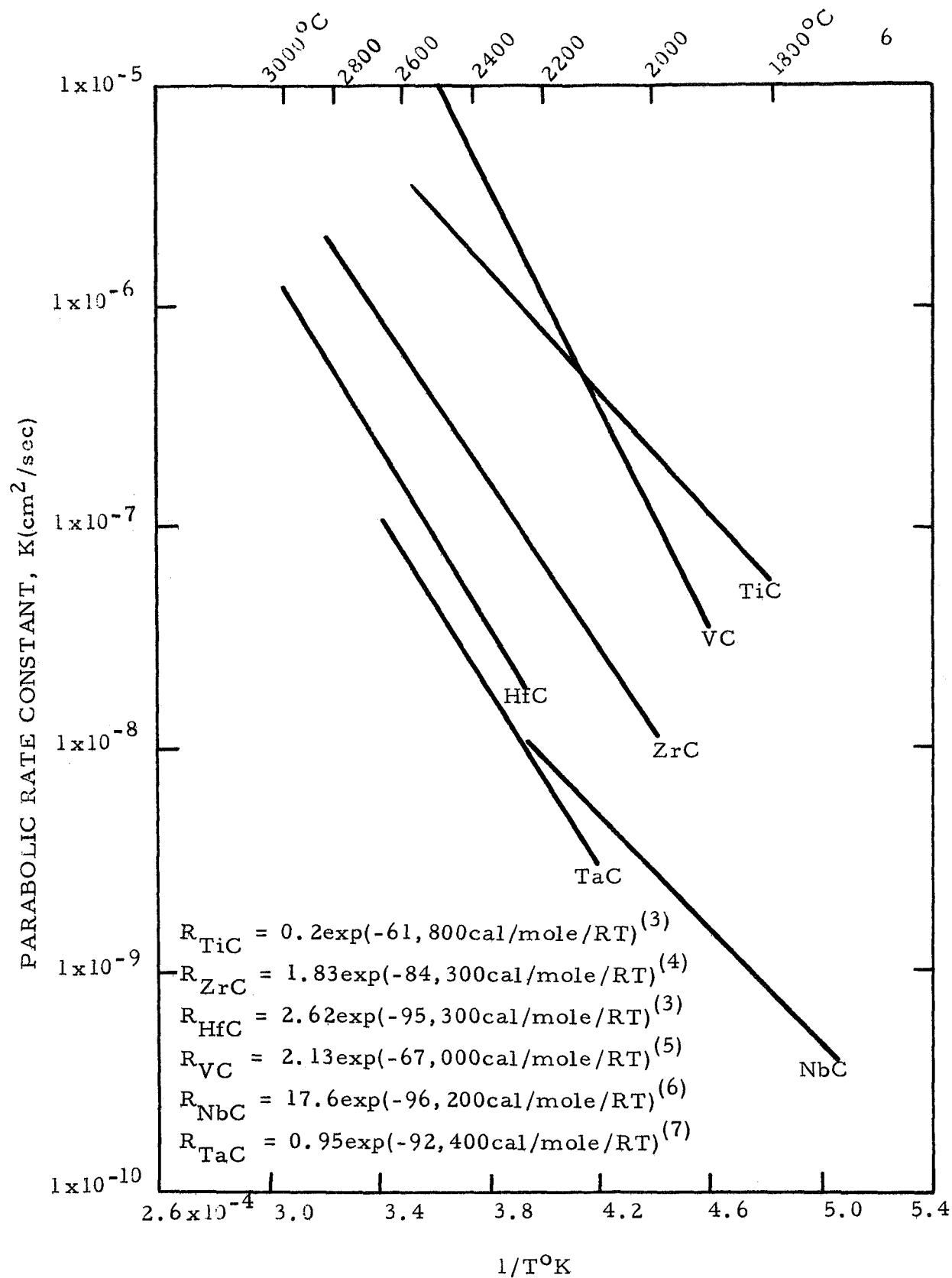


Figure 1. Parabolic Growth Constants for the Group IVB and VB Monocarbides ($R = w^2/t$, w = width of layer, t = time)

with the phase diagrams. Carbon analyses after mechanical testing are given in Table 1 together with the measured lattice parameters. Spectrographic analyses of specimens after testing are given in Table 2.

The carbides are inherently free of dislocations in the as-grown condition because of their high Peierls stress. An electron micrograph of a sub-boundary in zirconium carbide is shown in Figure 2. After a small amount of deformation the dislocation density is greatly increased as experienced in conventional metals.

2.2 Apparatus

2.2.1 Graphite Mold

Right cylindrical molds 0.490 inch O.D. by 2.75 inches long were made from ZTA graphite. A 2.625 inch deep flat-bottomed hole was drilled in the mold to receive the metal rods. Spiral grooves left by the drilling operation were removed by reaming to 0.375 inch I.D. Metal rods were fitted tightly into the molds to reduce the probability of forming bubbles in the resulting carbide rods. Because titanium, zirconium and vanadium metals wet graphite well a ZTA graphite plug in the entrance of the mold was used to contain the liquid metal. A schematic representation of the mold is shown in Figure 3.

TABLE 1
CARBON, OXYGEN, NITROGEN AND X-RAY
ANALYSIS AFTER MECHANICAL TESTING

	<u>Atomic % Carbon</u>	<u>O₂ (ppm)</u>	<u>N₂ (ppm)</u>	<u>a_o^o(Å)</u>	<u>M.P.[*] (°C)</u>
TiC	49.0	743	<20	4.3259	3,050
ZrC	49.7	25	"	4.6981	3,420
HfC	50.0	11	"	4.6421	3,830
VC	46.7	13	"	4.1655	2,750
NbC	49.2	9	"	4.4691	3,500
TaC	50.0	7	"	4.4534	4,000

* Melting temperatures are taken from Figures 5 through 10.

TABLE 2
SPECTROGRAPHIC ANALYSIS AFTER
MECHANICAL TESTING, PPM

	<u>TiC</u>	<u>ZrC</u>	<u>HfC</u>	<u>VC</u>	<u>NbC</u>	<u>TaC</u>
Ag	<3	18	22	< 2	< 3	< 3
Al	150	<10	<10	< 2	<10	< 10
B	---	4.0	< 1	240	< 1	< 1
Ba	<10	< 10	< 3	< 6	< 3	< 10
Be	< 3	< 0.3	< 0.3	< 0.6	< 0.3	< 0.3
Bi	<30	< 10	<30	< 60	< 10	<100
Ca	<10	< 10	< 3	< 60	< 10	< 10
Cd	<100	<100	<100	<600	< 100	< 300
Co	< 30	< 10	< 10	< 6	< 30	< 10
Cr	110	< 3	< 10	16	< 10	< 30
Cs	<100	<100	<100	< 200	< 100	< 100
Cu	6.7	< 3	< 3	< 6	< 10	< 3
Fe	1000	93	< 30	1280	< 13	< 10
Hf	---	96	---	---	---	---
In	<100	< 30	< 30	< 60	< 30	< 100
K	<10	< 30	< 10	< 20	< 3	< 30
Li	< 3	< 3	< 1	< 6	< 1	< 3
Mg	13	< 1	< 3	< 0.6	< 1	< 0.3
Mn	13	< 3	< 3	< 0.6	< 3	< 1
Mo	<30	18	22	<160	< 25	< 30
Na	< 3	<10	< 3	< 6	< 10	< 10
Nb	200	<30	<100	< 600	---	< 30
Ni	27	< 3	< 10	51	< 10	< 10
P	<300	<100	<100	< 200	<100	< 300
Pb	< 10	< 30	< 30	< 6	< 30	<100
Rb	< 30	<100	< 30	< 60	< 30	< 30
Sb	< 30	< 30	< 30	< 20	< 100	< 100
Si	110	< 10	< 10	160	< 10	< 3
Sn	40	< 10	< 30	< 6	< 30	< 30
Sr	< 3	< 30	< 10	< 60	< 30	< 100
Th	<100	< 30	<100	< 600	<100	<100
Ti	---	15	33	19	10	< 10
Ta	---	<300	---	---	< 300	---
V	1200	< 3	< 3	---	< 10	< 10
W	<100	<100	< 30	< 2000	<300	< 300
Zn	<100	<100	<100	< 60	<100	< 100
Zr	< 30	---	14500	< 200	250	< 3



Figure 2. Transmission Electron Micrograph of a Sub-Boundary in As-Grown Zirconium Carbide Indicating It Has a High Stacking Fault Energy Because of Little Dissociation at Dislocation Nodes, 23,000x.

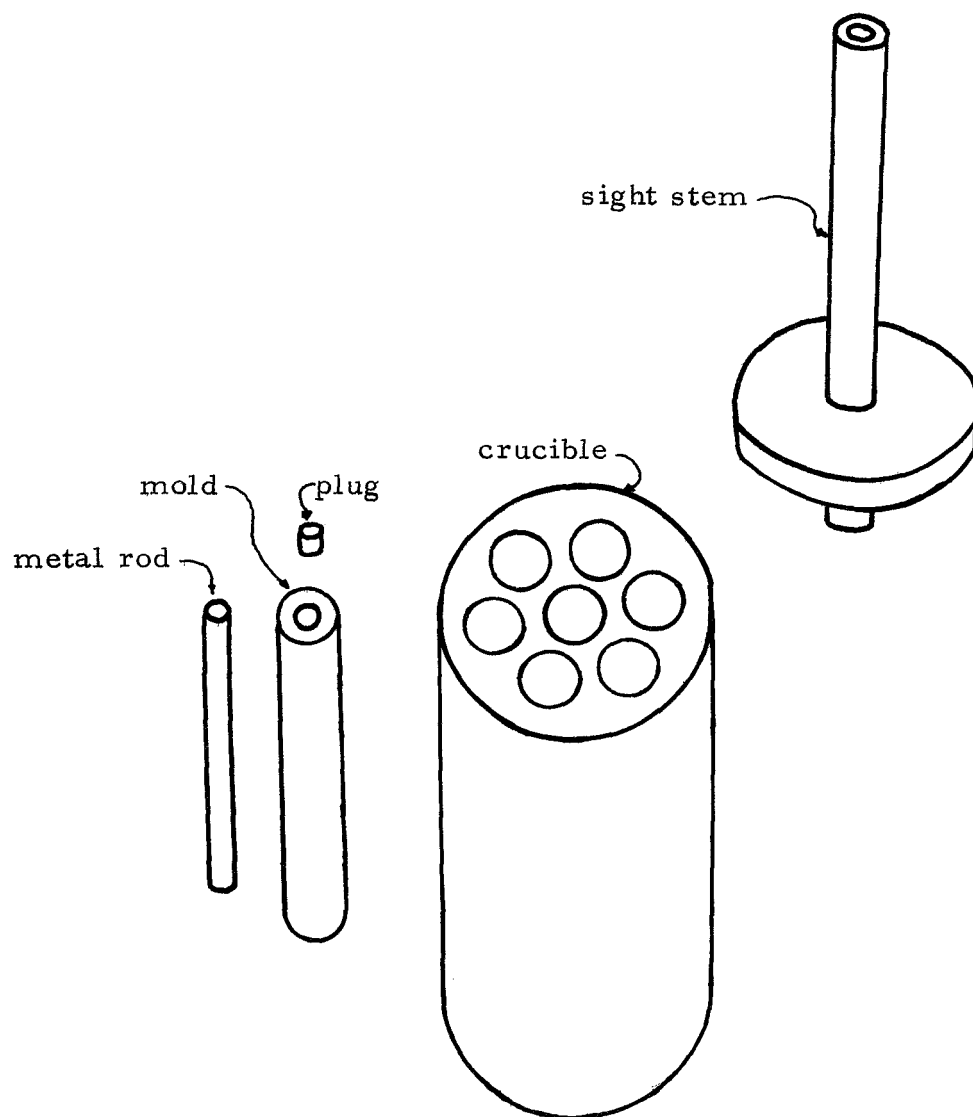


Figure 3. Six Rod Crucible Assembly

2.22 Graphite Crucible

Crucibles were made of ATJ graphite and were capable of holding six graphite molds. A schematic of the crucible is shown in Figure 3. The graphite crucible was 2.25 inches O.D. by 3.25 inches long. The molds were inserted into six holes 0.500 inch in diameter by 3.00 inches deep. The center hole was 0.250 inch diameter by 1.50 inches deep and was used to sight into the center of the crucible with a Leeds and Northrup optical pyrometer. The sight stem was made of ATJ graphite and was inserted through the lid into the center hole. The sight stem was 0.400 inch I.D. and 0.500 inch O.D. and projected 5.5 inches above the lid.

2.23 Induction Furnace

Schematic representation of the six-rod crucible and the radio frequency induction heating furnace is shown in Figure 4. The crucible was placed near the center of a inner Vycor (silica) tube 4.50 inches I.D. by 17 inches long. The graphite crucible was both supported on and covered with a five inch layer of purified lampblack. The sight tube projected one-half inch above the lampblack. The thickness of lampblack around the sides of the crucible was 1.25 inches. The lampblack did not heat in a radio-frequency field and thus was an excellent thermal insulator preventing the Vycor tube from reaching

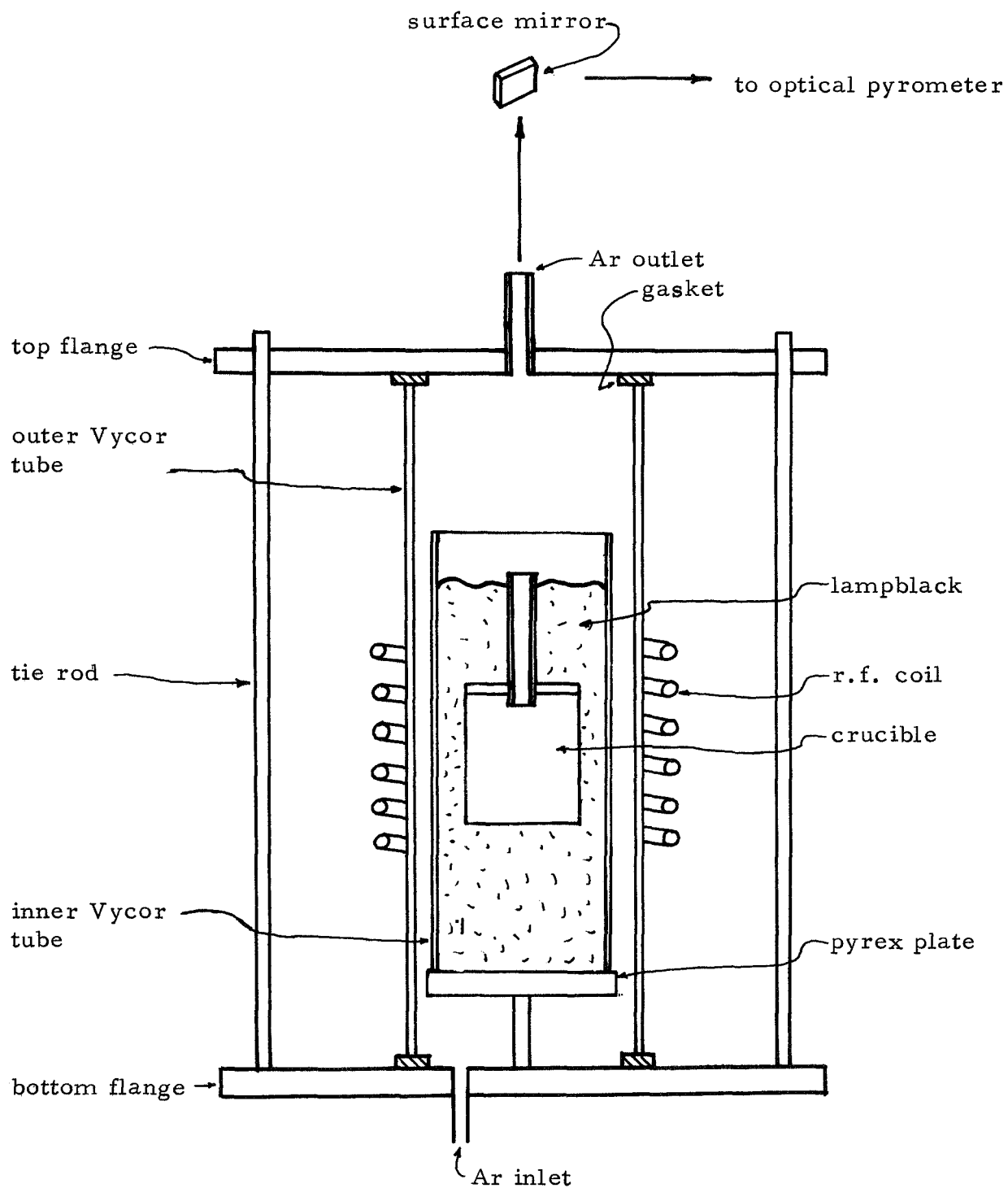


Figure 4. Schematic of Carburization Furnace

its softening temperature even when the internal temperature may be as high as 3000°C .

The inert gas protective environment was contained within a larger Vycor tube 5.50 inches I.D. by 18 inches long. Two stainless steel flanges closed the ends of the Vycor tube with tie bolts and silicon rubber gaskets. Argon entered the system through the bottom flange and exited through a nozzle in the top flange producing a dynamic seal. Temperatures were determined directly through the gas seal. The advantage of a dynamic seal was that it eliminated condensation on windows and therefore reduced some major pyrometry errors.

2.24 Radio-Frequency Power Source

Radio-frequency power was provided to the crucible by means of a six-turn coil of $3/8$ inch copper tubing six inches in diameter by 3.5 inches long. The coil fitted over the outer Vycor tube as shown in Figure 4. A Lepel 450 kilocycle generator rated at 15 kilowatts was used with no modification necessary. There was no difficulty in obtaining temperatures up to 3500°C but temperatures above 3000°C could be achieved for only short times. The ability to maintain temperatures above 3000°C for prolonged times was limited by vaporization of the graphite crucible and by carbon vapor condensing in the lampblack causing it to break down as an insulator and to act

as a poor r.f. susceptor. This breakdown resulted in raising the temperature of the inner Vycor tube to its softening point, 1100°C .

3.0 CARBIDE CHARACTERIZATION

3.1 Structure

The phase diagrams for Groups IVB and VB metal-carbon systems has been extensively studied and the currently accepted phase diagrams are shown in Figures 5 through 10. The phase diagrams indicate that one carbide, MeC, is present in the Group IVB metal-carbon systems and that two carbides, MeC and Me₂C, exist in the Group VB metal-carbon systems. The monocarbide in both Groups can exist over a wide range of composition with the range of solubility being larger in the Group IV carbides. The monocarbide and the dicarbide have a sodium chloride type structure and a hexagonal structure as shown in Figures 11 and 12. The MeC structure consists of two interpenetrating face-centered cubic arrays of carbon and metal atoms in which the carbon atoms occupy the octahedral interstices. For convenience the carbon atom maybe considered as an interstitial atom since it produces only a four percent linear expansion of the structure when carbon is added to a hypothetical pure f.c.c. metal to form its carbide. The metal atoms unlike the carbon atoms can not be removed from their normal sites except for the expected thermodynamic defect concentration.

The bonding between the carbon and metal atoms has been

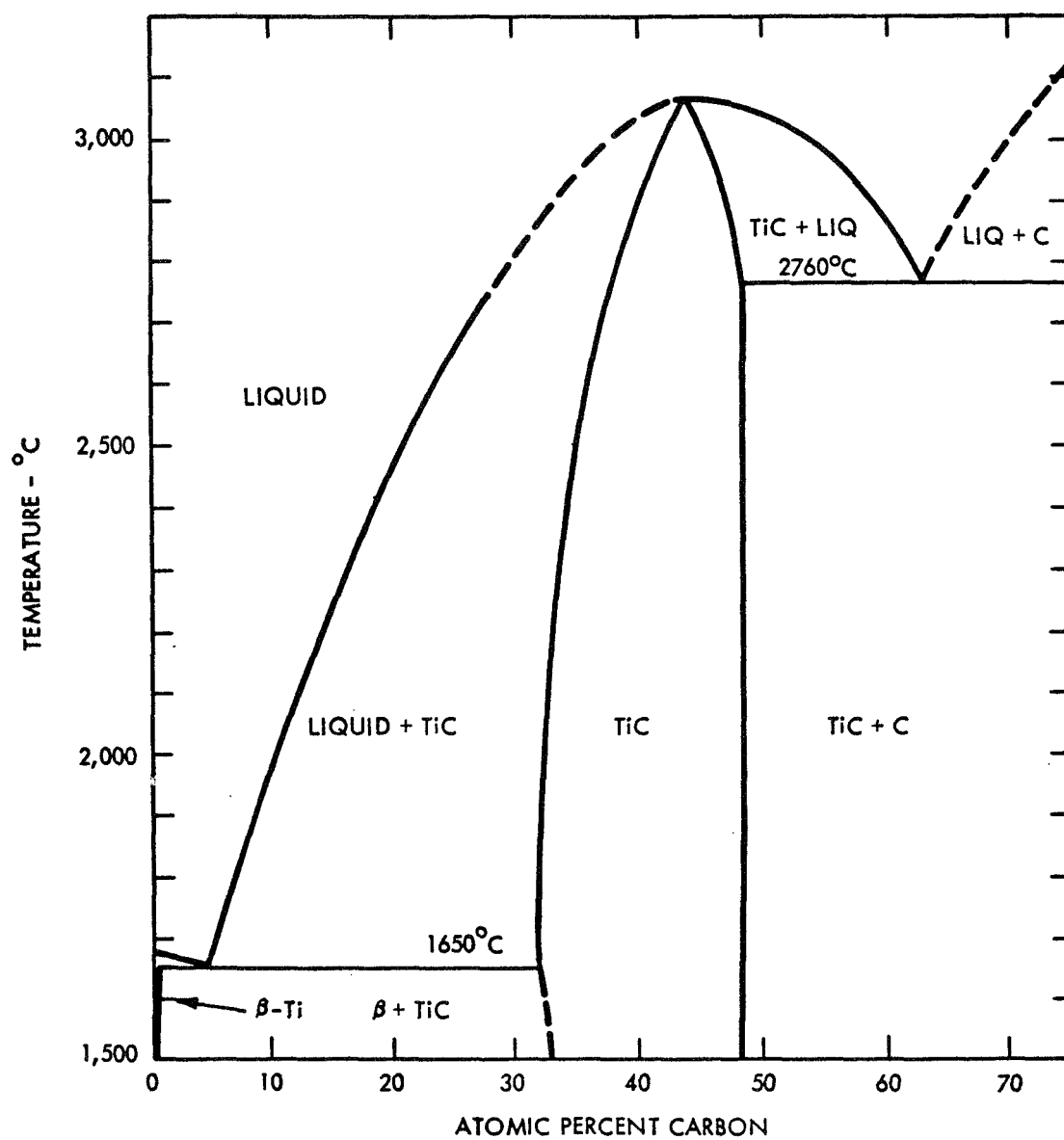


Figure 5. Titanium-Carbon Phase Diagram⁽⁸⁾ (3)

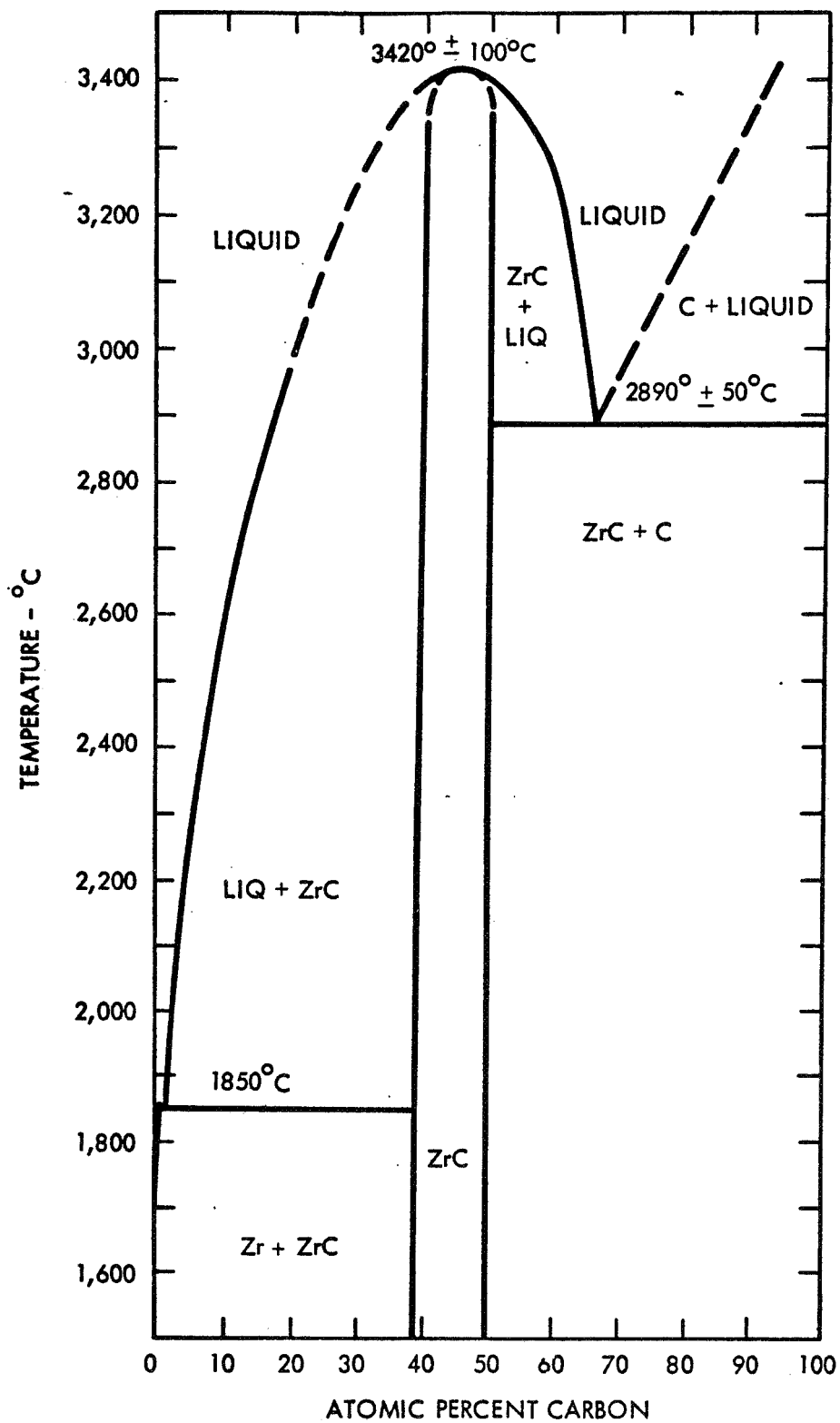


Figure 6. Zirconium-Carbon Phase Diagram^{(9) (4)}

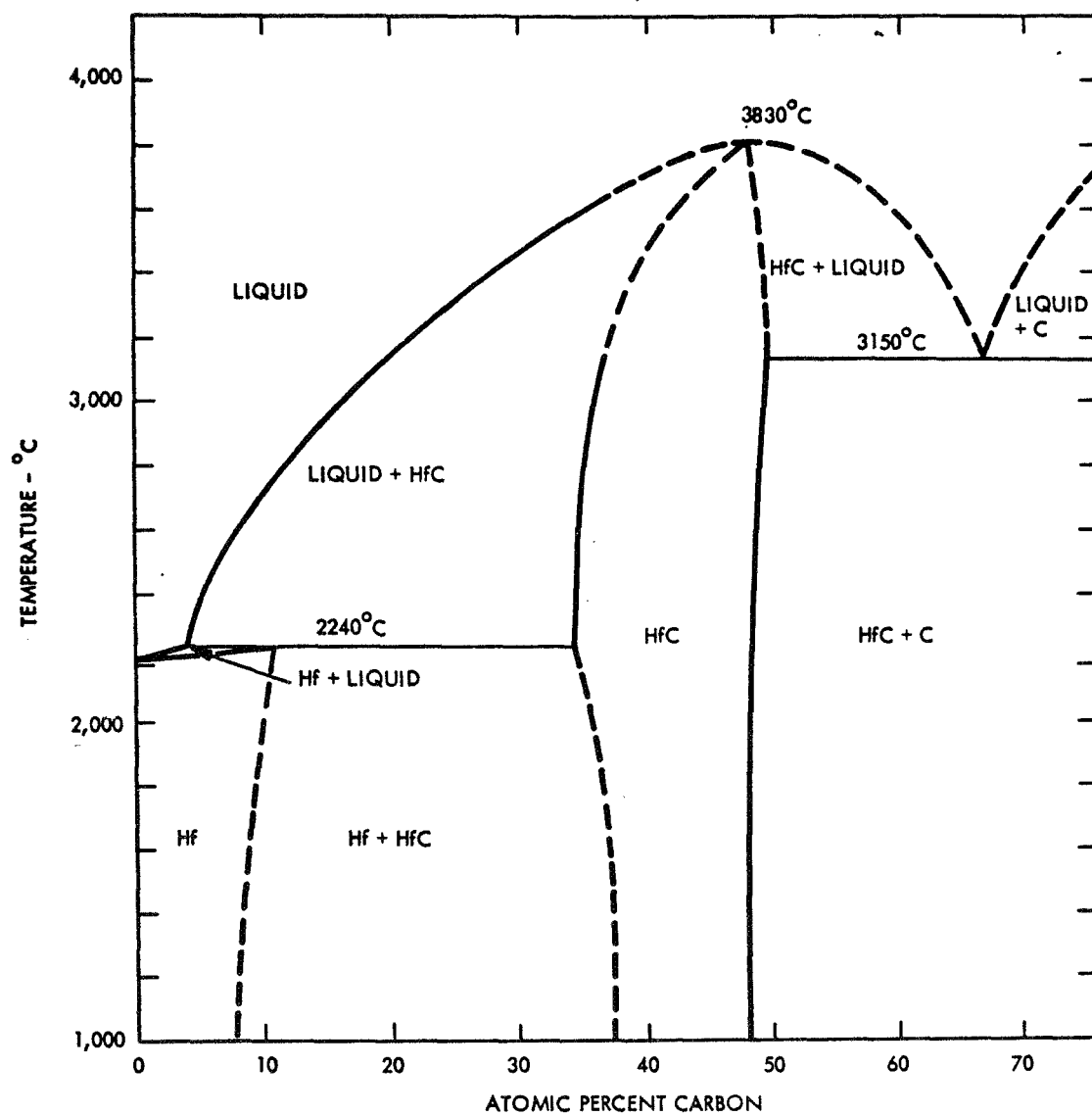


Figure 7. Hafnium-Carbon Phase Diagram^{(10) (3)}

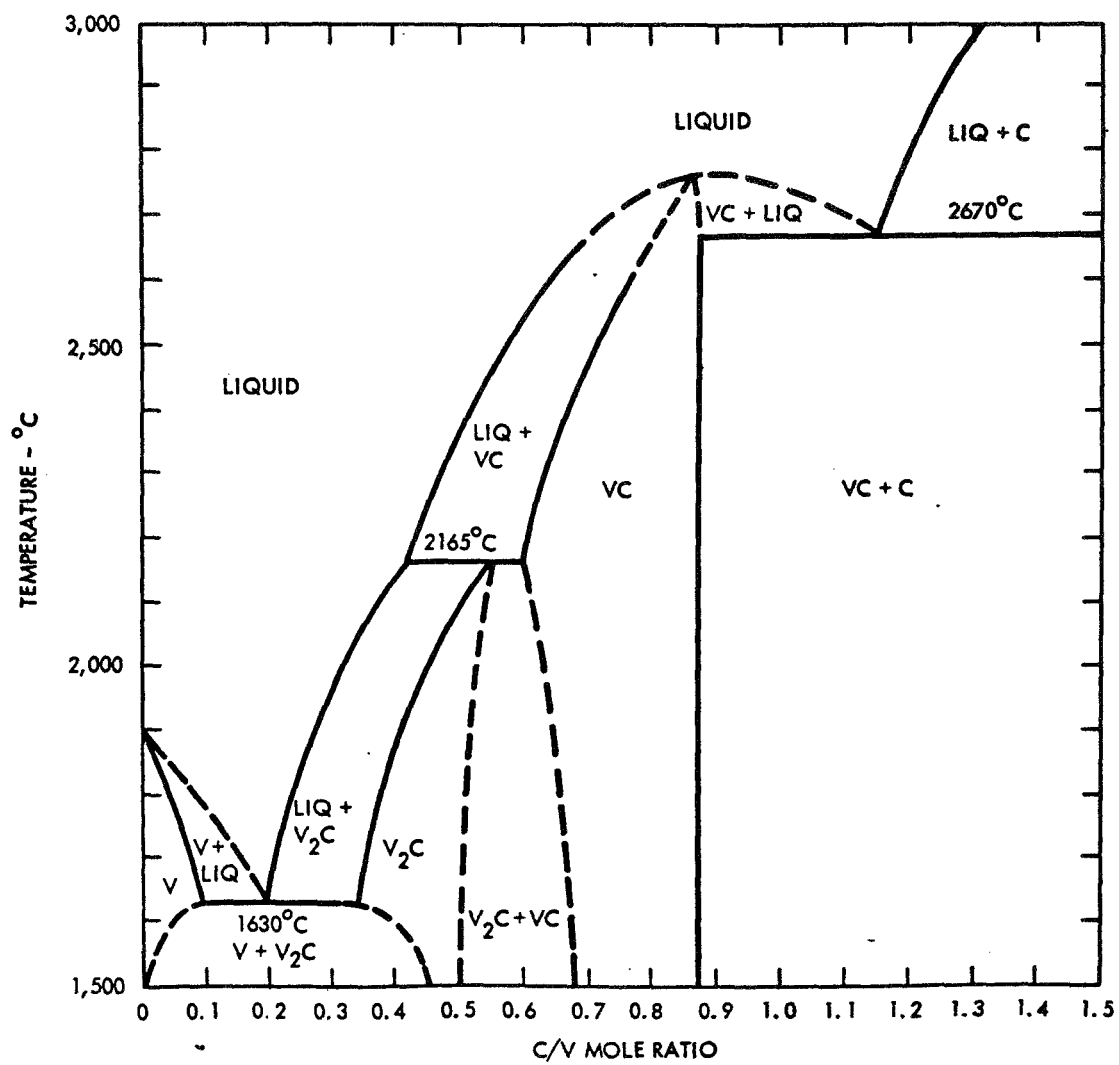


Figure 8. Vanadium-Carbon Phase Diagram⁽¹¹⁾ (5)

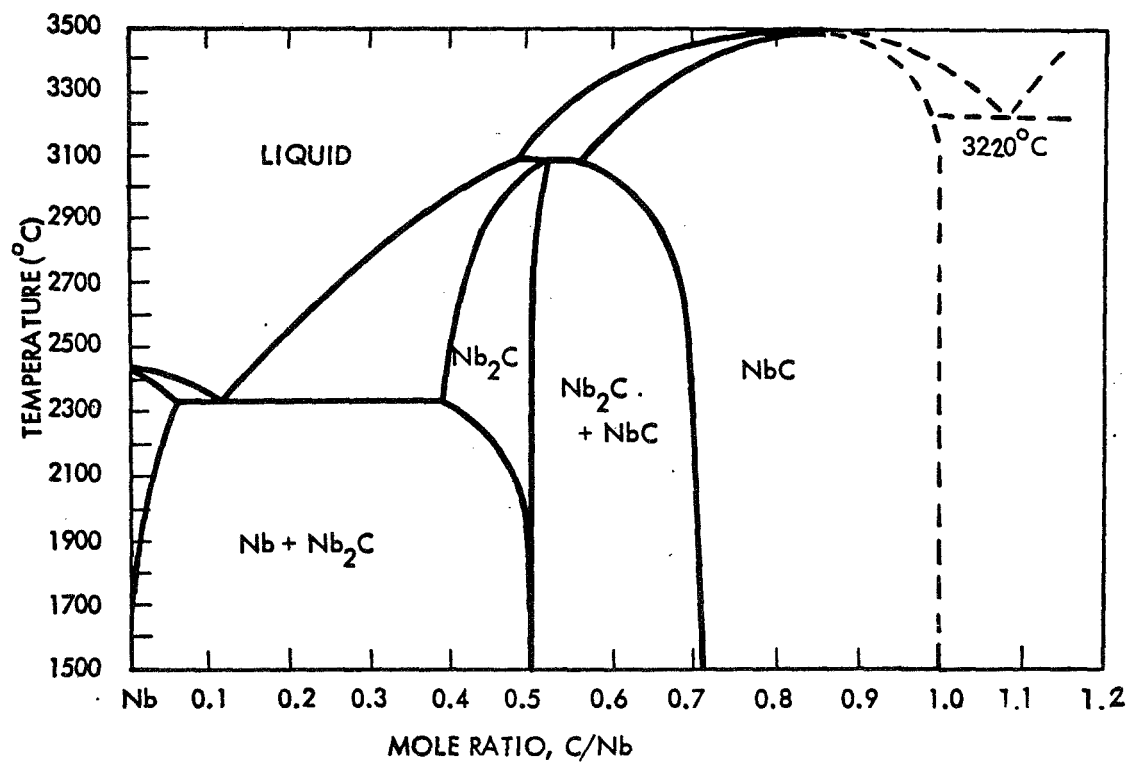


Figure 9. Niobium-Carbon Phase Diagram^{(12) (13)}

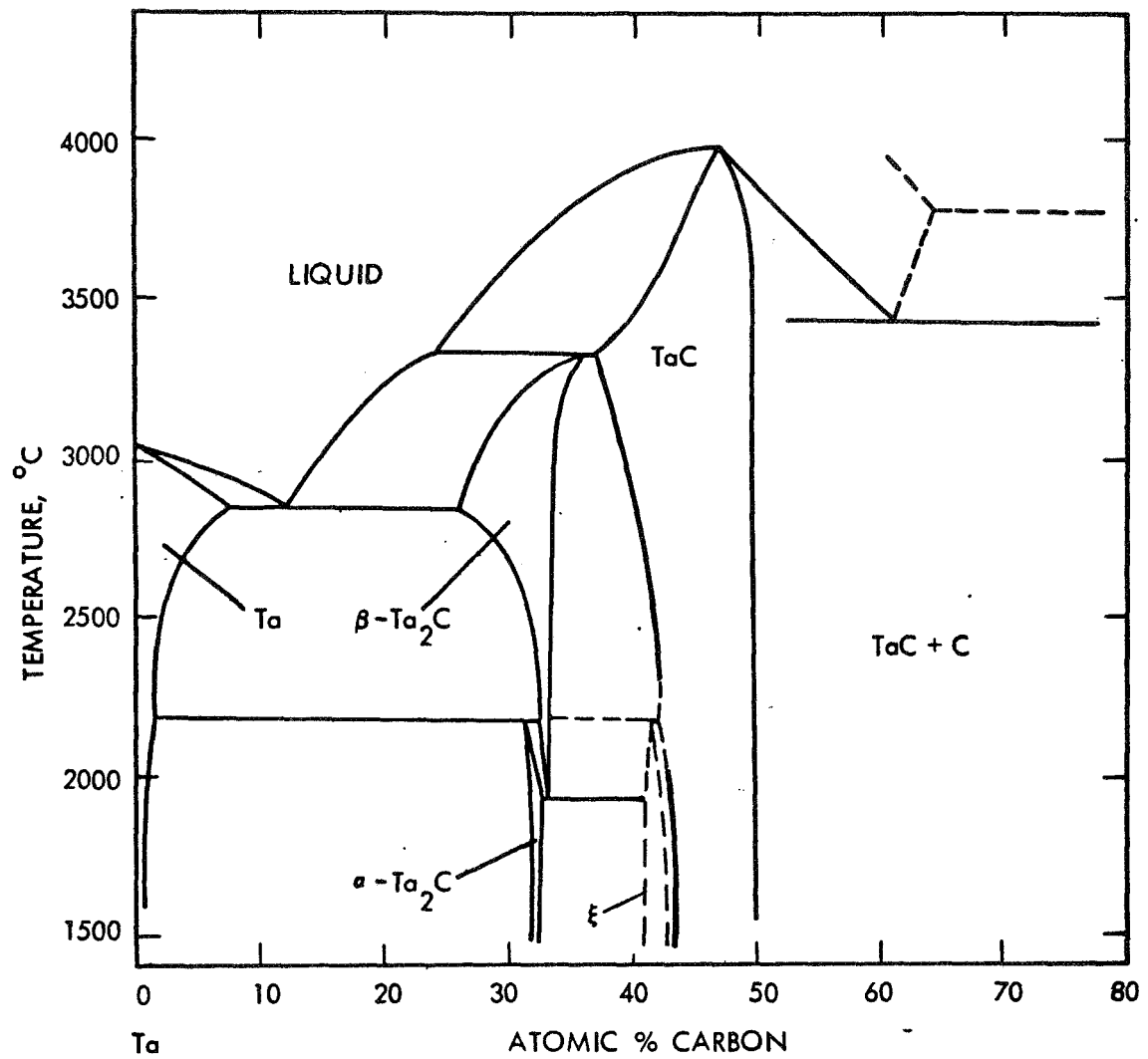


Figure 10. Tantalum-Carbon Phase Diagram^{(14) (15)}

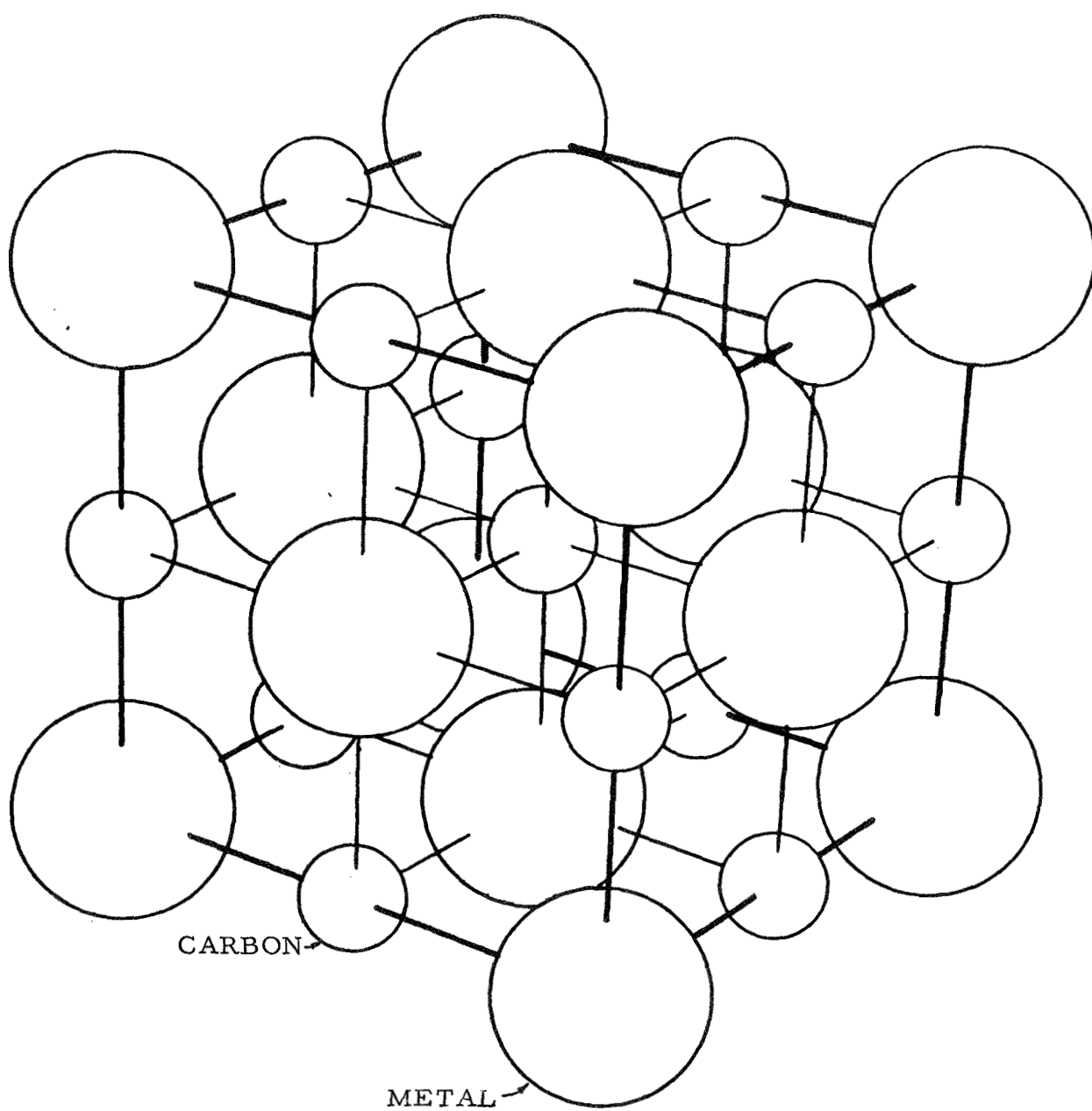


Figure 11. The B1 Structure of MeC

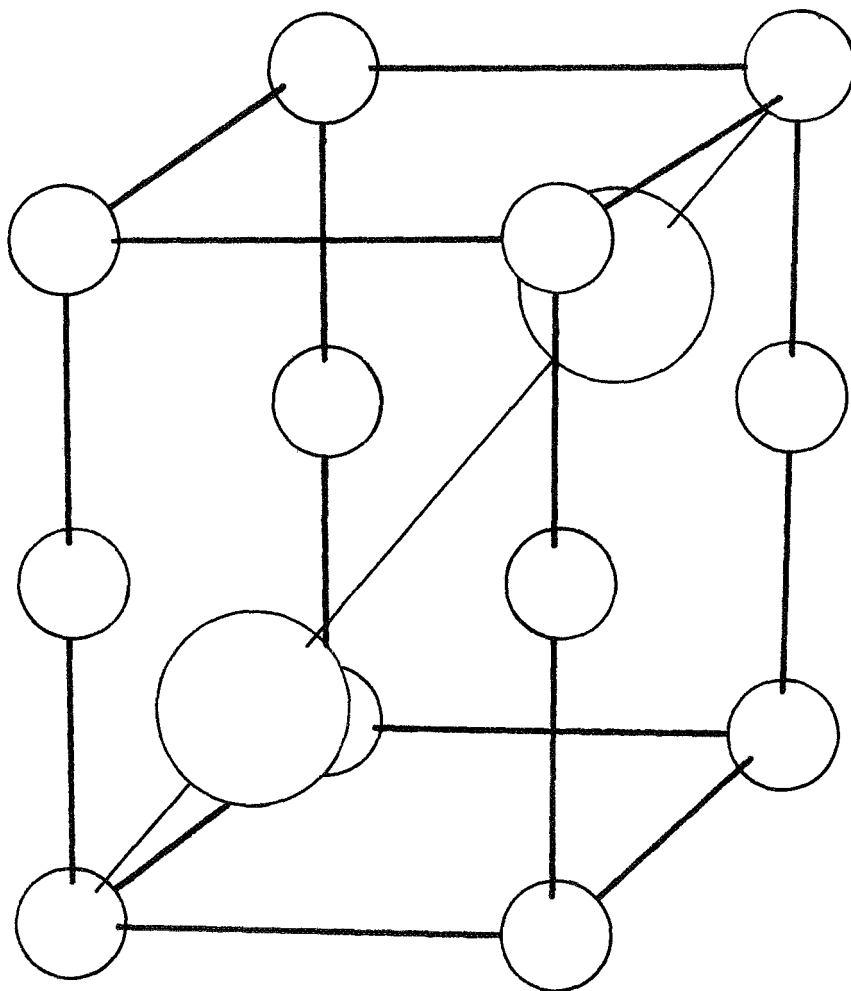


Figure 12. The B8 Structure of Me_2C

extensively studied by Lye.⁽¹⁶⁾ He suggests that there are three major contributions to the observed high strength of titanium carbide; (1) strong covalent metal-metal bonds, (2) carbon atoms donate electrons which increase the number of d-electrons participating in metal-metal bonding and (3) the metal-metal interaction is intensified by the presence of carbon atoms in overlap regions of neighboring metal atom d-orbitals. It seems probable that the same contributions may also occur in the other carbides.

3.2 Room Temperature Hardness

Hardness of the Groups IVB and VB metal monocarbides was studied with the intent of further characterizing bonding as a function of carbon composition in the carbides. Hardness is not a "primary" property and therefore its behavior is not expected to be explained from simple theoretical explanations. However it is believed that microhardness is related to the yield stress of the material and at room temperature it is believed that the yield stress of the carbide is a function of the Peierls stress or bond strength. Microhardness measurements were made across a monocarbide layer formed during a diffusion anneal between the parent metal and graphite. Hardness profiles (hardness vs. distance) were reported earlier.⁽¹⁷⁾ The present hardness data was related to composition using x-ray and

grinding procedures and its orientation dependence was also examined. These latter results confirmed the findings of Williams⁽¹⁸⁾ that hardness is a function of orientation. Because orientation affects the absolute value of the hardness number many grains were examined and a summary of the results of the dependence of hardness on composition are given in Figure 13. It is interesting to note that a definite trend appears. At high stoichiometries (MeC_x , where $x \approx 1.0$) the hardness is greatest for the first of the Group IV carbides and decreases as one proceeds down the Groups IV and V monocarbides. The opposite trend appears to be occurring for low stoichiometric carbides (MeC_x , where $x \approx 0.7$) i.e., the hardness is least for the Group IV carbides and increases as one proceeds down the Groups IV and V monocarbides. Thus for the Group IV carbides hardness is decreasing with decreasing carbon composition and for the Group V carbides hardness is increasing with decreasing carbon composition. The cross-over occurs near vanadium carbide. This behavior can be described in terms of the previously mentioned model proposed by Lye,⁽¹⁶⁾ i.e., carbon atoms can donate electrons which increases the number of d-electrons participating in metal-metal bonding. It follows then that in the Group IV carbides as the carbon concentration increases or as the number of 3d-electrons increases the Me-Me bonding increases. In the Group VB, however, the 3d states

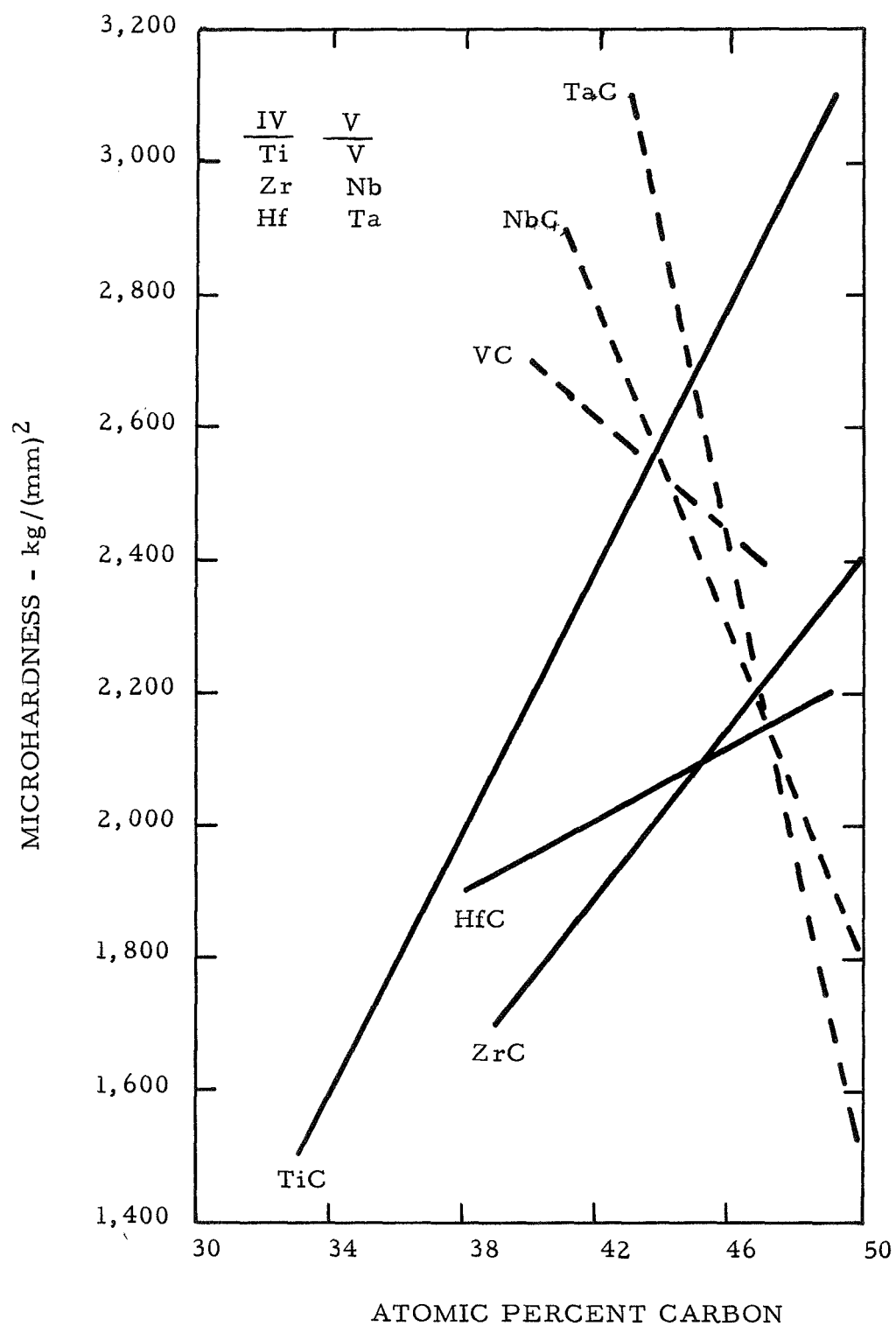


Figure 13. Summary of the Hardness of the Groups IVB and VB Monocarbides as a Function of Composition. Depending on Orientation Hardness May Vary by $\pm 200 \text{ kg}/(\text{mm})^2$.

are saturated at low stoichiometries and as the carbon concentration increases carbon atoms donate electrons to anti-bonding d-states which results in a decrease in hardness.

A decrease in hardness near the lower carbon compositional limit in tantalum carbide has been reported by Santoro⁽¹⁹⁾ as being due to a maximum in the bonding. Verification of a decrease in hardness in tantalum carbide at low stoichiometry was reported earlier⁽¹⁷⁾ and was also found to occur in the present study of the HfC-C, VC-C and NbC-C systems. It is believed that the decrease in hardness at low stoichiometries can not be attributed to a maximum in bonding but that the decrease in hardness results from indentations being made in a two phase region. Evidence of a second phase can clearly be seen from a photomicrograph and an electron micrograph, Figures 14 and 15. Precipitation is expected since the solvus lines (Figures 7, 8, and 9) are sloping away from the two phase regions with decreasing temperature. It is not known whether the precipitate was present and undetectable before hardness testing or whether precipitation was stress induced during indentation. Until the precipitation phenomena associated with the hardness impression is shown to be irrelevant the decrease in hardness or the apparent maximum in the hardness at low stoichiometries can not be realistically explained in terms of maximum in the bonding.

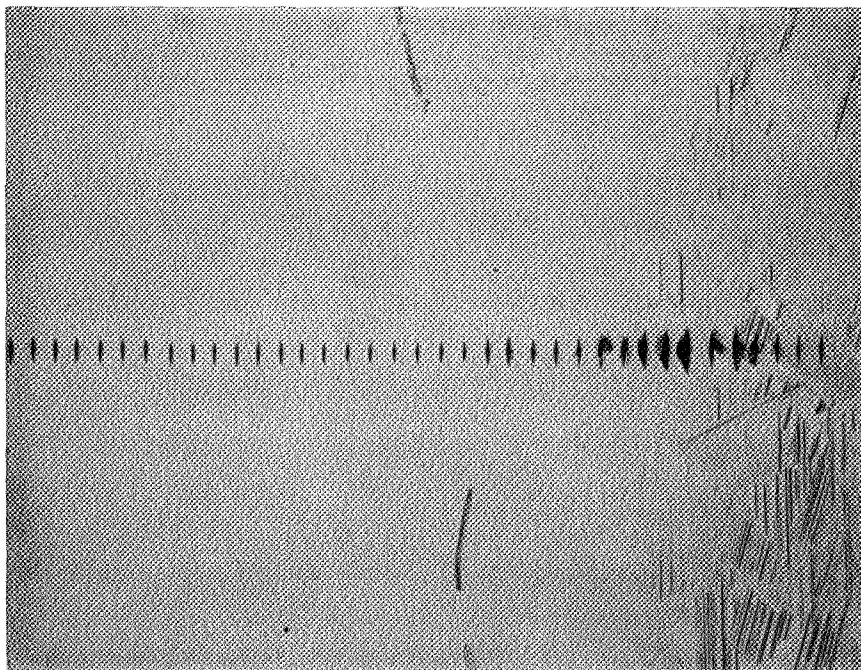


Figure 14. Photomicrograph of Hardness Impressions in TaC Showing a Precipitation Phenomena Associated with Impressions Made at Low Stoichiometries (150 x)

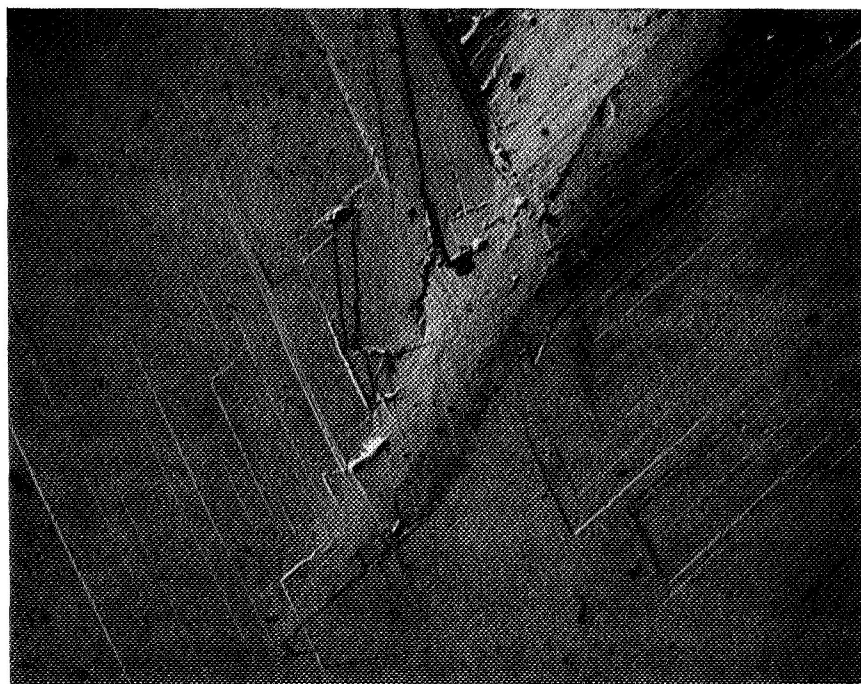


Figure 15. Electron Micrograph of Hardness Impression at Low Stoichiometry (6,000 x)

3.3 Thermal Expansion

The void of information on the high temperature thermal expansion of vanadium carbide provided the stimulus to measure its thermal expansion behavior. The thermal expansion characteristics of the other carbides were also investigated. The preliminary results of this study were reported earlier.⁽¹⁷⁾

3.31 Sample Preparation

Carbide specimens 3/8 inch diameter by two inches long were fabricated using the same method discussed in section 2.1. The desired test specimen was three inches long which required cropping the ends of the as-fabricated specimens with a diamond cut-off wheel and brazing the two sections together. A schematic diagram of the brazing unit is given in Figure 16. The brazing was done by placing a 2mil foil of zirconium metal between two specimens, heating to 2000°C in less than 30 seconds to insure good wetting of both carbide surfaces and annealing at 2300°C for ten minutes to convert the zirconium metal into carbide. The specimen was then shaped with a diamond cut-off wheel into the test specimen configuration shown in Figure 17.

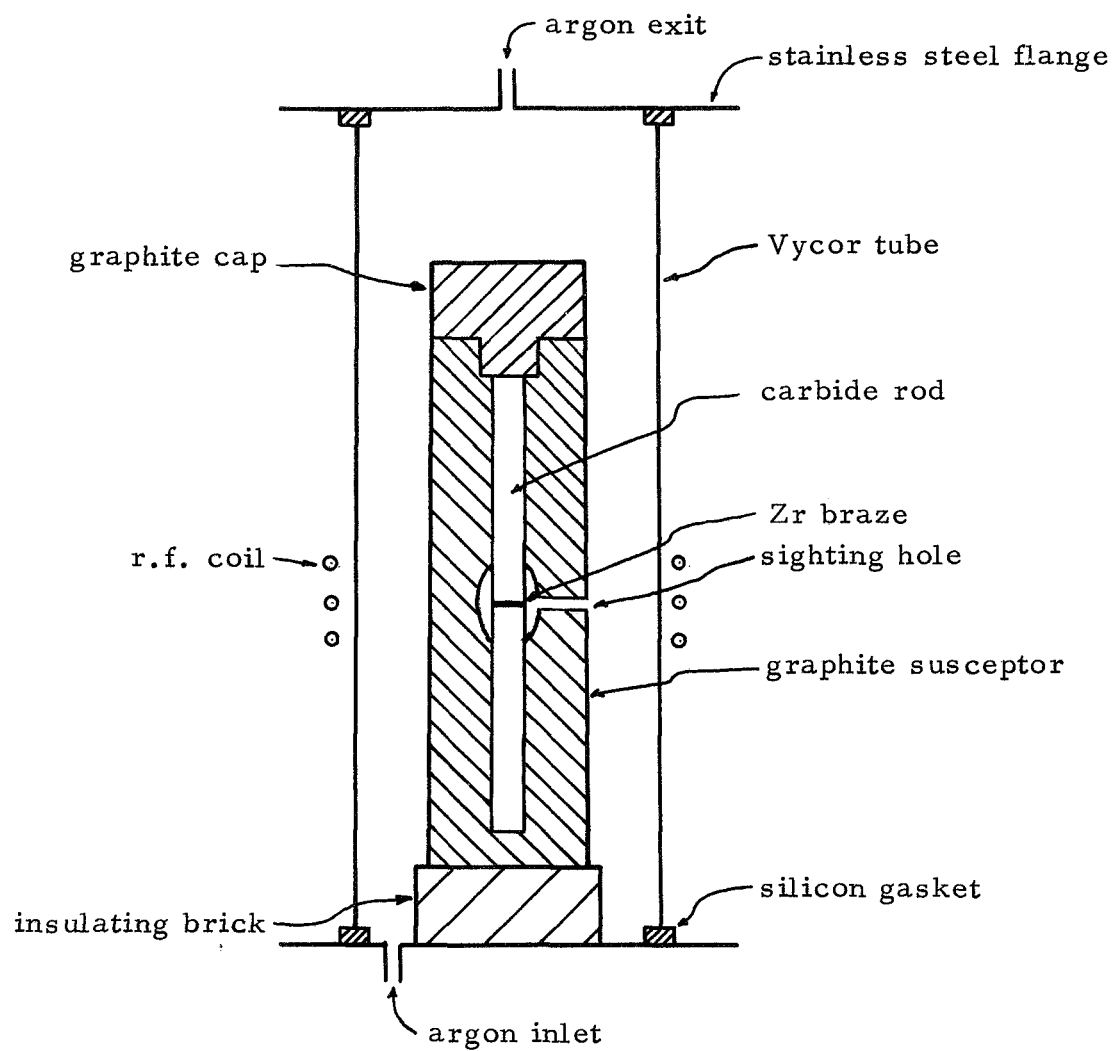


Figure 16. Schematic of Brazing Apparatus

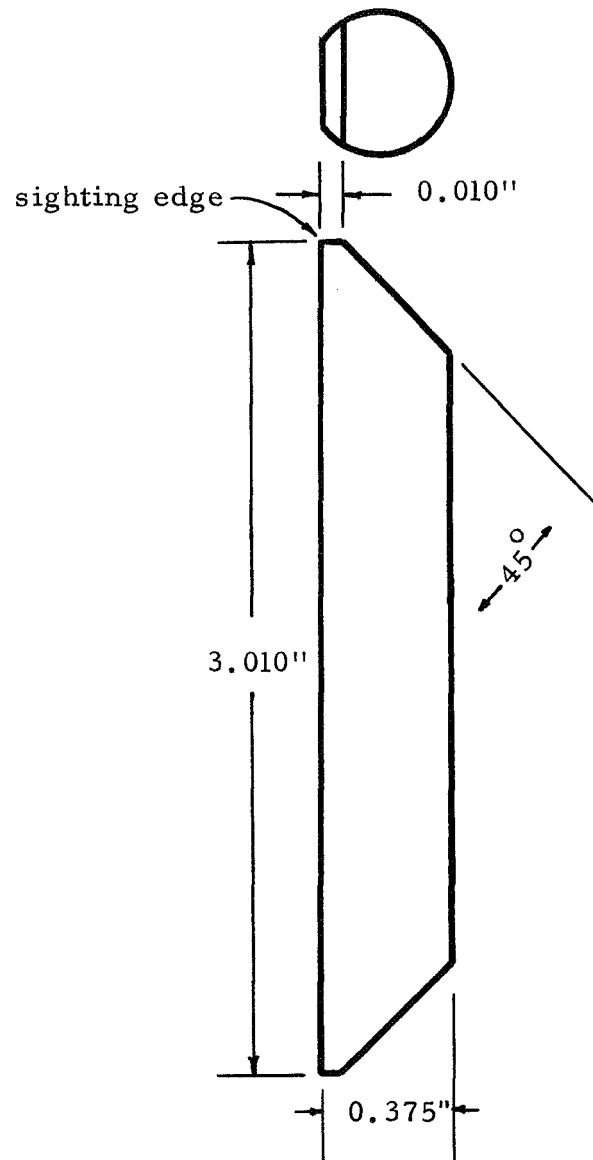


Figure 17. Thermal Expansion Test Specimen Configuration

3.32 Apparatus

Thermal expansion measurements of six carbides were made in a graphite furnace which was evacuated and back-filled with helium to a pressure of 15 microns. Samples were heated by two graphite hair-pin heating elements which maintained a flat plate-shape heat zone. Specimens were mounted upright between the two heating elements and the sighting edges were visible through viewing ports in the front and back of the furnace. The measuring device consisted of two micro-telescopes (50x) mounted in a frame anchored in a large surface stone that was free to traverse on an air-bearing surface from sample to sample across a larger granite stone that provided the stable platform necessary for accurate measurements. The microtelescopes were equipped with motor driven filar eyepieces and transmitting potentiometers. Low temperatures were measured with an infrared pyrometer and high temperatures with a Milletron two-color pyrometer. The overall accuracy of the system is estimated to be \pm two percent of the measured value at 2000°C and to have a temperature uniformity of $\pm 15^{\circ}\text{C}$.

3.33 Results and Discussion

The thermal expansion of vanadium carbide as a function of temperature is given in Figure 18. The only other data obtained on

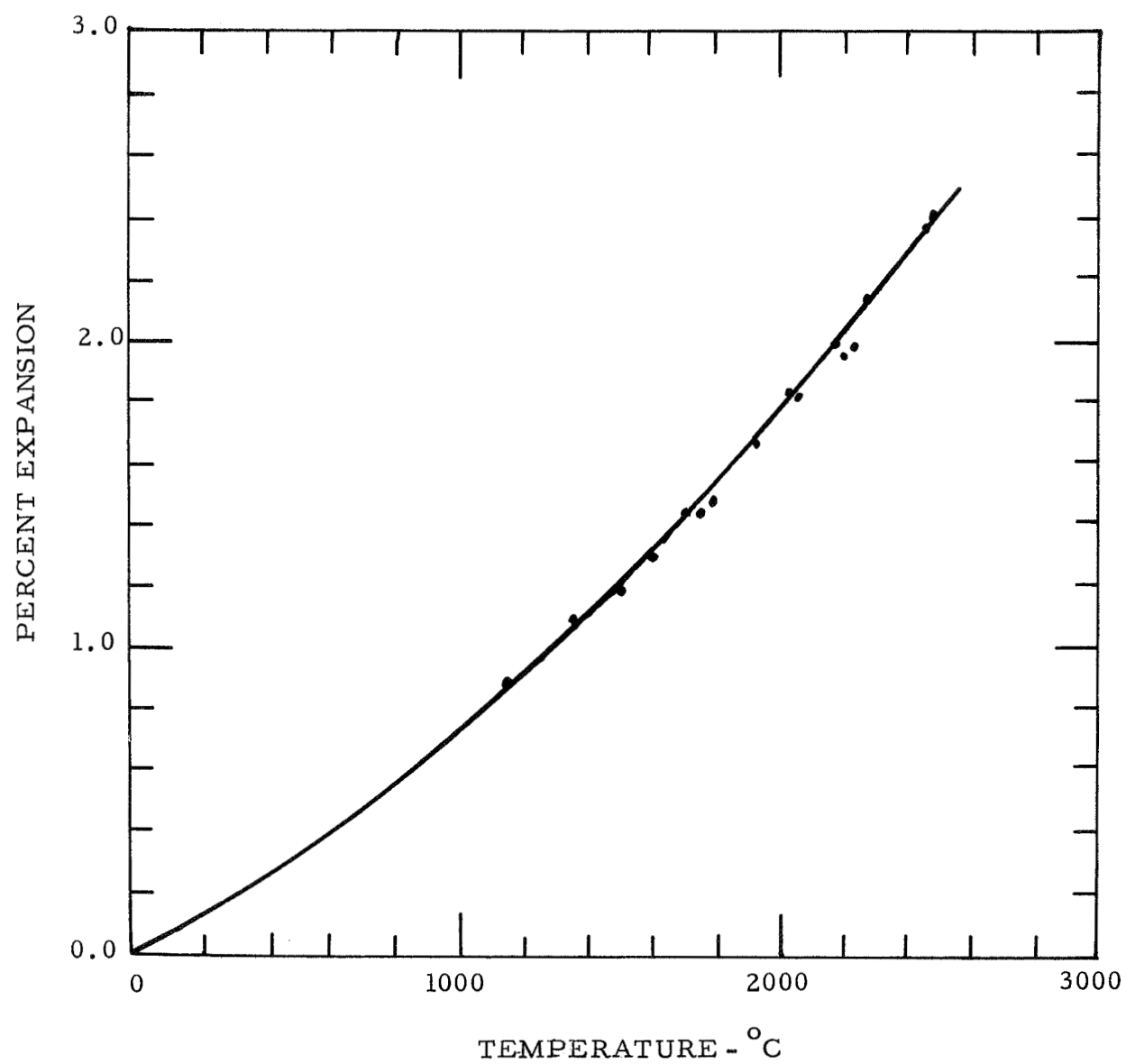


Figure 18. Linear Thermal Expansion vs. Temperature for VC

vanadium carbide was by Storms and Kempter⁽²⁰⁾ using x-ray measurements to 600°C and it is in agreement with the present work. The thermal expansion of the other five carbides is shown in Figures 19 through 23. From the data presented in Figures 19 through 23 a least mean equation for each of the carbides has been computed and is given in Table 3. From the equations presented in Table 3 the average coefficients of thermal expansion as a function of temperature are given in Table 4. A recent bibliography on thermal expansion of the carbides has been given by Fries and Wahman⁽²¹⁾ and the present thermal expansion measurements are in agreement with the wide scatter of data obtained among the other investigators. The expansion of the carbides appear to follow the same relationship as mentioned earlier i.e., the amount of expansion increases with decreasing melting temperature and decreasing atomic number within each Group. Also there appears to be a relationship between the average coefficient of expansion, $\bar{\alpha}$, and hardness as a function of carbon composition. From previous expansion measurements⁽²⁰⁾⁽²¹⁾⁽²²⁾ and the present hardness measurements it is found that $\bar{\alpha}$ decreases with increasing hardness in the vanadium, niobium and tantalum carbide systems.

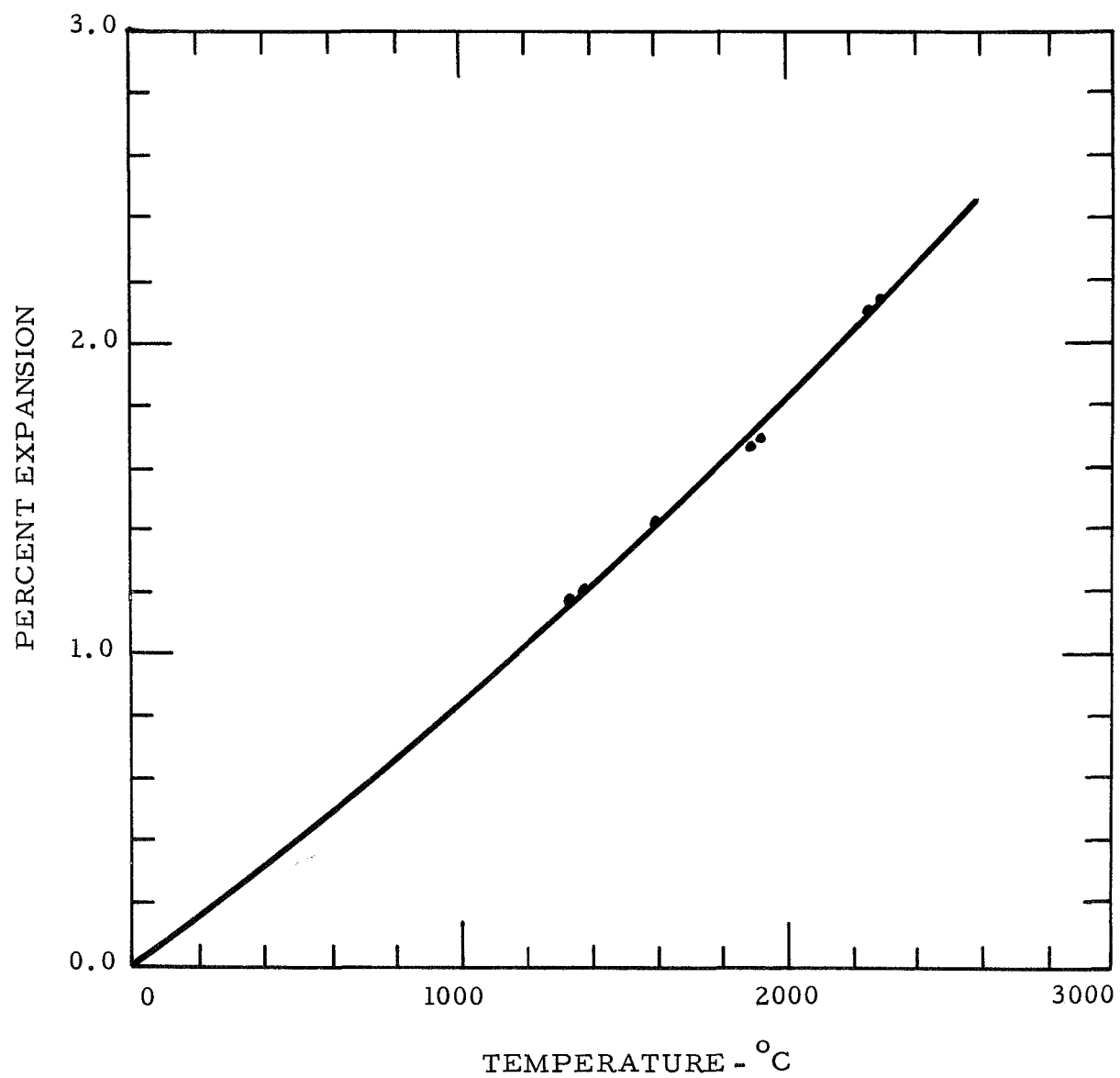


Figure 19. Linear Thermal Expansion vs. Temperature for TiC

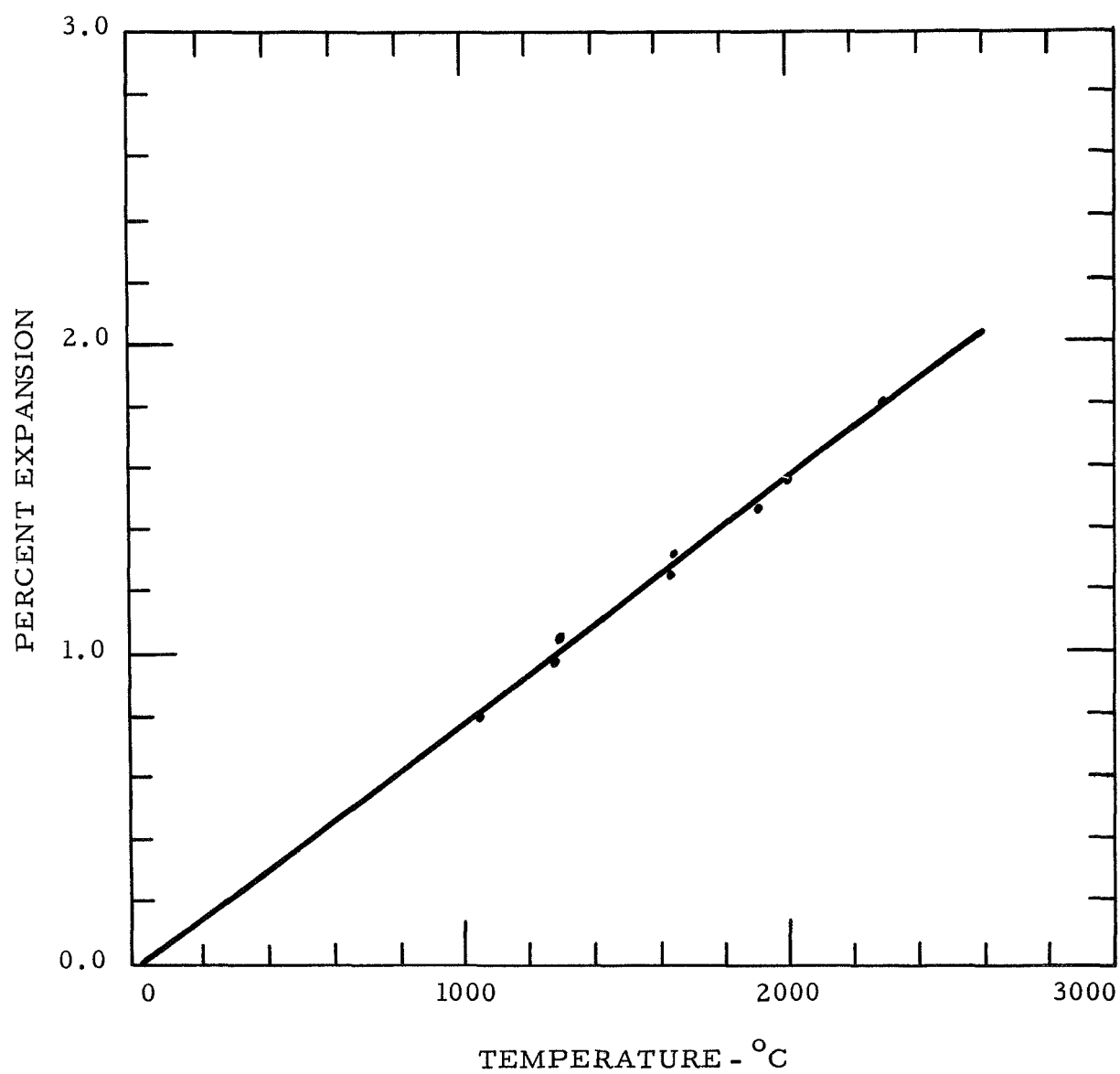


Figure 20. Linear Thermal Expansion vs. Temperature for ZrC

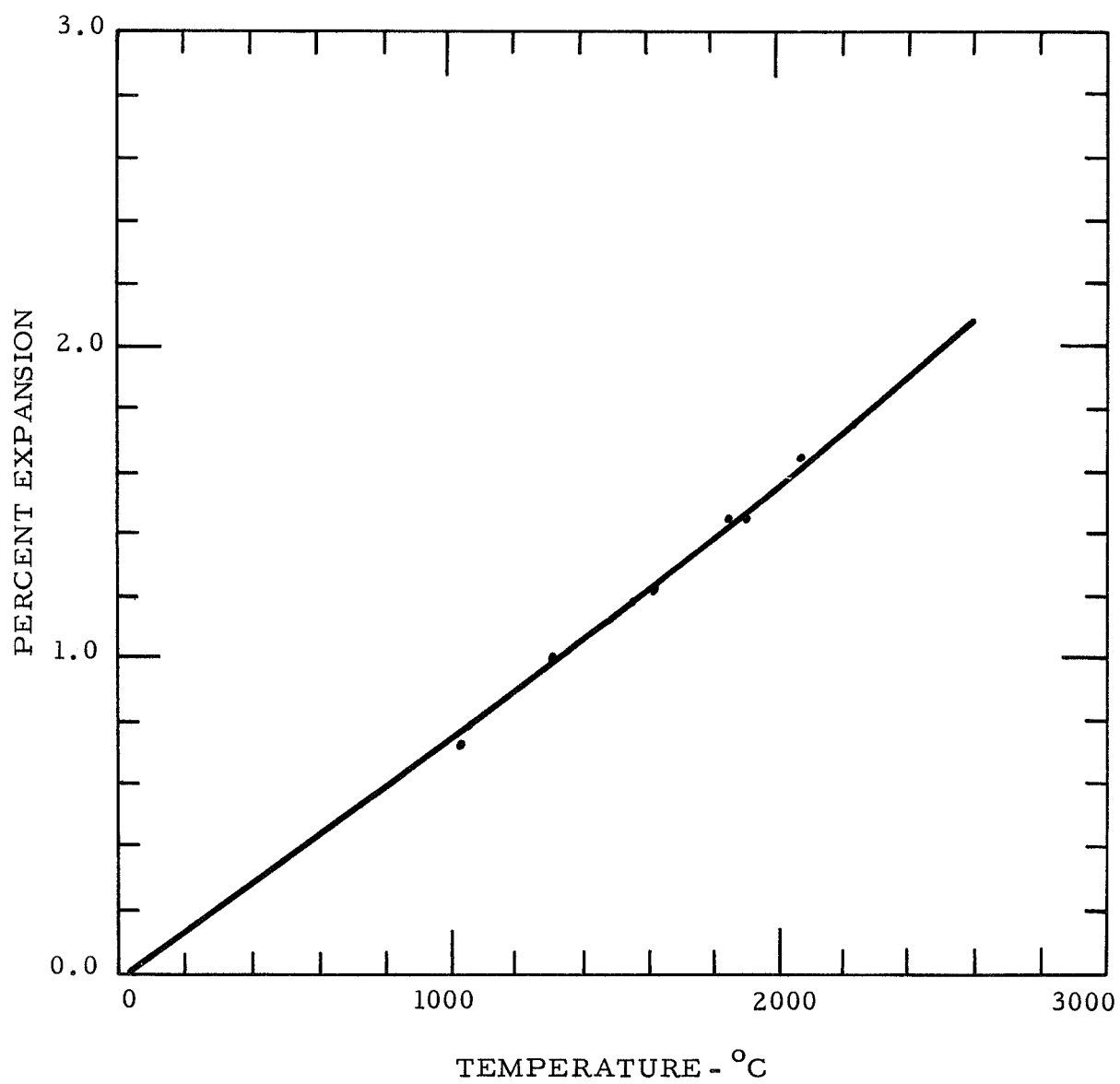


Figure 21. Linear Thermal Expansion vs. Temperature for HfC

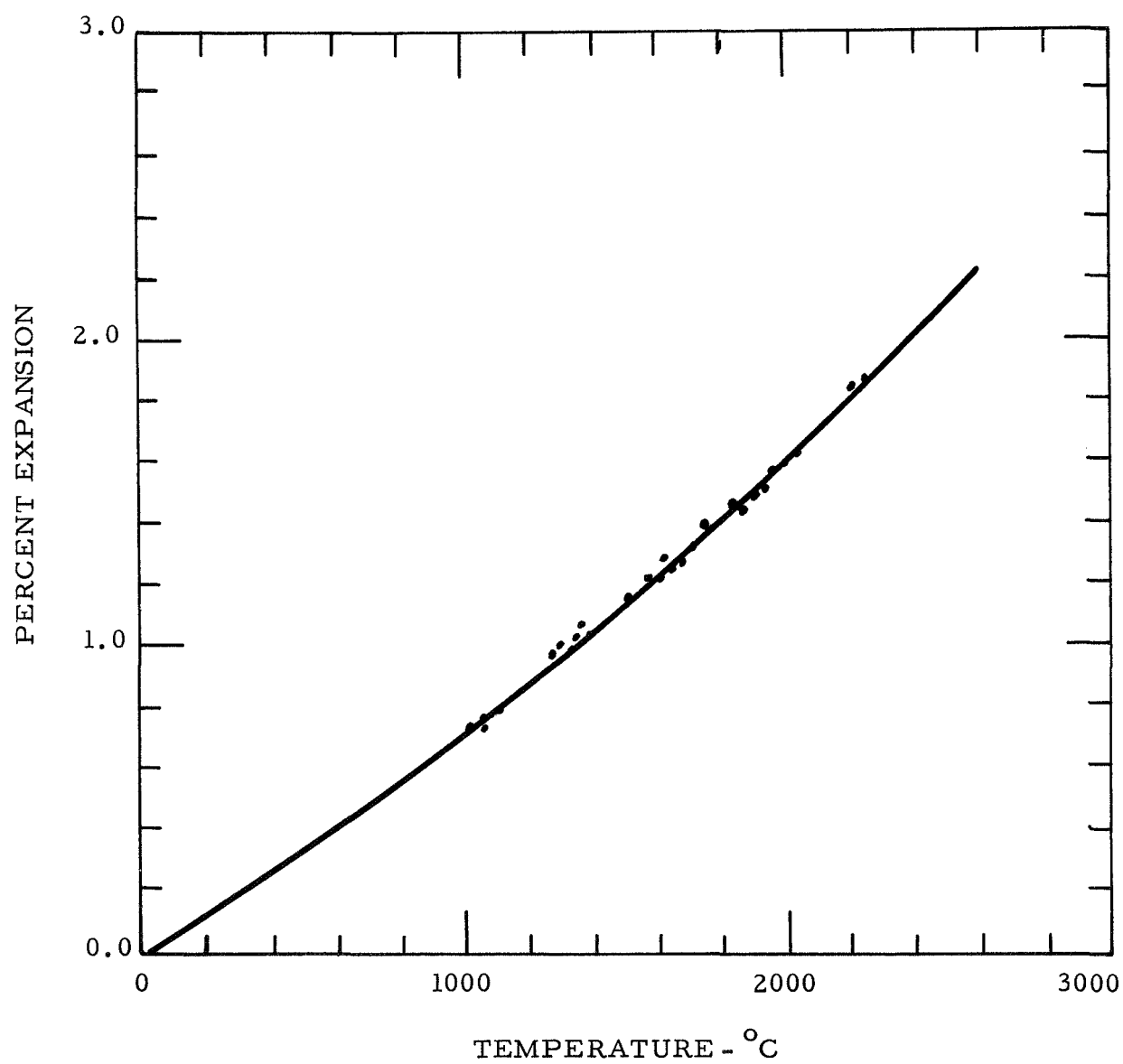


Figure 22. Linear Thermal Expansion vs. Temperature for NbC

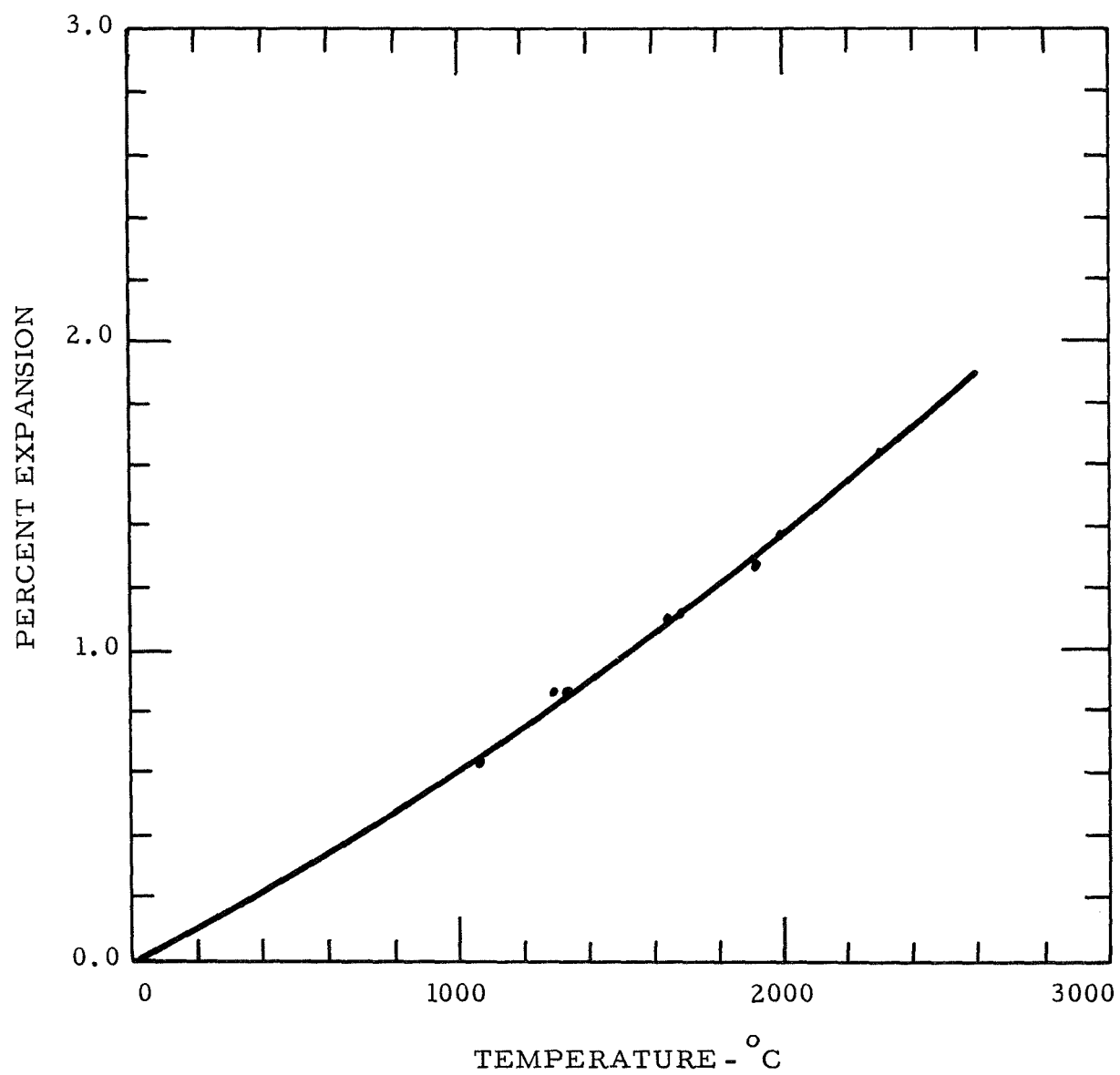


Figure 23. Linear Thermal Expansion vs. Temperature for TaC

TABLE 3

Least Squares Equation for Thermal Expansion
of the Groups IVB and VB Monocarbides
as a Function of Temperature

$$\text{Percent Expansion} = -A + B \times 10^{-4} T + C \times 10^{-7} T^2 (^\circ\text{C})$$

	A	B ($^\circ\text{C}$) ⁻¹	C ($^\circ\text{C}$) ⁻²
TiC	0.0160	7.8136	0.67440
ZrC	0.0228	7.8664	0
HfC	0.0175	6.8803	0.47870
VC	0.0092	5.3705	1.6292
NbC	0.0143	6.2846	0.89740
TaC	0.0134	5.5639	0.67490

TABLE 4

Average Coefficient of Thermal Expansion
for the Groups IVB and VB Monocarbides

$$\bar{\alpha} (10^{-6}/^{\circ}\text{C})$$

Temperature $^{\circ}\text{C}$	<u>TiC</u>	<u>ZrC</u>	<u>HfC</u>	<u>VC</u>	<u>NbC</u>	<u>TaC</u>
100	8.157	7.255	6.725	5.991	6.421	5.573
200	8.077	7.600	6.894	5.997	6.496	5.682
300	8.104	7.696	6.975	6.014	6.582	5.761
400	8.152	7.742	7.039	6.146	6.670	5.834
500	8.208	7.768	7.096	6.290	6.758	5.905
600	8.269	7.785	7.150	6.442	6.847	5.975
700	8.331	7.797	7.202	6.596	6.936	6.043
800	8.394	7.806	7.253	6.753	7.026	6.112
900	8.459	7.813	7.303	6.911	7.115	6.180
1000	8.524	7.818	7.353	7.070	7.205	6.249
1100	8.590	7.823	7.403	7.230	7.294	6.317
1200	8.655	7.826	7.452	7.391	7.384	6.384
1300	8.722	7.830	7.501	7.551	7.473	6.452
1400	8.788	7.832	7.550	7.712	7.563	6.520
1500	8.854	7.835	7.598	7.874	7.653	6.588
1600	8.921	7.837	7.647	8.035	7.742	6.656
1700	8.988	7.838	7.695	8.197	7.832	6.723
1800	9.054	7.840	7.744	8.359	7.922	6.791
1900	9.121	7.841	7.792	8.521	8.011	6.859
2000	9.188	7.843	7.840	8.683	8.101	6.926
2100	9.255	7.844	7.889	8.845	8.191	6.994
2200	9.322	7.845	7.937	9.007	8.280	7.062
2300	9.389	7.846	7.985	9.169	8.370	7.129
2400	9.456	7.847	8.033	9.332	8.460	7.197
2500	9.523	7.847	8.081	9.494	8.550	7.264

3.4 Long-Range Ordering

Ordering of carbon atoms in vanadium monocarbide has been studied by Froidevaux and Rossier,⁽²³⁾ de Novion,⁽²⁴⁾ and Venerables, Kahn and Lye⁽²⁵⁾ using x-ray, electron microscopy, and nuclear magnetic resonance studies. Venerables has suggested that the ordered compound is V_6C_5 and has determined an order-disorder temperature to be approximately 1300°C . Kahn using nuclear magnetic resonance studies has described the distribution of carbon vacancies in $VC_{0.84}$. The ordered structure is described as being built up of (111) planes of carbon and vanadium atoms, however, on alternate carbon layers carbon vacancies are present in an hexagonal pattern. Due to birefringence and the large domain size ordering can easily be seen on metallographic samples at sixty magnifications using polarized light. A photomicrograph of an area of a diffusion couple between graphite and vanadium metal showing a band of ordering is shown in Figure 24. The optically active region was found to exist over the compositions $VC_{0.86}$ to $VC_{0.81}$ using grinding and x-ray analyses. Whether ordering exists over a larger range in composition was not determined. The order-disorder temperature was investigated using conventional annealing and quenching experiments. The order-disorder temperature was found to be $1300^{\circ}\text{C} \pm 50^{\circ}\text{C}$ in agreement with Venerables. This temperature was well below the

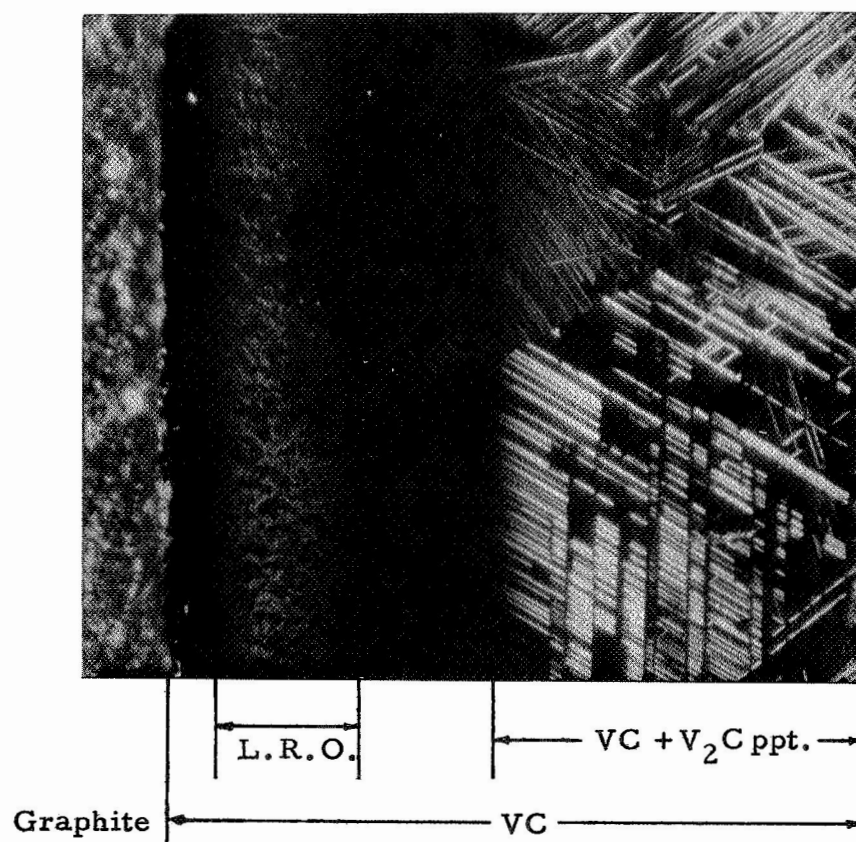


Figure 24. Photomicrograph of a Portion of a Diffusion Couple between Vanadium Metal and Graphite Showing a Region of Long Range Order in VC. (60 x, polarized light)

temperatures used in the mechanical property study to be discussed and thus long-range ordering was not considered in describing its high temperature mechanical behavior.

4.0 HIGH TEMPERATURE DEFORMATION

4.1 Introduction

Deformation characteristics of titanium carbide have been examined by Williams⁽²⁶⁾ and Hollox.⁽²⁷⁾ From electron micrographs they suggest that titanium carbide has a high stacking fault energy because dissociation of dislocations into partials has not been observed. Dissociation of dislocations also has not been observed in zirconium carbide, Figure 2. The slip system in titanium carbide has been determined to be $\{111\} \langle 110 \rangle$ by etch pit⁽²⁸⁾ and electron microscopy⁽²⁹⁾ studies. It is interesting to note that this slip system is the same for f.c.c. metals and not that observed for sodium chloride strongly suggesting that the carbides do not have ionic character as expected. In general it is assumed that all the Groups IVB and VB carbides have the same deformation characteristics.

4.2 Yield Stress Behavior

4.21 Introduction

Yield strength measurements on carbides have been made by Williams,⁽²⁶⁾ Hollox,⁽²⁷⁾ Kelly,⁽³⁰⁾ Steinitz,⁽³¹⁾ Santoro⁽³²⁾ and Johansen.⁽³³⁾ Williams measured the behavior of titanium and

niobium carbides as a function of temperature. He determined that niobium carbide was stronger than titanium carbide and that both were very temperature dependent. He also observed that titanium carbide increased in strength as carbon vacancies were removed contrary to TiO_2 in which strengthening occurs due to dislocation vacancy interactions. Hollox has indicated that this behavior is expected because oxygen ions are large in rutile and they therefore govern the mechanical behavior. In titanium carbide the carbon atoms are interstitial and titanium atoms are expected to control the mechanical behavior. Hollox has measured the yield strength of titanium and vanadium carbide and has also noted a strong temperature dependence. He examined the strength of vanadium carbide as a function of composition and found the strength to be maximum near $\text{VC}_{0.84}$, Figure 25. This maximum occurs in the region where long-range ordering has been observed as discussed earlier. Hollox interprets this maximum in terms of ordering and suggests that ordering is still affecting the mechanical properties at 200°C above the order-disorder temperature. The maximum in strength may also be partially due to a maximum in the bonding similar to that discussed previously in explaining the hardness behavior as a function of stoichiometry for the Groups IV and V carbides. Vanadium carbide is in the transition region where carbon atoms may be donating electrons to d-metal

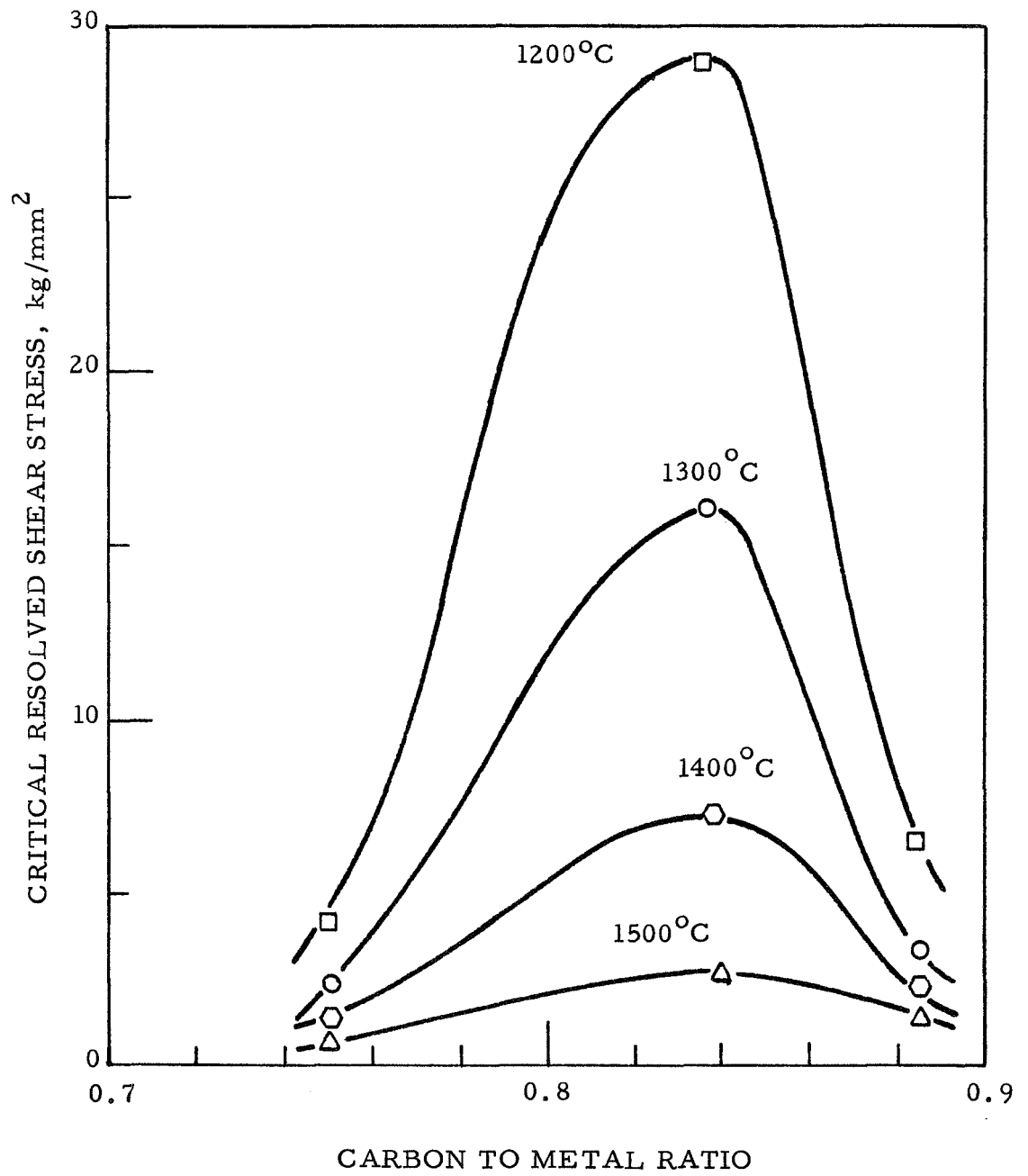


Figure 25. Critical Resolved Shear Stress in VC as a Function of Carbon Composition from Hollox⁽²⁷⁾

orbitals at low stoichiometries and to anti-bonding states at higher stoichiometries. During high temperature diffusion controlled deformation processes the maximum in strength decreases because the effect of carbon atoms on bonding becomes secondary to the role of carbon vacancies.

4.22 Apparatus and Procedure

Yield stress measurements were made using a high temperature graphite furnace (Brew 1080-60KVA) mounted in a constant strain rate machine (Instron 10,000 lb. T.T.C.L.). Specimens were 3/8 inch diameter by 3/4 inch long and were tested in compression. Pyrocarbon platens were used between the specimen and the graphite load train to prevent indentation or deformation of the graphite fixtures. Strain rates were measured from the movement of the crossheads and the yield stress was determined at 0.2 percent offset. Temperatures were measured directly on the specimen with a Milletron two-color pyrometer and were controlled to $\pm 5^{\circ}\text{C}$ with a Leeds and Northrup Speedomax H controller. Testing was done under one atmosphere of helium after normal backfill and purging procedures.

4.23 Results and Discussion

The yield stress as a function of temperature for the Groups IV and V carbides are shown in Figure 26. The yield stress shows a strong temperature dependence indicating that the deformation process is thermally activated up to approximately seven tenths of the melting point. The strength at a given temperature follows the familiar relationship mentioned earlier i.e., that the yield strength increases with decreasing atomic number within each Group.

Williams⁽³⁴⁾ has suggested that an activation energy for deformation can be determined from a plot of log yield stress versus reciprocal temperature. In analysing the yield stress curves he uses the following expression describing dislocation velocity:

$$v \propto \tau^m \exp -(U/kT) \quad (1)$$

where v is the dislocation velocity, τ the stress, m a constant and U the apparent activation energy. Williams assumes the dislocation velocity at the yield stress can be considered a constant independent of temperature at a given strain which defines the yield stress and also that the constant m is not a function of temperature. Consequently for a constant strain rate test

$$(\tau_{y.s.})^m \propto \exp (U/kT). \quad (2)$$

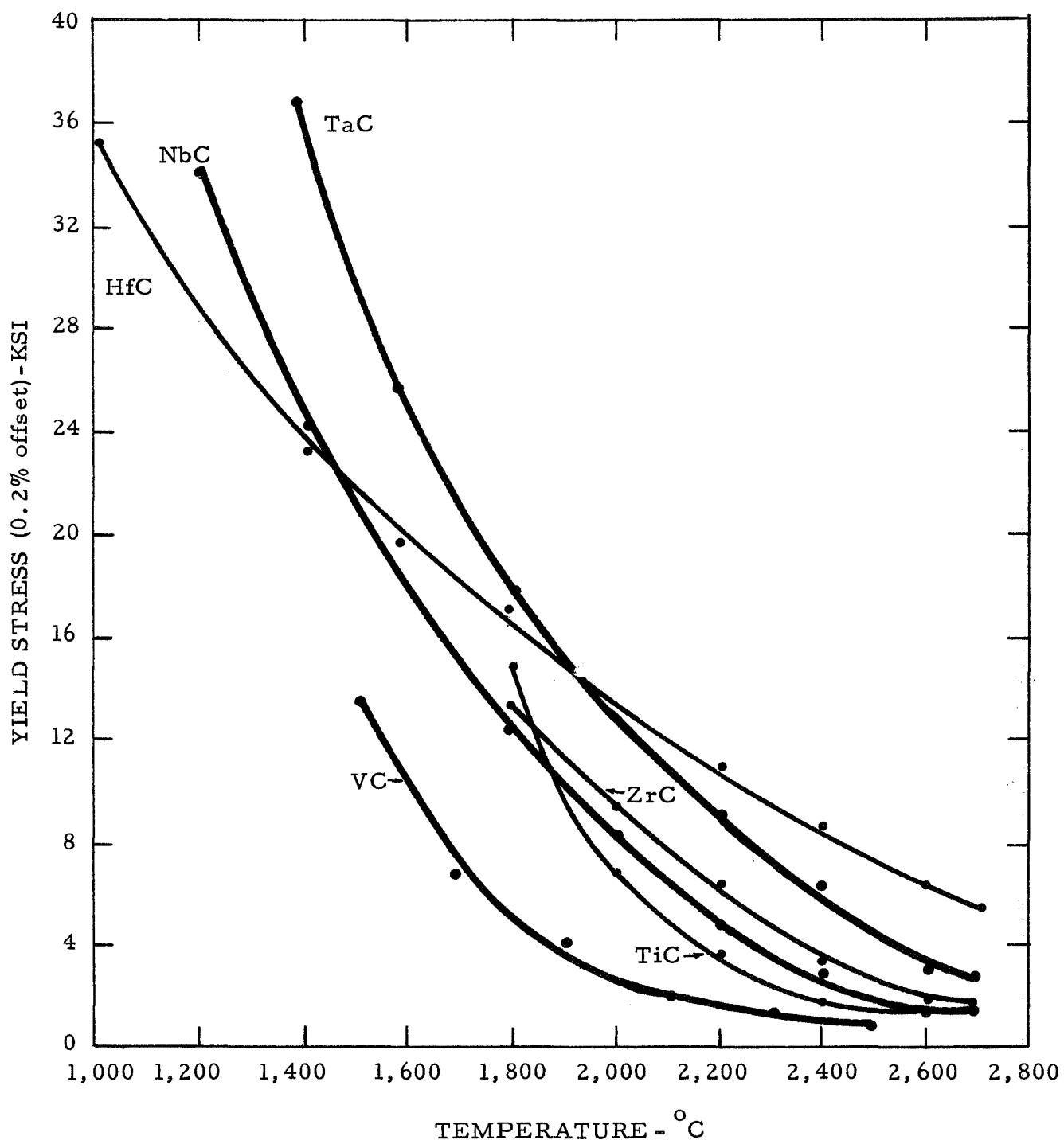


Figure 26. Yield Stress of the Groups IVB and VB Monocarbides as a Function of Temperature

The value of m can be determined from the dependence of strain rate on yield stress⁽³⁵⁾

$$\dot{\gamma} = K_1 \left(\frac{\tau_{y.s.}}{\tau_o} \right)^m \quad (3)$$

where K_1 and τ_o are constants. Williams calculated an activation energy for TiC from the slope of log yield stress vs. reciprocal temperature curve (equation 2 and Figure 27) and from knowledge of the constant m . The activation energy at high temperature is in agreement with the activation energy for self-diffusion, however, the value of the activation energy is strongly dependent on the value of the constant m . Because there is a wide range in reported values for m the calculated value of activation energy varies depending upon which m is chosen.

An interesting observation of the log yield stress vs. reciprocal temperature curve, Figure 27, is its change in slope at lower temperatures. Williams⁽³⁴⁾ suggests that the change in slope signifies a change in activation energy i.e., a change in the deformation mechanism. This proposal appears attractive for carbides since intuitively one would expect that deformation is metal diffusion-controlled at high temperatures and is rate limited by another mechanism at lower temperatures such as a Peierls stress or a carbon diffusion controlled mechanism, the latter being suggested by Kelly and Rowcliffe.⁽³⁶⁾ The present yield stress data was examined for similar

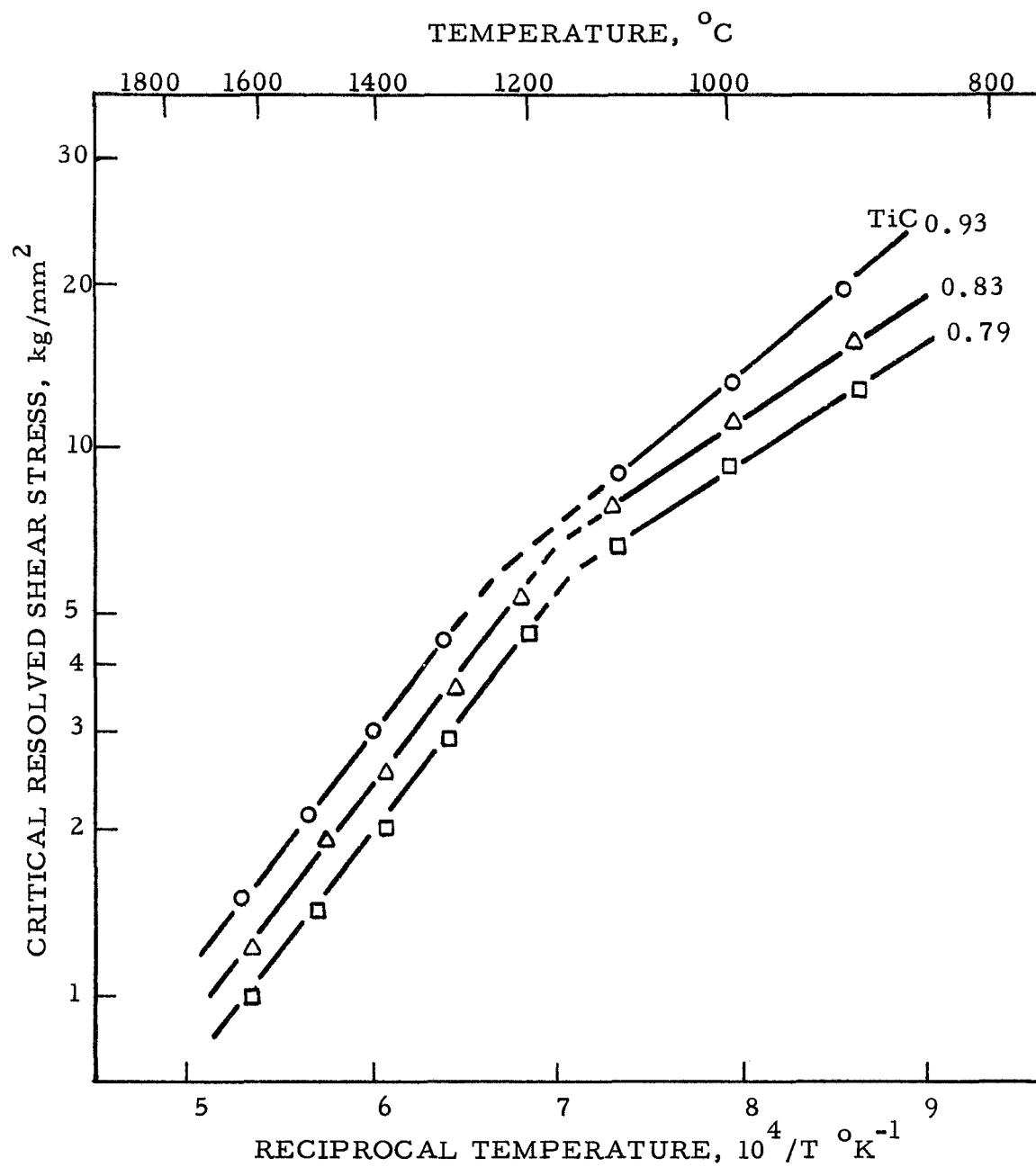


Figure 27. Temperature Dependence of the Log of Yield Stress from Hollox⁽²⁷⁾

changes in slope and the results are given in Figures 28 and 29. A break in the curve did occur for ZrC, HfC and NbC. No apparent break was observed for TiC, VC and TaC which may be due to the fact that the temperature of the investigation did not extend to sufficiently low temperatures. Other deformation data such as total deformation or minimum creep rate after a one hour constant load test was examined for similar discontinuities (to be discussed in Figures 35 through 38). None of the carbides showed an obvious break. Again a possible explanation of why a change of slope was not observed for the other carbides is that the temperature of the investigation did not extend to sufficiently low temperatures. Another explanation for the breaks in the log y.s. vs. $1/T$ curves may be that assumptions of constant m and dislocation density in equation 2 are incorrect. Hollox⁽²⁷⁾ suggested that yield stress data is described by

$$\tau_{y.s.} = A \exp -(BT) \quad (4)$$

where A and B are constants. If equation 4 is correct the data presented in Figure 27 is expected to have a curvature which may be approximated by two straight lines. The present data is presented in Figures 30 and 31 and equation 4 does appear to describe the data.

Williams⁽²⁶⁾ has observed that the yield stress for titanium carbide decreases as carbon is removed from the lattice, Figure 27. This is in agreement with room temperature hardness measurements

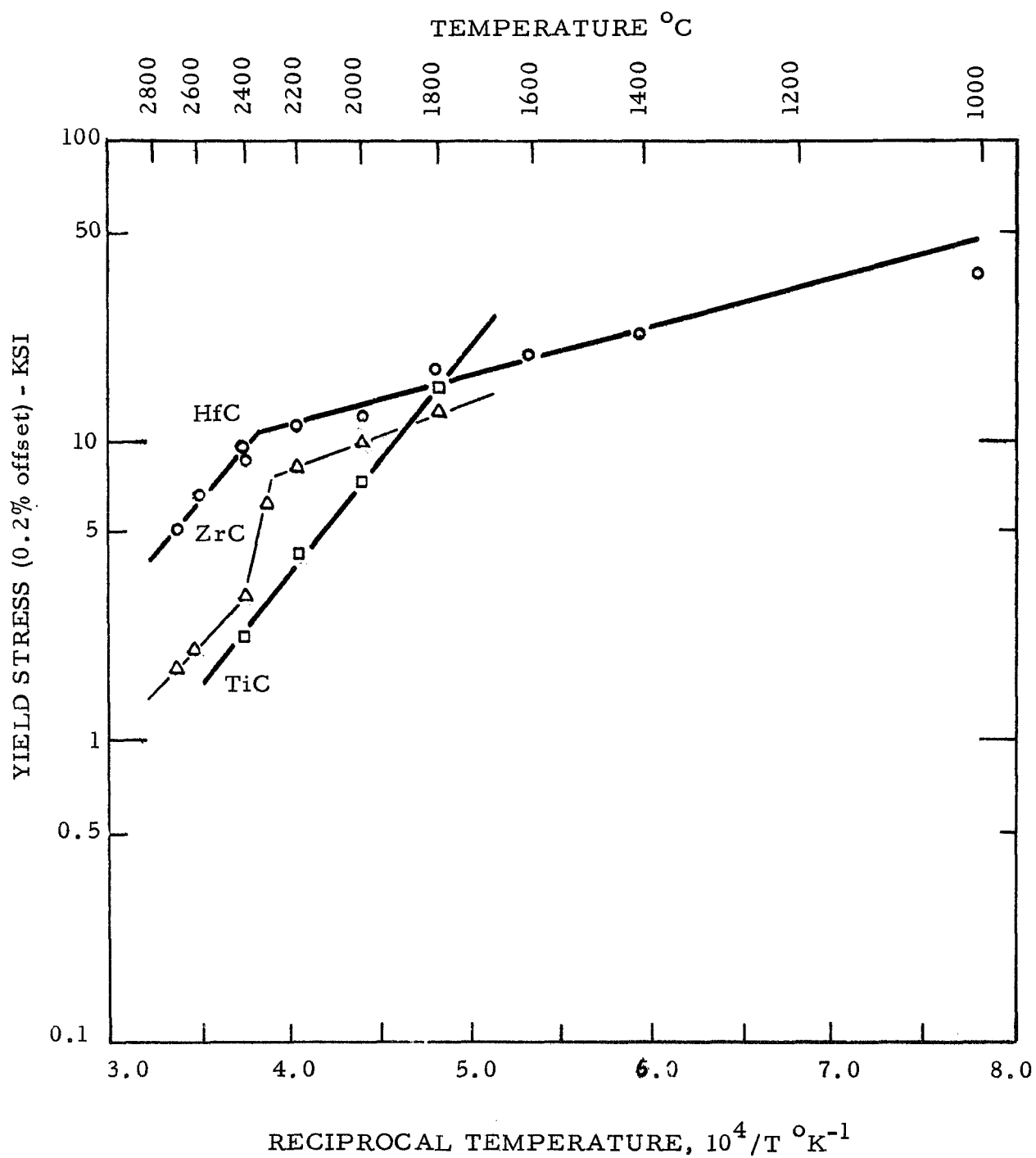


Figure 28. Log of Yield Stress vs. Reciprocal Temperature for the Group IVB Monocarbides

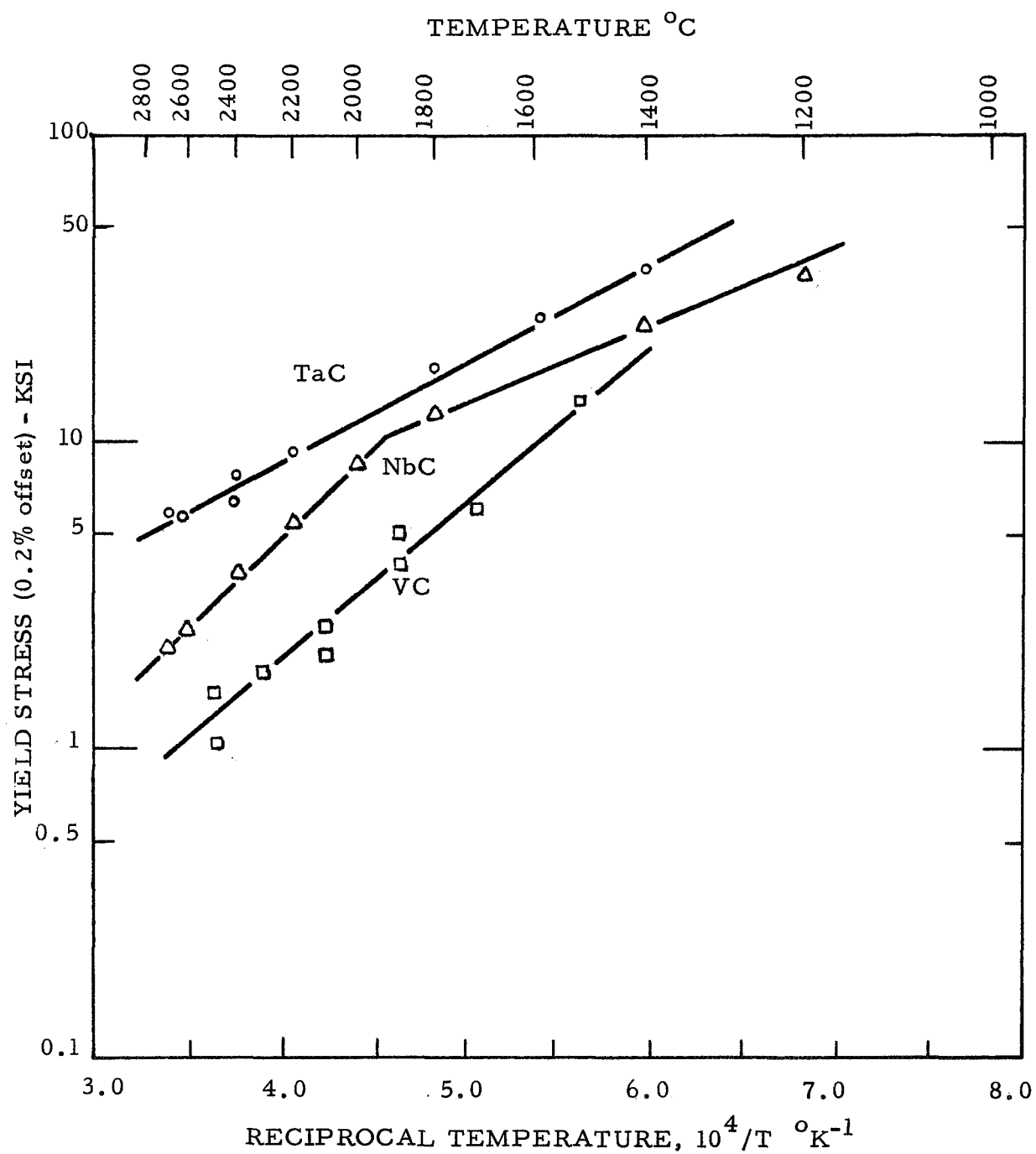


Figure 29. Log of Yield Stress vs. Reciprocal Temperature for the Group VB Monocarbides

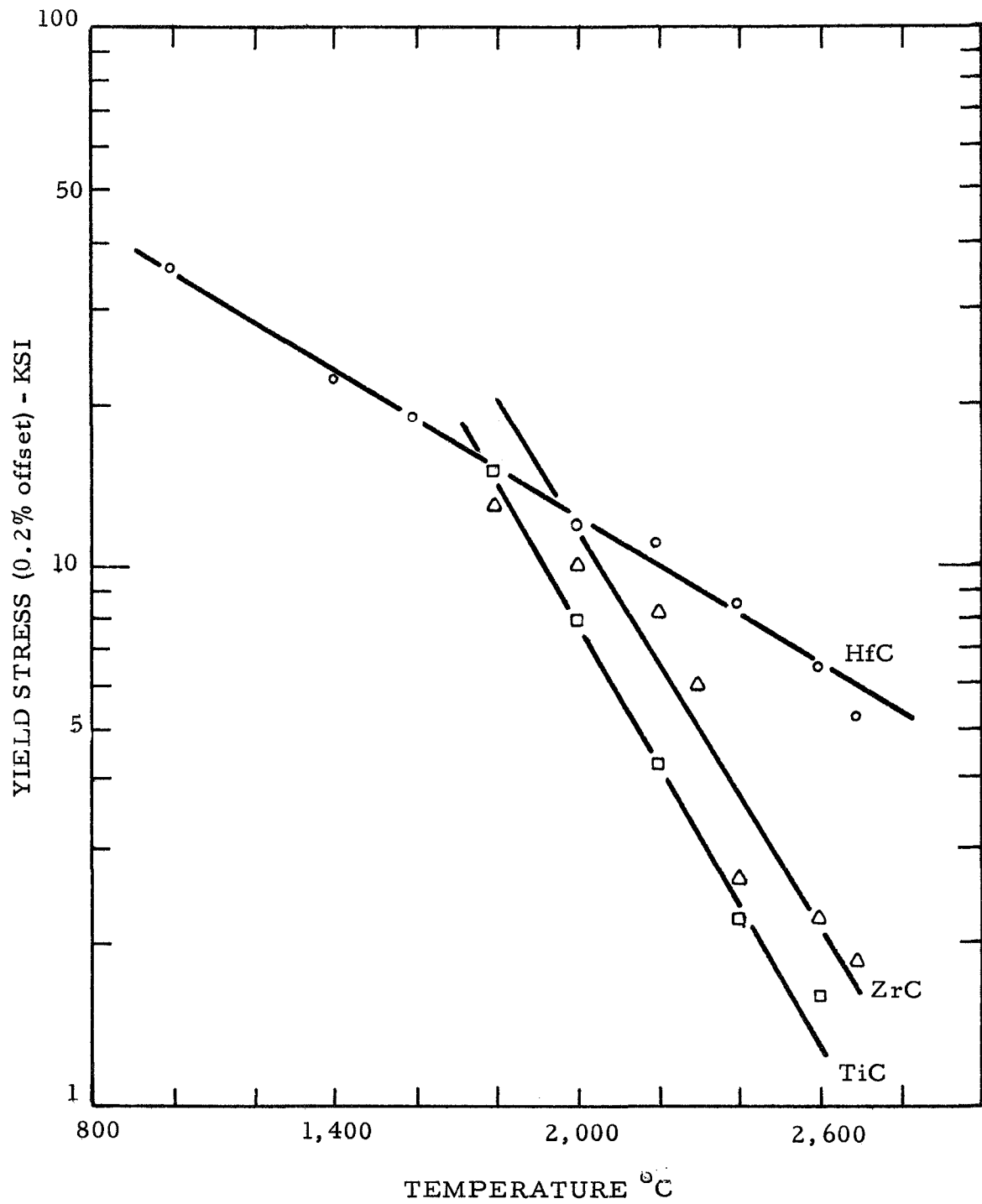


Figure 30. Log of Yield Stress vs. Temperature for the Group IVB Monocarbides

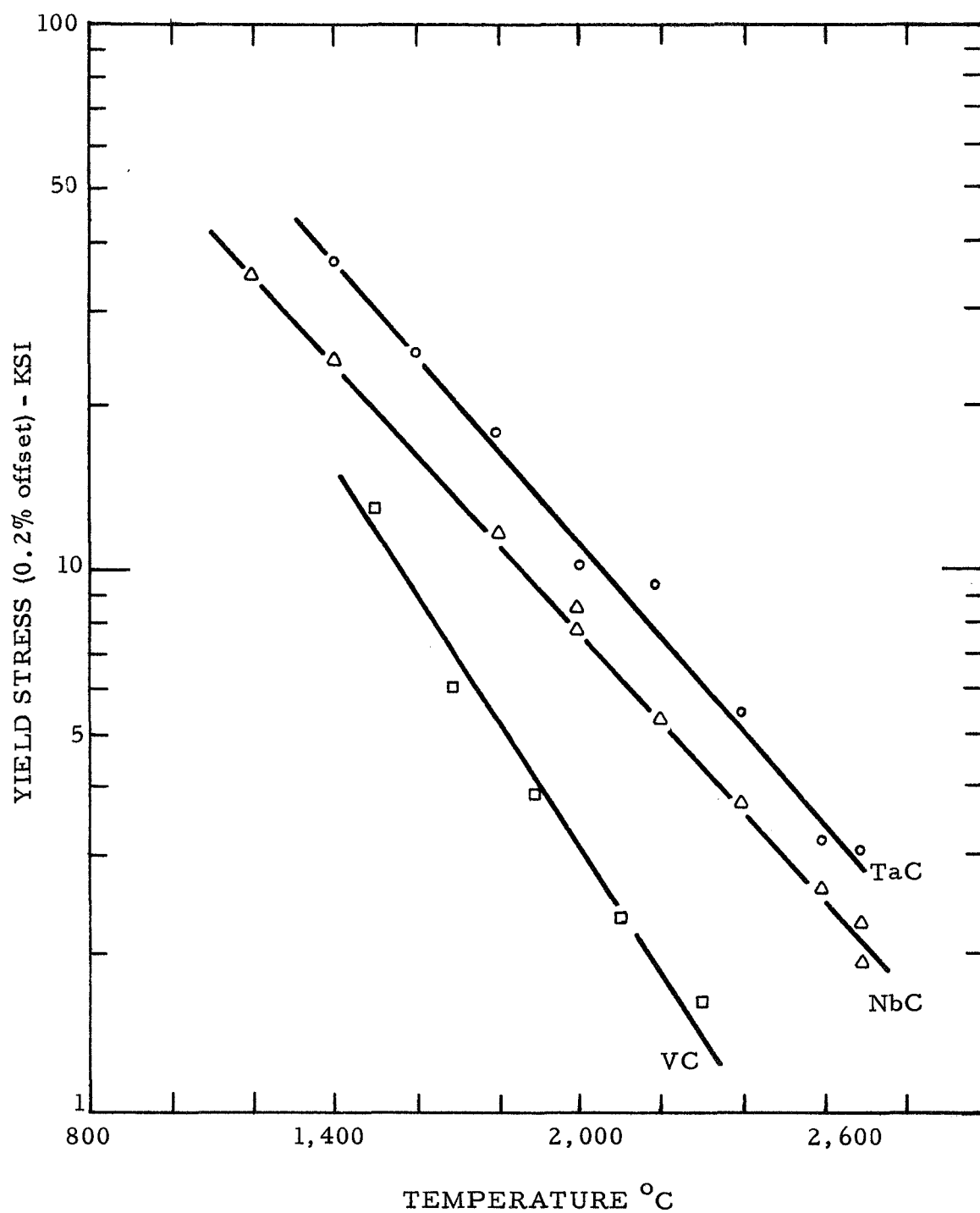


Figure 31. Log of Yield Stress vs. Temperature for the Group VB Monocarbides

discussed earlier and also with diffusion measurements where the diffusivity of both carbon and metal increases with decreasing carbon content i.e., with increasing vacancy concentration. In tantalum carbide, however, room temperature hardness and metal and carbon diffusion increases with decreasing stoichiometry. High temperature yield strength of tantalum carbide was examined as a function of stoichiometry to determine if the yield stress is influenced more by bonding (y.s. increasing with decreasing stoichiometry) or by diffusion (y.s. decreasing with decreasing stoichiometry). The results given in Table 5 indicate that diffusivity of carbon or metal influences deformation more than the difference in bonding that occurs between stoichiometric and substoichiometric TaC. This finding is contrary to that reported by Steinitz.⁽³¹⁾ Steinitz's specimens were made by carburizing solid sheets of tantalum. It is believed that this method produced microcracks which increased with increasing carbon content. This lead to his conclusion that strength drastically decreases with increasing carbon content.

TABLE 5
Yield Stress of TaC and TiC
as a Function of Composition*

	Y.S. at 2000°C (psi)	Y.S. at 2500°C (psi)
TaC _{1.0}	11,500	4,300
TaC _x	11,000	3,800
TiC _{0.96}	5,000	1,900
TiC _x	4,200	1,500

*Low stoichiometry samples were made by partially carburizing metal rods i.e., the diffusion anneal was terminated immediately after the carbide scale reached the center of the specimen.

4.3 Activation Area

4.31 Introduction

The concept of an activation volume to describe the lowering of a thermal barrier by a stress was first proposed by Norwich and Machlin⁽³⁷⁾ (1947). The activation volume can be readily described if we consider the force that acts on a dislocation in its slip plane. According to Li⁽³⁸⁾ if a shear stress (τ^*) does positive work when the dislocation moves forward the free energy of activation, ΔF_o , is decreased by $V^* \tau^*$ where V^* is the activation volume. Thus

$$\Delta F_f = \Delta F_o - \int_0^{\tau^*} V^* d\tau^* \quad (5)$$

and for the backward motion

$$\Delta F_b = \Delta F_o + \int_0^{\tau^*} V^* d\tau^* . \quad (6)$$

Assuming that the average dislocation velocity can be described as

$$v = v_o \exp - \frac{\Delta F}{kT} \quad (7)$$

equations 5, 6 and 7 yield

$$v = 2v_o \exp - \frac{\Delta F_o}{kT} \sinh \left[\frac{1}{kT} \int_0^{\tau^*} V^* d\tau^* \right] . \quad (8)$$

When $\int_0^{\tau^*} V^* d\tau^* \geq kT$, equation 8 can be approximated as

$$v = v_o \exp - \left(\frac{\Delta F_o - \int_0^{\gamma^*} V^* d\gamma^*}{kT} \right) \quad (9)$$

Taking the derivative of equation 9 with respect to stress and assuming

ΔF_o and v_o are independent of stress yields (see Appendix A)

$$V^* = - \left(\frac{\partial (\Delta F)}{\partial \gamma^*} \right)_T \approx kT \left(\frac{\partial (\ln v/v_o)}{\partial \gamma^*} \right)_T \quad (10)$$

Conrad, Hays, Schoeck and Wiedersich⁽³⁹⁾ have used extensively the concept of an activation volume in their studies of low temperature deformation. Li⁽³⁸⁾ has indicated that the term activation volume should be redefined to describe the pressure dependence of dislocation velocity and activation area should be used to describe its stress dependence. Therefore the activation volume and activation area are defined as

$$V^* = kT \left(\frac{\partial (\ln v)}{\partial P} \right)_{T, \gamma^*} \quad (11)$$

$$A^* = \frac{kT}{\bar{b}} \left(\frac{\partial (\ln v)}{\partial \gamma^*} \right)_{T, P} \quad (12)$$

where \bar{b} is the Burgers vector and P the hydrostatic pressure. The activation area is physically the area over which a dislocation must be thermally activated to overcome an obstacle and is defined as

$$A^* = L d \quad (13)$$

where L is the length of a dislocation segment held up at a barrier and d the distance a dislocation must move to overcome the barrier.

Activation area has been used to differentiate between various mechanisms. But due to the possibility of more than one mechanism occurring simultaneously and the large overlap of activation areas for different mechanisms, the use of activation areas in this manner has not been generally accepted. However the activation area is frequently used to distinguish between such mechanisms as climb, Peierls-Nabarro stress, intersection mechanism and nonconservative motion of jogs in which the activation areas are approximately $1\bar{b}^2$, $50\bar{b}^2$, $500\bar{b}^2$ and $500\bar{b}^2$ respectively.⁽⁴⁰⁾ Activation area measurements were made in the present investigation because a Peierls stress was considered a possible rate controlling mechanism in the carbides. Activation area measurements were also needed to obtain true activation energies which will be discussed in section 6.31.

4.32 Apparatus and Procedure

An Instron machine previously described was used to determine activation areas. Specimens 3/8 inch diameter by 3/4 inch long were loaded in compression at a constant strain rate until plastic deformation occurred, the strain rate was instantaneously changed and the new stress was noted. Equation 12 was modified to determine the activation area as

$$A^* = \frac{kT}{\bar{b}} \left(\frac{\partial \ln \dot{\gamma}}{\partial \gamma_A} \right)_T \quad (14)$$

where $\dot{\gamma}$, the crosshead speed, is assumed⁽⁴¹⁾ proportional to the dislocation velocity and τ_A is the measured shear stress. $\partial \tau_A$ was assumed to be equal to $\partial \tau^*$ because

$$\tau_A = \tau^* - \tau_i \quad (15)$$

and τ_i , the internal stress, is considered a constant during each change in strain rate. The internal stress will be further defined in Section 5.0. A schematic of a stress strain curve interrupted by strain rate changes for NbC at 2100°C is shown in Figure 32. The stresses were determined by extrapolating the curve back to the strain where the instantaneous strain rate change was made.

4.33 Results and Discussion

The activation areas as a function of strain, applied stress and temperature are given in Tables 6 through 11 for the Groups IV and V carbides. The activation areas increase with increasing temperature and decrease with increasing strain or stress. In general the activation area is approximately $100b^2$ at one half the melting point. A Peierls stress controlled mechanism is apparently not occurring at the high temperatures studied because the activation area for this mechanism is usually less than $20b^2$ and independent of strain. The activation area for NbC was also determined from yield stress measurements shown in Figure 33 and is in agreement with those

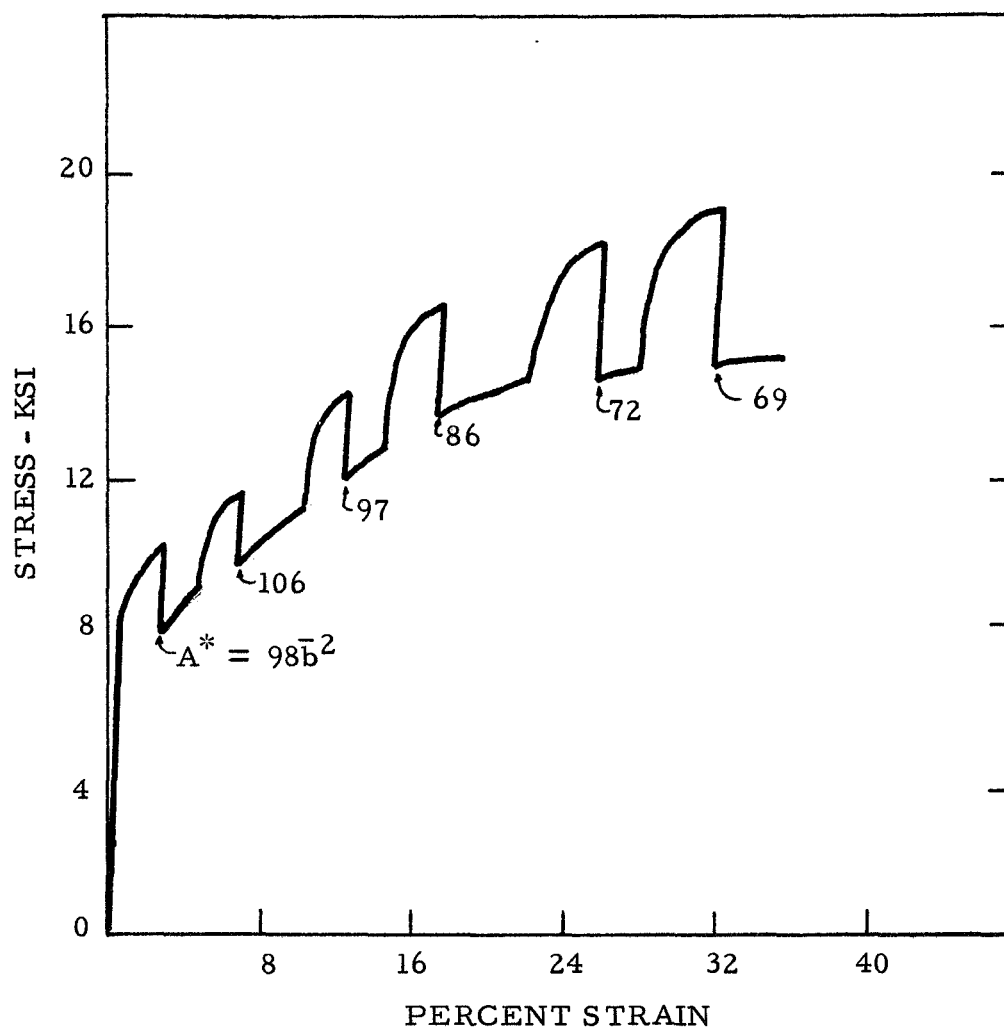


Figure 32. Schematic of a Stress vs. Strain Curve for Determining Activation Areas (NbC, 2100°C, 0.02/min to 0.002/min)

TABLE 6

Activation Areas as a Function of
Temperature and Applied Stress for TiC

Temperature (°C)	Strain Rates (min ⁻¹)	A* (\bar{b}^2)	%Strain	Applied Shear Stresses (psi)
1900	0.005-0.05	68.6	0.4	5,260-6,920
"	"	65.0	6.0	5,550-7,450
"	"	47.4	15.0	5,250-7,625
"	"	49.2	27.2	4,800-7,120
2100	0.005-0.05	92.8	0.8	2,890-4,245
"	"	83.6	5.3	3,125-4,600
"	"	75.0	11.1	3,400-5,150
"	"	67.2	19.5	3,470-5,220
2500	0.005-0.05	466	1.1	1,125-1,440
"	"	346	3.4	1,320-1,740
"	"	260	7.6	1,480-2,045
"	"	258	14.2	1,640-2,240
"	"	195	24.1	1,580-2,320

TABLE 7

Activation Areas as a Function of
Temperature and Applied Stress for ZrC

Temperature (°C)	Strain Rates (min ⁻¹)	A* (\bar{b}^2)	% Strain	Applied Shear Stresses (psi)
1900	0.005-0.05	53.2	0.1	7,270-8,010
"	"	26.6	2.8	7,775-9,300
"	"	20.8	6.9	8,300-10,250
"	"	19.9	12.0	9,000-11,000
2100	0.005-0.05	44.5	1.0	4,582-6,625
"	"	38.2	6.9	5,200-7,550
"	"	45.5	12.8	5,520-7,550
"	"	43.4	21.4	5,620-7,700
"	"	39.7	31.9	5,550-7,800
2600	0.005-0.05	161	2.6	950-1,620
"	"	181	7.9	1,175-1,630
"	"	190	12.4	1,450-2,020
"	"	196	17.3	1,570-2,130
"	"	189	27.7	1,570-2,150
"	"	152	36.5	1,490-2,200

TABLE 8

Activation Areas as a Function of
Temperature and Applied Stress for HfC

Temperature (°C)	Strain Rates (min ⁻¹)	A* (\bar{b}^2)	% Strain	Applied Shear Stresses (psi)
2100	0.005-0.05	82.6	1.3	7,425-8,660
"	"	78.5	4.7	8,220-9,500
2400	0.005-0.05	62.5	0.7	5,040-5,920
"	"	69.5	3.9	6,250-6,900
"	"	41.5	7.4	6,750-7,870
"	"	43.3	13.2	7,425-8,650
2600	0.005-0.05	156	0.9	3,270-4,030
"	"	105	3.8	3,850-4,680
"	"	121	8.0	4,250-5,210
"	"	111	13.7	4,600-5,625
"	"	101	20.9	4,850-6,000
"	"	106	30.1	5,100-6,175

TABLE 9

Activation Areas as a Function of
Temperature and Applied Stress for VC

Temperature (°C)	Strain Rates (min ⁻¹)	A* (\bar{b}^2)	% Strain	Applied Shear Stresses (psi)
1700	0.005-0.05	125	0.63	3,335-4,340
"	"	104	3.89	3,520-4,670
"	"	92.0	8.40	3,530-4,930
"	"	88.5	14.6	3,780-5,200
2100	0.005-0.05	315	3.03	1,655-2,125
"	"	303	6.40	1,800-2,275
"	"	285	10.8	1,965-2,470
"	"	260	16.2	2,080-2,630
"	"	180	26.0	2,080-2,820
2400	0.005-0.05	725	1.3	712-940
"	"	577	4.5	825-1,105
"	"	452	10.4	892-1,250
"	"	337	18.8	805-1,340
"	"	307	29.9	865-1,385

TABLE 10

Activation Areas as a Function of
Temperature and Applied Stress for NbC

Temperature (°C)	Strain Rates (min ⁻¹)	A* (\bar{b}^2)	% Strain	Applied Shear Stresses (psi)
2100	0.002-0.02	98	3.46	4,010-5,200
"	"	106	7.13	4,510-5,520
"	"	97.2	12.8	5,300-6,400
"	"	86.5	18.1	5,800-7,075
"	"	71.5	26.5	5,820-7,270
"	"	69.5	33.4	5,650-7,250
"	"	71.5	42.0	6,200-7,720
2400	0.002-0.02	287	2.03	2,300-2,860
"	"	344	5.90	2,730-3,200
"	"	295	9.35	3,220-3,720
"	"	262	12.4	3,600-4,070
"	"	220	15.6	3,820-4,370
"	"	192	19.1	3,970-4,620
"	"	168	22.5	4,150-4,870
"	"	158	26.4	4,270-5,000
"	"	119	33.3	4,620-5,675
2700	0.002-0.02	338	2.10	1,675-2,075
"	"	335	6.19	2,105-2,510
"	"	312	11.5	2,160-2,590
"	"	223	17.6	2,230-2,850
"	"	114	27.6	1,970-3,180
"	"	171	37.5	2,310-3,105

TABLE 11
Activation Areas as a Function of
Temperature and Applied Stress for TaC

Temperature (°C)	Strain Rates (min ⁻¹)	A* (\bar{b}^2)	% Strain	Applied Shear Stresses (psi)
2100	0.005-0.05	93.8	0.62	5,850-7,035
"	"	92.6	3.67	6,450-7,650
"	"	88.2	6.86	7,000-8,250
"	"	93.5	10.4	7,550-8,750
2400	0.005-0.05	118	1.23	3,795-4,860
"	"	120	3.86	4,170-5,175
"	"	123	6.85	4,560-5,550
"	"	129	10.2	4,940-5,900
"	"	86.5	15.3	5,200-6,650
"	"	88.4	24.0	5,450-6,900
2600	0.005-0.05	170	1.18	2,160-3,425
"	"	184	4.13	3,070-3,780
"	"	182	7.92	3,410-4,150
"	"	153	12.6	3,625-4,480
"	"	139	20.8	3,720-4,680

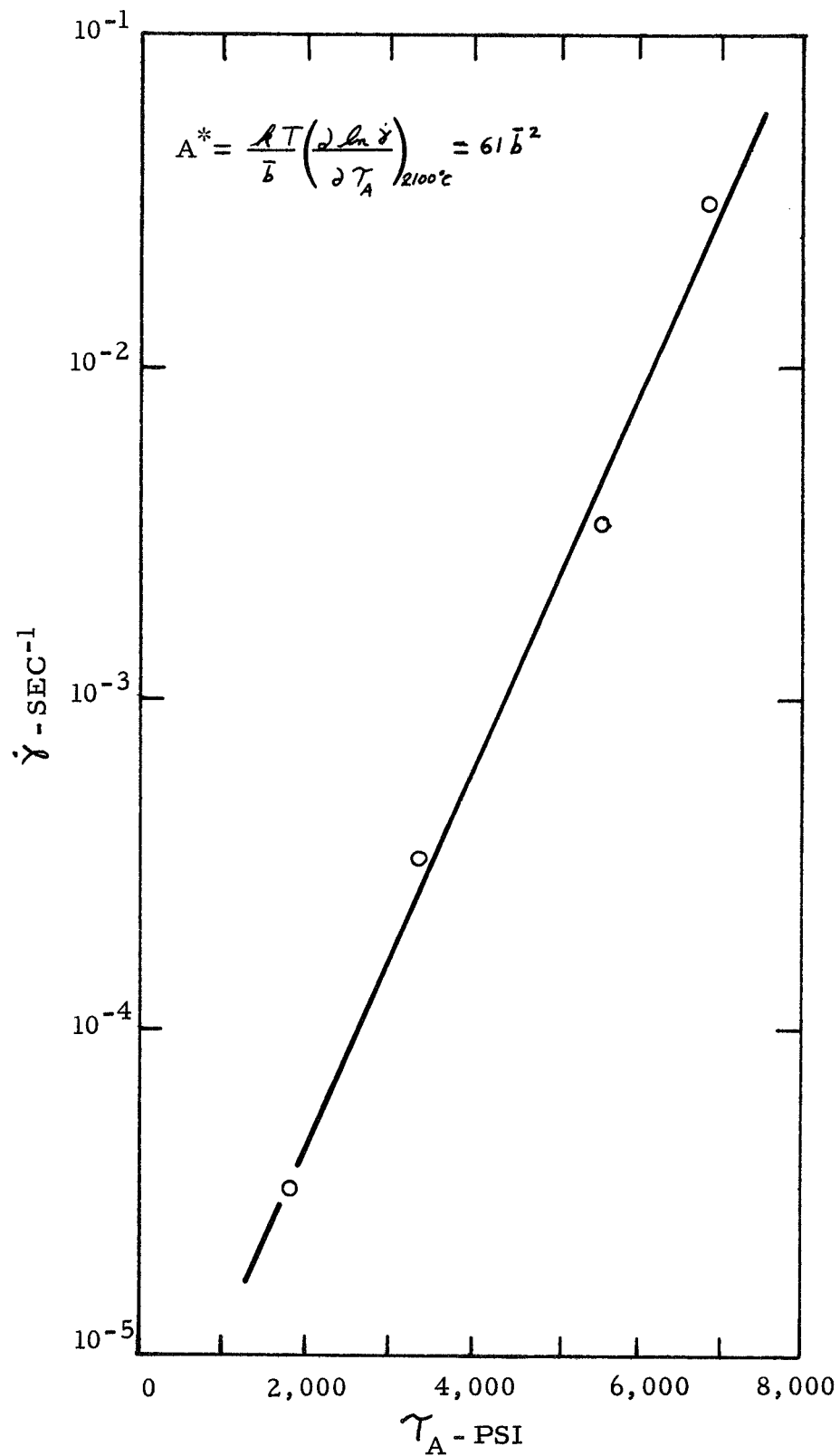


Figure 33. Activation Area for NbC Determined from Yield Stress Data, 2100°C

determined from strain rate change experiments.

The dependence of dislocation velocity on stress can be expressed⁽³⁸⁾ empirically as

$$v = K_2 \left(\frac{\tau^*}{\tau_o} \right)^{m^*} \quad (16)$$

where K_2 , τ_o and m^* are constants. Equation 16 is commonly approximated at small strains by

$$\dot{\gamma} = K_3 \left(\frac{\tau_A}{\tau_o} \right)^m \quad (17)$$

where $\dot{\gamma}$ is the cross-head speed and τ_A the applied stress. Values of m were determined from strain rate change experiments using equation 17 in the following form:

$$m = \left(\frac{\frac{\partial (\ln \dot{\gamma})}{\partial \tau}}{\tau_A} \right)_{T,P} \quad (18)$$

In Table 12 values of m are given and found to usually be between 5 and 15. The value of m was also determined from yield stress data, Figure 34, and was calculated to be equal to 5.3 in agreement with values determined from strain rate change experiments.

Values of m^* were not determined because the internal stress was not known as a function of strain. The values of m^* are expected to be lower than m depending on the value of the internal stress as predicted by Li⁽³⁸⁾.

TABLE 12

Constant m Relating Stress and Strain Rate

	<u>Temperature ($^{\circ}\text{C}$)</u>	<u>m</u>
TiC	1900	8.20
"	2100	6.00
"	2500	7.40
ZrC	1900	16.5
"	2100	5.44
"	2600	3.86
HfC	2100	14.6
"	2400	12.7
"	2600	9.80
VC	1700	8.30
"	2100	8.50
"	2400	9.80
NbC	2100	7.57
"	2400	7.88
"	2700	8.80
TaC	2100	12.0
"	2400	8.30
"	2600	9.65

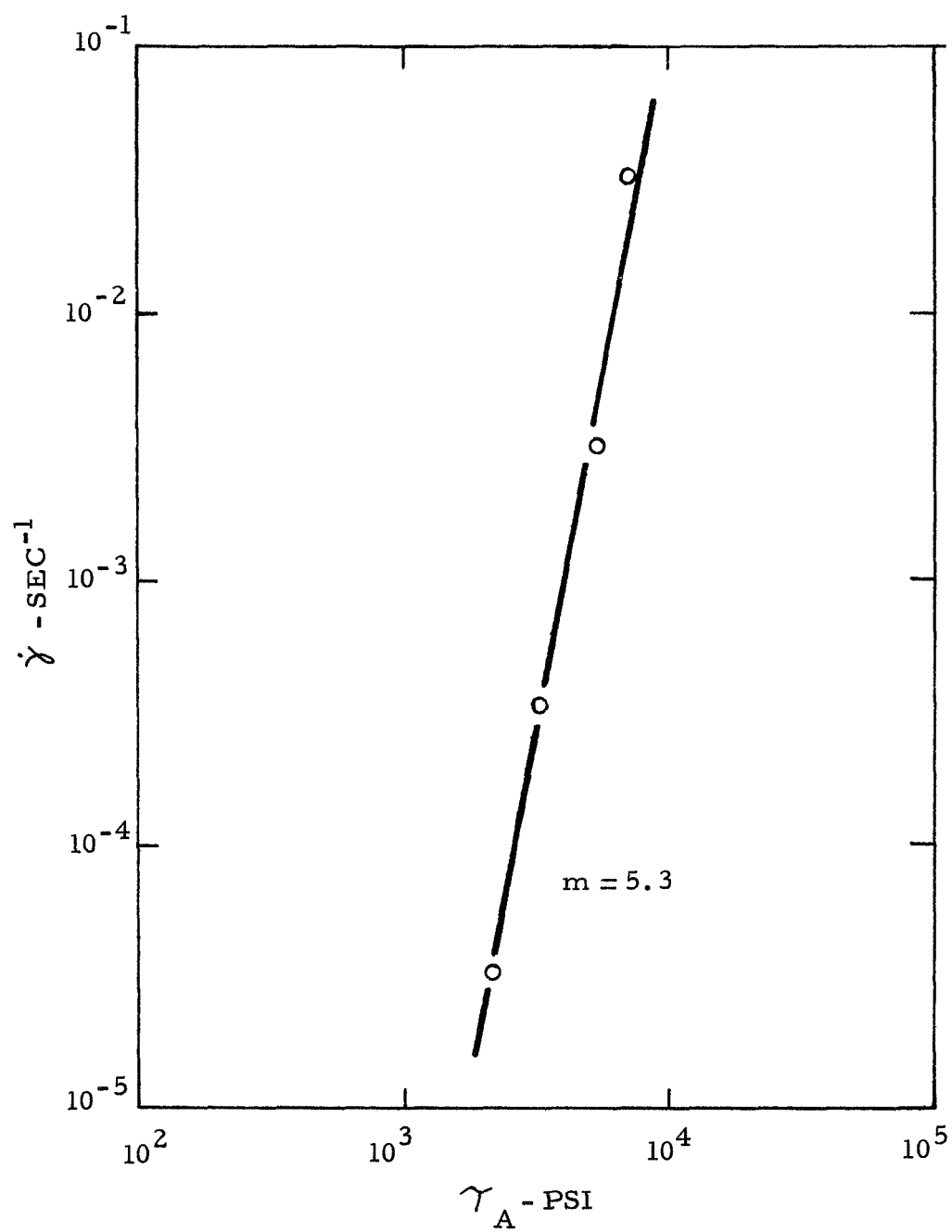


Figure 34. Determination of m from Yield Stress Data, 2100°C

$$\frac{m^*}{m} = \frac{1}{1 - \frac{\tau_i}{\tau_A}} \quad (19)$$

4.4 Constant Load Creep

4.41 Introduction

Very little creep data is available on the transition metal carbides. Williams⁽¹⁸⁾ determined an anomalously low activation energy (23 Kcal/mole) for single crystal titanium carbide. Leipold and Nielsen⁽⁴²⁾ determined creep rates on powder metallurgical samples of zirconium carbide. They concluded that high temperature deformation properties of ZrC could not be determined from impure and poorly characterized samples. Steinitz⁽³¹⁾ studied the creep behavior of tantalum carbide as a function of composition and temperature. His data showed a large amount of scatter probably due to surface cracks which developed during the solid state fabrication method. Keihn and Kebler⁽⁴³⁾ measured creep rates on single crystals of titanium carbide in tension and showed that TiC can undergo large extensions up to 65% before fracture when heated above 1600°C. Their attempts to measure activation energies from constant load tests were unsuccessful. The present constant load tests were made on well characterized one

hundred percent dense samples. The results should assist in design of high temperature structural members fabricated from carbides.

4.42 Apparatus and Procedure

Specimens 3/8 inch diameter by 3/4 inch long were tested in compression in a Bendix Balzers graphite resistance furnace similar to the Brew furnace previously mentioned in section 4.22. Load was applied by a Satec constant load frame and extension was measured using a linear voltage transformer outside the furnace enclosure. Temperatures were controlled to $\pm 2^{\circ}\text{C}$ throughout each test.

4.43 Results and Discussion

Minimum creep rate and total creep at the end of a one hour test are shown in Figures 35 through 38. Hafnium and tantalum carbide which have the highest melting points are the most creep resistant. The creep rate in a compressive constant load test is continuously decreasing and a true steady state condition (linear region) is never achieved due to the increasing cross-sectional area. Because the creep rate for carbides is sensitive to small changes in stress activation energies could not be determined from constant load test. The following expression relates creep rate and stress:⁽³⁸⁾

$$\dot{\epsilon} = K_4 \left(\frac{\tau_A}{\tau_o} \right)^m \quad (20)$$

where m is a constant which has the range of 5 to 15 for the carbides and τ_o and K_4 are constants. For a constant load compression test if m is 5 and τ_A is equal to 5,000 psi the creep rates as a first approximation are in error by greater than 5%, 10% and 25% at 1%, 2% and 5% strains respectively. Thus apparent activation energies determined from constant load tests in tension and compression are invariably too high and too low respectively. The error increases as the temperature range of the investigation is decreased.

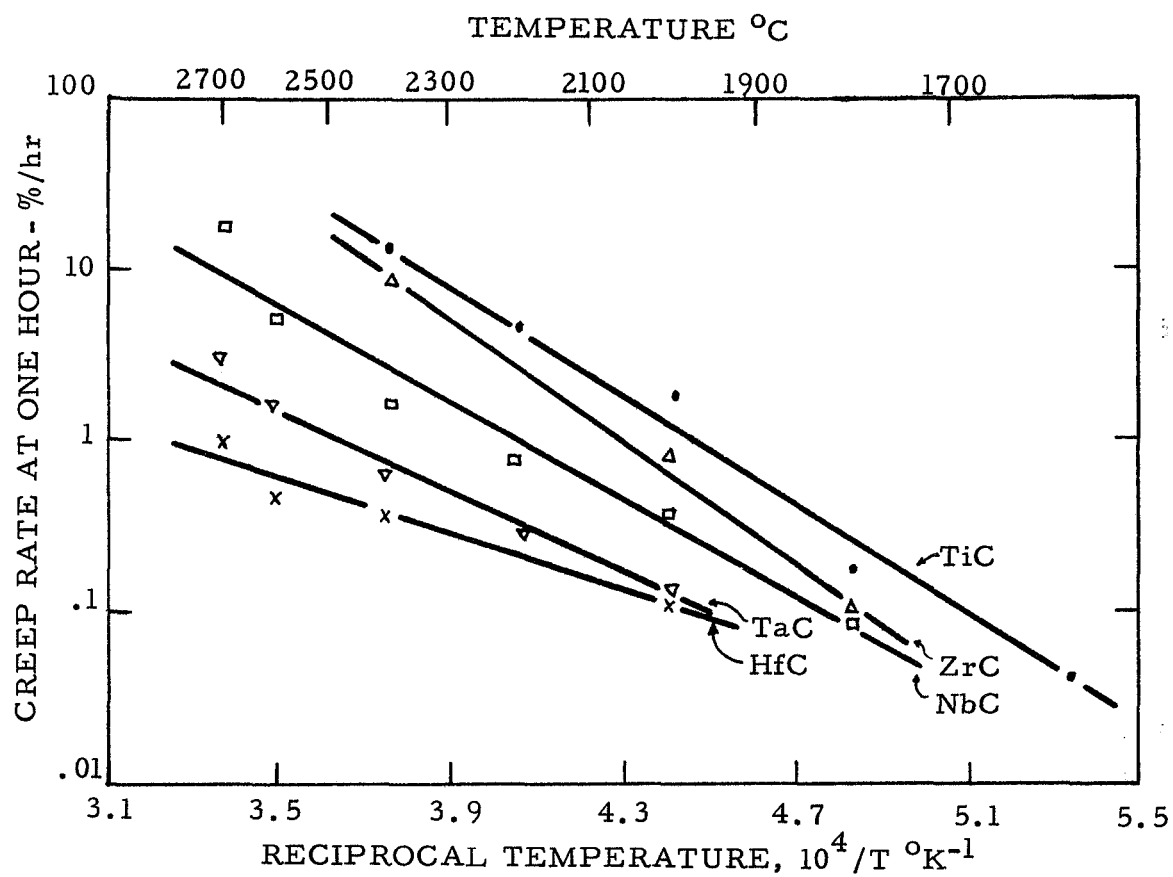


Figure 35. Minimum Creep Rate after One Hour at Constant Load as a Function of Temperature, 4,000 psi

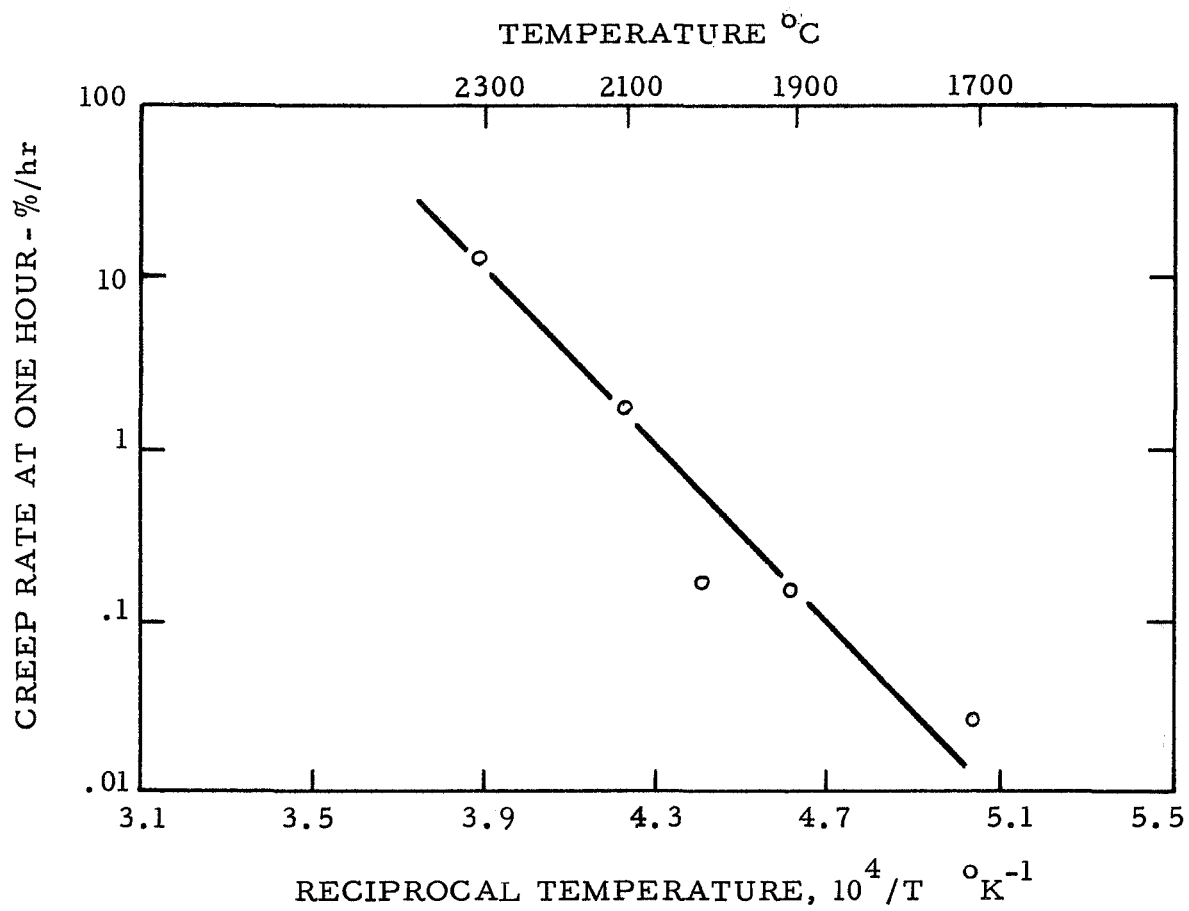


Figure 36. Minimum Creep Rate for VC after One Hour at Constant Load as a Function of Temperature, 2,000 psi

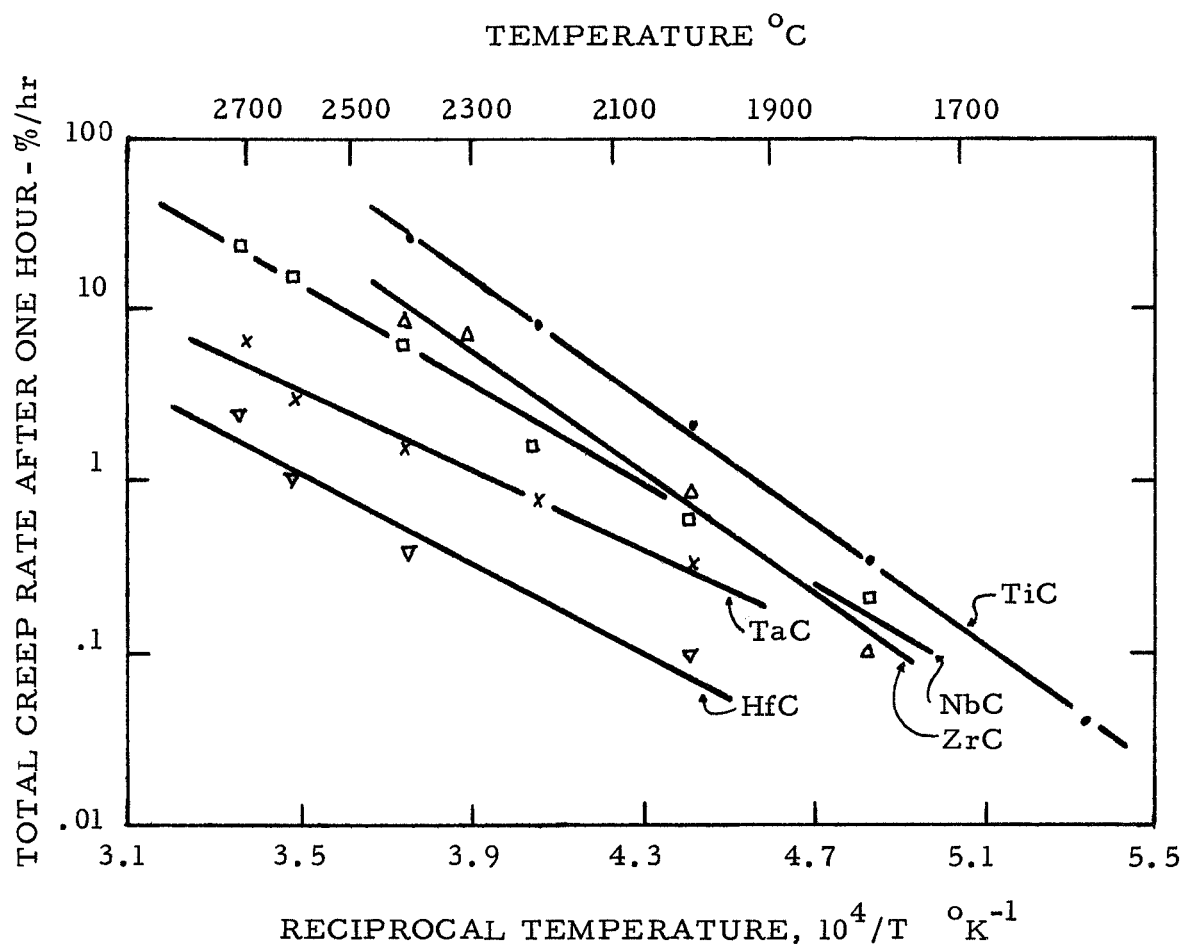


Figure 37. Total Creep Rate after One Hour at Constant Load as a Function of Temperature, 4,000 psi

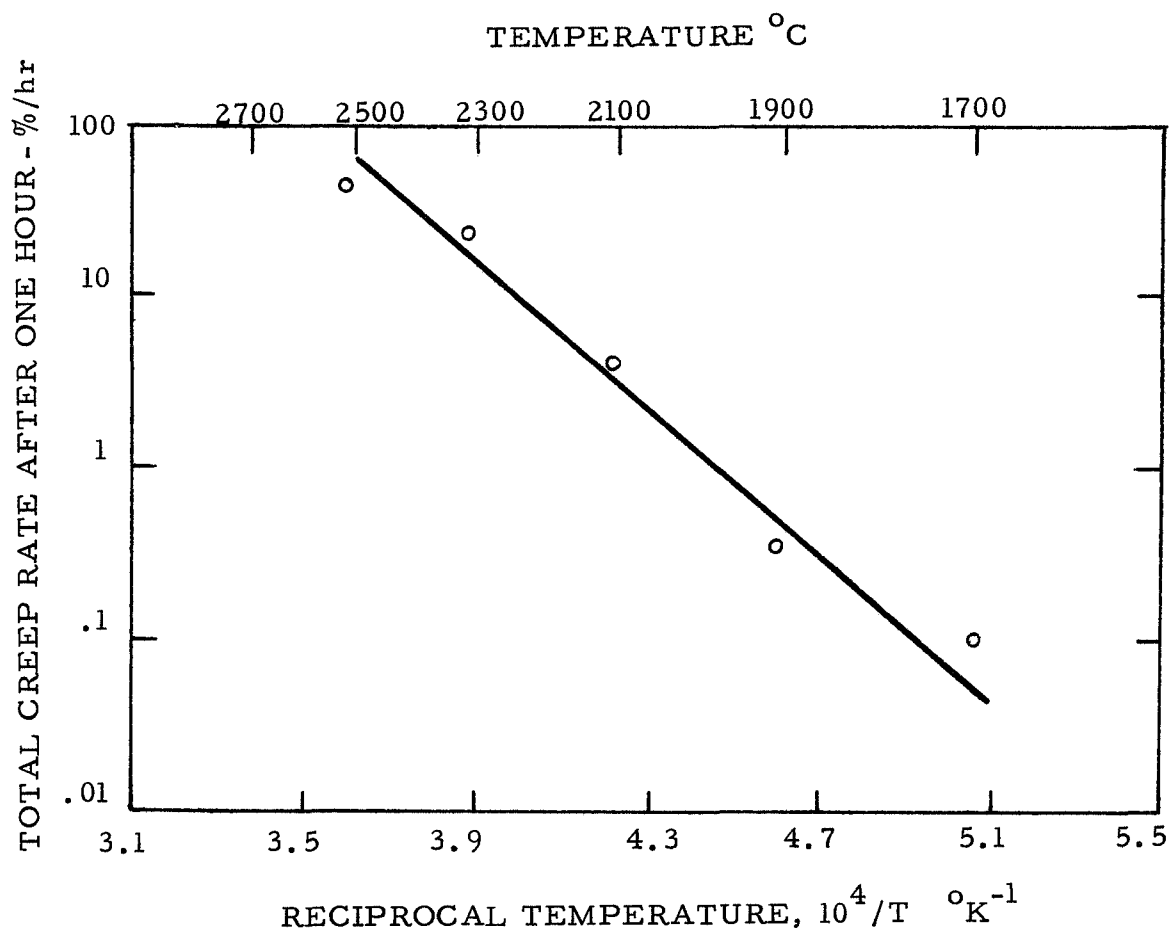


Figure 38. Total Creep Rate for VC after One Hour at Constant Load as a Function of Temperature, 2,000psi

5.0 MODEL FOR CONSTANT STRESS CREEP

Creep under constant stress and temperature conditions is usually studied to gain insight into the mechanism or mechanisms controlling high temperature deformation. Two parameters are usually obtained, namely a stress independent activation energy, ΔH , and the stress dependence of the creep rate, m . These two parameters can be related to creep rate assuming a single rate controlling process as follows:⁽⁴⁰⁾

$$\dot{\epsilon} = K_4 \left(\frac{\gamma_A}{\gamma_0} \right)^m \exp - \frac{\Delta H}{k T} \quad (21)$$

where $K_4 = N A \bar{b} \nu$

N = number of pieces of dislocation likely to slip at any moment

A = area swept out by a dislocation when it slips

ν = frequency of vibration of the dislocation

γ_A = applied shear stress

γ_0 = constant

ΔH = the stress independent activation energy

Weertman⁽⁴⁴⁾ has derived equation 21 for the special case of climb of edge dislocations of opposite sign piled up on parallel slip planes.

Head⁽⁴⁵⁾ and Li⁽⁴⁶⁾, however, have indicated that these pileups never form. Recently it has been recognized by some authors⁽³⁹⁾⁽⁴⁷⁾ that the measured activation energy depends on stress and that recovery

may not be rate controlling in creep but rather that pinning points which restrain bowed-out dislocations may be rate controlling. Assuming entropy effects are negligible the creep rate can be expressed as:

$$\dot{\epsilon} = K_4 \exp - \frac{\Delta Q}{k T} = K_4 \exp - \frac{\Delta H - \int_0^{\tau^*} v^* d\tau^*}{k T} \quad (22)$$

where ΔQ = stress dependent activation energy

ΔH = stress independent activation energy

A^* = activation area

\bar{b} = Burgers vector

$\tau^* = \tau_A - \tau_i$ = shear stress which assists in overcoming a thermal barrier

τ_A = applied shear stress

τ_i = internal stress

The long-range internal stress may be due to the interaction of dislocations on parallel slip planes where the stress field is too large to be overcome by a thermal fluctuation, Figure 39. The force that a dislocation experiences when attempting to overcome a thermal barrier of magnitude ΔH defined in terms of the above mentioned parameters is shown in Figure 40. Assuming the internal stress is constant it can be seen that if a stress greater than the internal stress is applied to a dislocation the dislocation will partially climb the thermal energy barrier thereby reducing the apparent activation

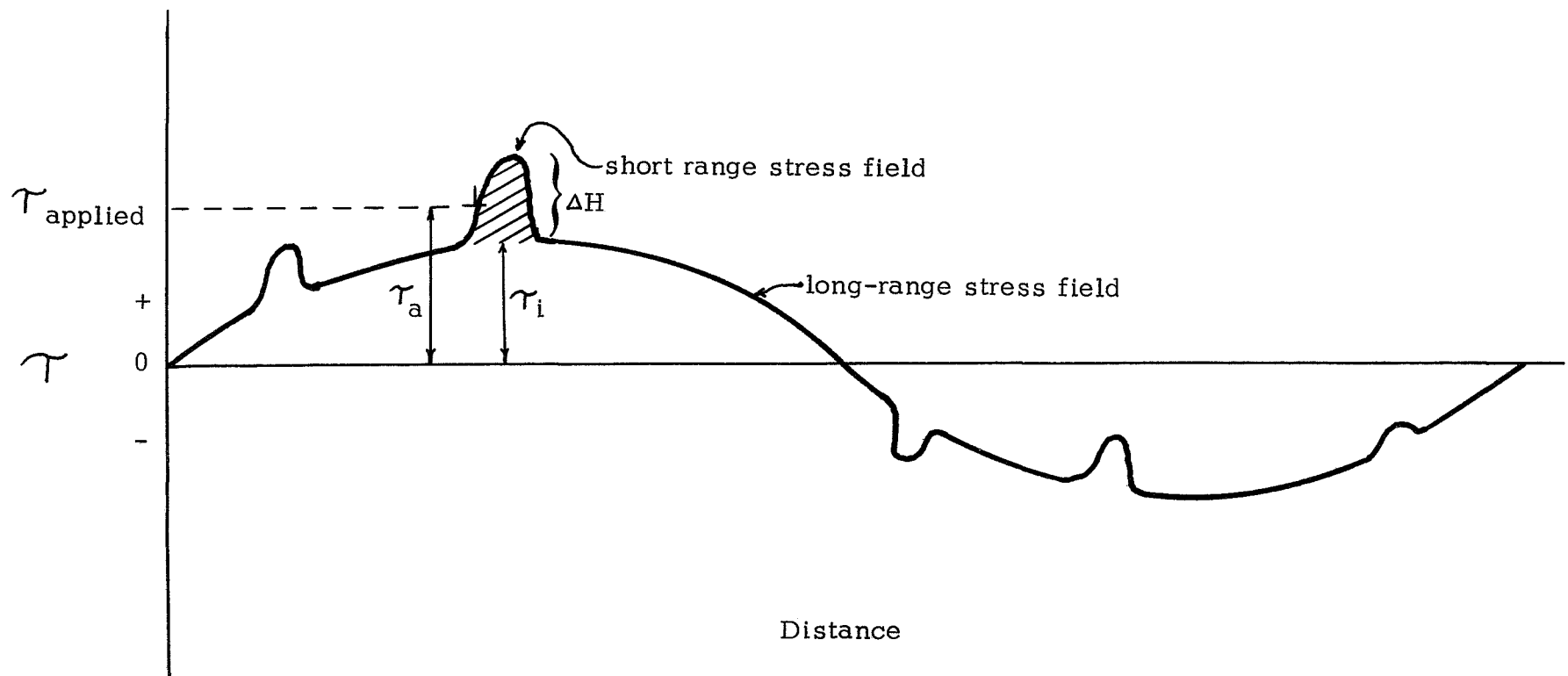


Figure 39. Force vs. Distance for a Dislocation Showing Long - Range and Short - Range Stresses, Conrad⁽³⁶⁾

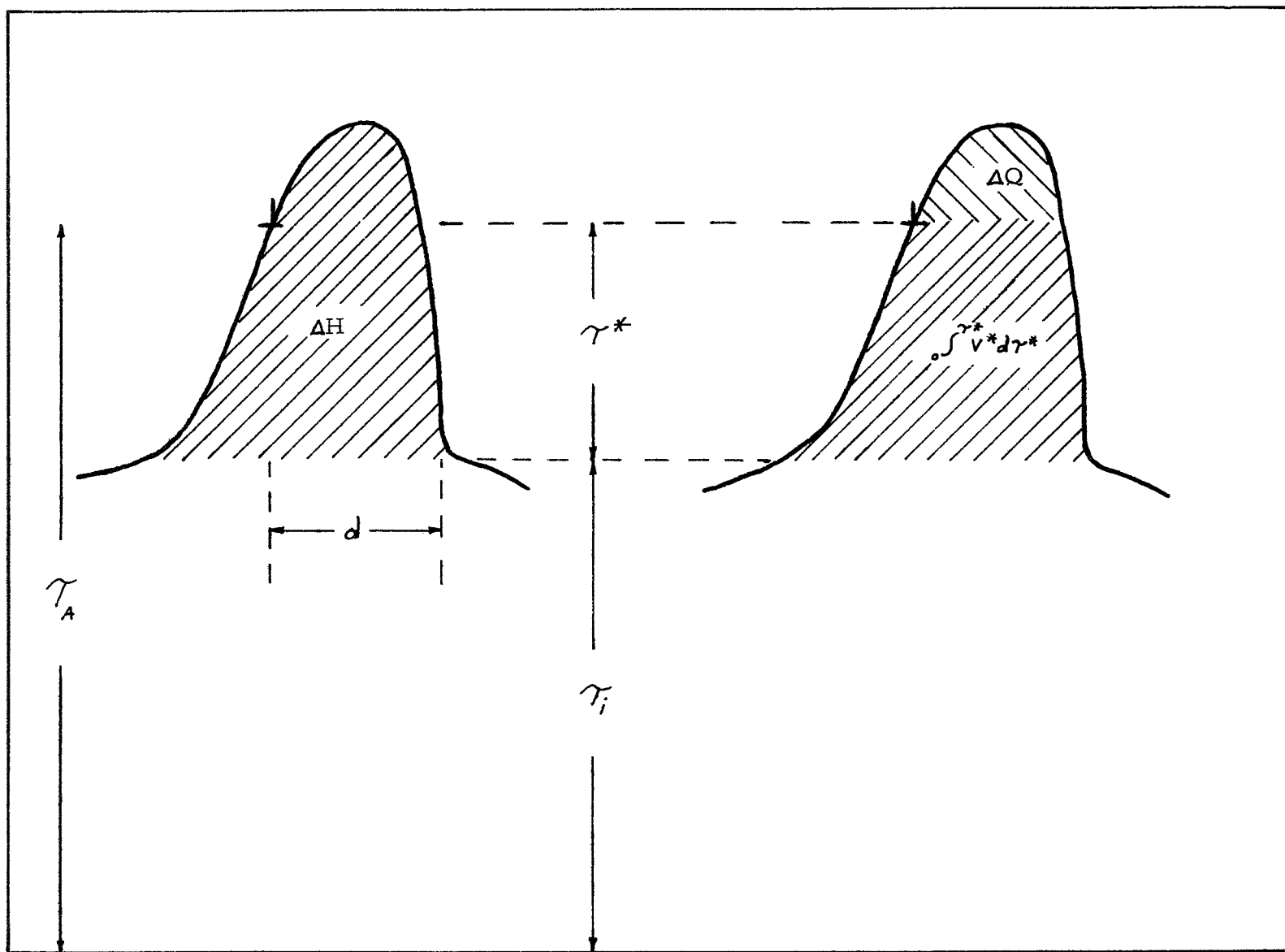


Figure 40. Force vs. Distance Curve for a Dislocation

energy, ΔQ . If the applied stress is increased to the top of the energy barrier, ΔH , no thermal energy is required to overcome the barrier and deformation proceeds uninhibited. This condition rarely exists because as deformation proceeds the internal stress does not remain constant but increases with increasing strain. The increase in the internal stress with increasing strain can be expressed by the following relation:⁽⁴⁸⁾

$$\left(\tau_i\right)^2 \propto \epsilon \quad (23)$$

where τ_i = internal stress

ϵ = strain

ρ = dislocation density

because $\epsilon \propto \rho$ and $\tau_i \propto \left(\rho\right)^{\frac{1}{2}}$.

The effect of strain on the force distance curve is given in Figure 41.

If the applied stress is greater than the internal stress, deformation will commence and if the applied stress is much larger than the internal stress as shown in Figure 41, the apparent activation energy, ΔQ , is reduced and deformation will proceed rapidly. As strain increases the internal stress increases resulting in an increase in ΔQ and a decrease in the deformation rate. As creep or strain continues to increase $\tau_i \rightarrow \tau_A$, $\Delta Q \rightarrow \Delta H$ and $A^{-1} b \tau^* \rightarrow 0$ i.e., all the energy needed to overcome a barrier ΔH must come from thermal fluctuations. If deformation proceeds further to where the internal

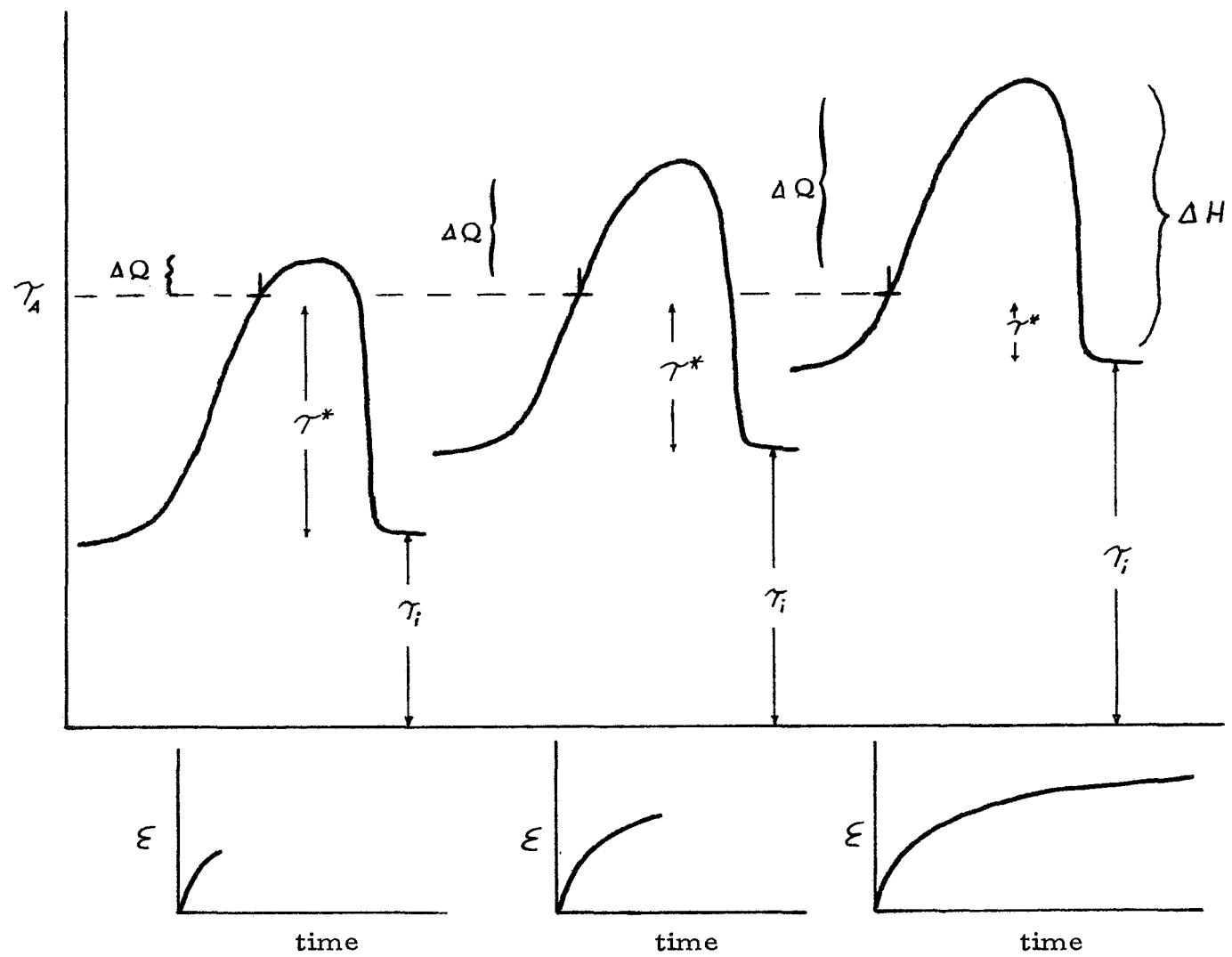


Figure 41. Force vs. Distance for a Dislocation as a Function of Strain

stress attempts to be larger than the applied stress, deformation would cease since a thermal fluctuation can not overcome the long-range internal stress field. This type of creep where the internal stress approaches the applied stress and the deformation rate approaches zero is referred to as logarithmic or low temperature creep. Thus for logarithmic creep the creep rate can be renewed after it has approached zero by increasing the applied stress or the creep rate can be stopped at any strain by reducing the applied stress to less than the internal stress. The total strain for a logarithmic creep test should be predictable if the relationship between internal stress and strain is known. During high temperature creep another process can occur and it is normally referred to as dynamic recovery. That is the internal stress can be reduced by recovery and at high temperatures deformation need not approach zero.

It is apparent from the above discussion that at high temperatures there are two competing processes. They are the increasing internal stress due to deformation and a decreasing internal stress due to dynamic recovery. The initial or transient region of creep where creep rate is at first very fast and then decreases with time occurs when the rate of increasing internal stress is greater than the rate of dynamic recovery. Steady state creep occurs when the internal stress remains constant. Thus the apparent activation energy observed for

steady state creep, ΔQ , is shown in Figure 40 to depend on the steady state values of γ^* and γ_i .

6.0 APPLICATION OF MODEL TO NbC

6.1 Creep of NbC at Constant Stress

6.11 Introduction

Determination of the apparent activation energy during constant stress experiments is normally determined by one of two methods. The first method involves measuring the creep rate after steady state has been achieved during a constant temperature test on a single specimen. Another specimen is used and the test is rerun at a different temperature. The apparent activation energy is determined from equation 22 as

$$\Delta Q = K_4 \left(\frac{\ln \frac{A_1}{A_2} + \ln \frac{\dot{\epsilon}_2}{\dot{\epsilon}_1}}{\frac{1}{T_1} - \frac{1}{T_2}} \right) = K_4 \left(\frac{\ln \frac{\dot{\epsilon}_2}{\dot{\epsilon}_1}}{\frac{1}{T_1} - \frac{1}{T_2}} \right) \quad (24)$$

The difficulty with this method is that the structure may change from specimen to specimen thus affecting the assumption that the constant A_1 equals A_2 . The second method involves a differential temperature technique i.e., after steady state has been achieved at a given temperature the temperature is changed and a new steady state creep rate is determined on the same specimen. This method has the advantage that because the temperature change is made rapidly on the same specimen at approximately the same strain the term A

can be considered a constant. The disadvantage over the first method is that both the temperature and creep rates must be known accurately because the differential in temperature is normally less than 50°C . The latter method was chosen for the present investigation but because of the difficulty in measuring creep rates at temperatures in excess of 2000°C the temperature differential was 200°C .

6.12 Apparatus and Procedure

The apparatus used for compressive constant stress experiments was previously described for constant load tests (section 4.42) with the exception that loads were manually adjusted during a creep test to maintain a constant stress to within one percent. Temperatures were read with a two-color pyrometer and controlled to $\pm 2^{\circ}\text{C}$. Temperature changes of 200°C were made within four minutes and an additional six minutes were needed to stabilize the system. An extremely stable system was needed because strain was measured outside the furnace enclosure. Small changes in temperature when made over the length of the load-train would produce a significant apparent strain. Samples were crept for twenty minutes after a temperature change was made and creep rate was determined by extrapolating the creep to the strain where the temperature change was made. Creep rates less than one percent per hour could not be reliably measured and creep rates

greater than ten percent per hour did not allow enough temperature cycles per sample. A test condition of 2020°C and 2220°C at 6,000 psi was found to be ideal.

6.13 Results and Discussion

A typical differential creep test is shown in Figure 42 with the apparent activation energies determined after each temperature change. The initial stage of the creep curve is clearly in the transient region and the apparent activation energies determined in this region are generally lower which could result from a larger value of τ^* as discussed in section 5.0. After steady state is reached the measured value of the apparent activation energy, ΔQ , is 130 kcal/mole and is relatively reproducible and independent of strain. Values of the apparent activation energies determined on a number of different samples are given in Table 13.

From the model presented earlier the apparent activation energy, ΔQ , is dependent on stress and is not equal to the rate controlling activation barrier, ΔH , unless τ^* is equal to zero. One can attempt to measure the stress dependence of the apparent activation energy by performing creep tests at different stresses, however, this was not done for two reasons. Firstly, because the measureable creep rates in the present work were limited to an order of magnitude change,

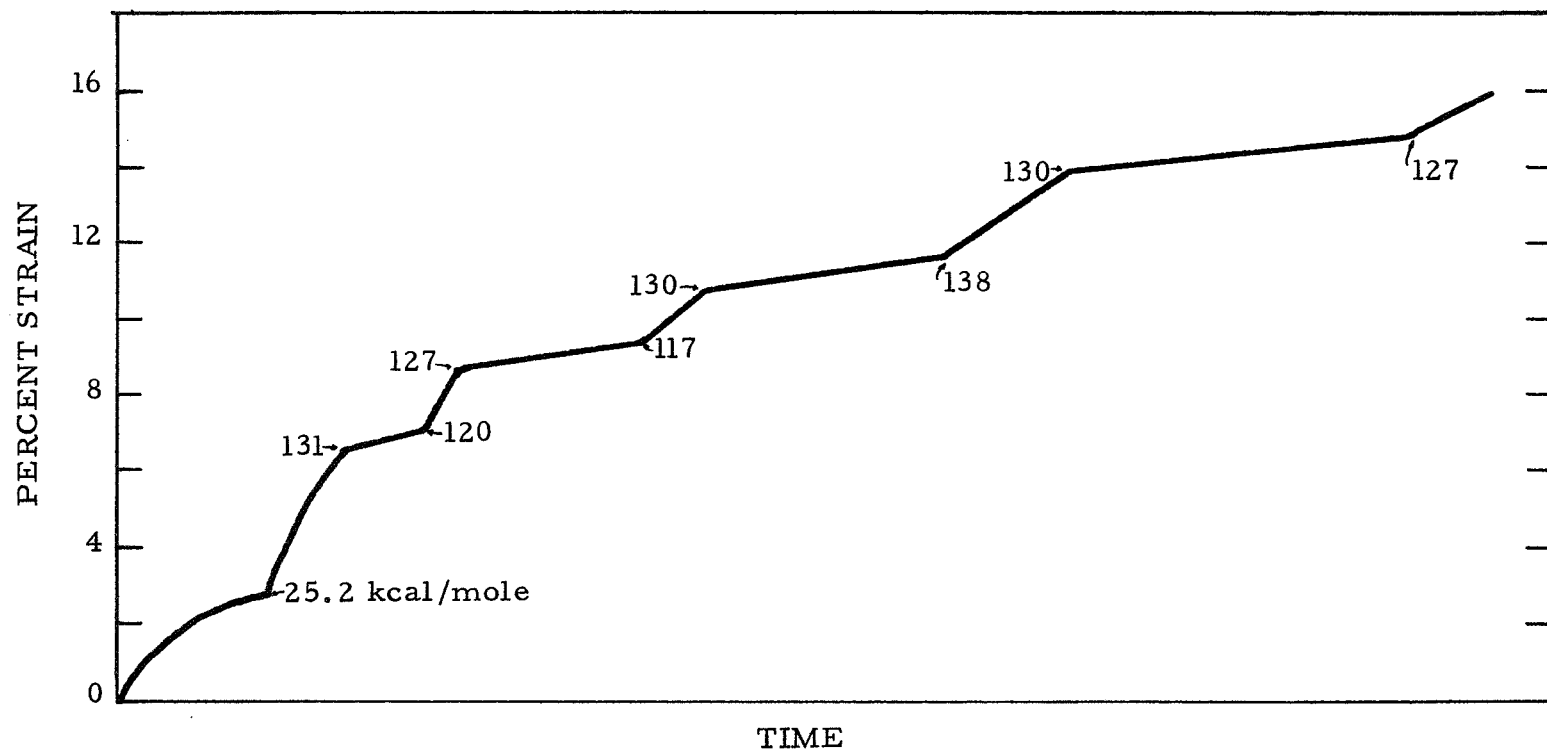


Figure 42. Schematic of a Differential Creep Test for NbC at 2020 to 2220 °C at 6,000 psi

TABLE 13

Apparent Activation Energies for NbC
Determined from Instantaneous Temperature
Changes at Constant Stress (2020°C to 2220°C at 6,000 psi)

Temp.	Specimen #1		Specimen #2		Specimen #3*	
	Strain (%)	Q (kcal/mole)	Strain (%)	Q (kcal/mole)	Strain (%)	Q (kcal/mole)
Low	2.86	25.2	2.60	29.1	3.66	130
High	6.48	131	6.40	130	8.80	117
L.	7.25	120	7.10	140	9.50	105
H.	8.70	127	8.20	107	10.95	126
L.	9.50	117	9.40	97	11.45	103
H.	10.7	130	11.3	103	12.5	131
L.	11.8	138	12.2	119	13.2	125
H.	13.6	130	13.9	141	13.9	127
L.	14.3	127	15.4	136	14.4	121
H.	15.8		17.1		15.1	

* Specimen was stress relaxed after testing.

the difference in the apparent activation energy with stress would only be 5.9 kcal/mole at 2100°C calculated from equation 22

$$\Delta Q = kT \ln \left(\frac{\dot{\epsilon}_1}{\dot{\epsilon}_2} \right). \quad (25)$$

This change in the apparent activation energy is within the experimental accuracy of ΔQ and would not verify its stress dependence. Secondly, if the internal stress also increases with the applied stress, the apparent activation energy may show little dependence on the applied stress.

It is clear from the model previously discussed that the apparent activation energy depends on the applied stress because creep rate increases with the applied stress. Therefore to be consistent with experimental measurements τ^* must increase to a new steady state value determined by the work hardening and recovery rates when the applied stress is increased during steady state creep. Therefore the effect of the applied stress on the apparent activation energy can not be determined unless τ^* or τ_i is known. Thus to determine the stress dependence of the apparent activation energy it is necessary to assume that it is stress dependent and then to determine both the internal stress, τ_i , and the thermal component of stress, τ^* .

Another possible explanation of why the creep rate increases with increasing stress is that the mobile dislocation density may be

increasing with increasing stress. The mobile dislocation density was not measured in the carbides so that it is not known whether this explanation is plausible. Li⁽³⁸⁾ has indicated that the agreement of activation areas determined from dislocation velocity measurements and from strain-rate change experiments suggest that the density of mobile dislocations does not change significantly. It is therefore assumed that the stress dependence of the creep rate arises from the stress dependence of dislocation mobility i.e., γ^* ,

6.2 Determination of the Internal Stress

6.21 Introduction

The internal stress is the stress that arises from long-range interactions of dislocations. Possible types of dislocation-dislocation interactions giving rise to long-range internal stresses has been discussed by Jonas.⁽⁴⁹⁾ The width of the stress field is approximately $10,000\bar{b}$ whereas the width of barriers that can be overcome by thermal energy are approximately $100\bar{b}$. The internal stress is commonly determined from yield stress versus temperature curves. The internal stress is equal to the yield stress when it becomes athermal i.e., when the thermal energy is large enough to overcome thermal barriers at the imposed strain rate without the assistance of

stress. For example, NbC, Figure 26 becomes athermal at approximately 2600°C. As temperature is lowered τ_i increases in proportion to the elastic modulus. The modulus as a function of temperature has been determined over a limited range of temperatures for NbC as shown in Figure 43. Because high temperature elastic modulus determinations are difficult and can be subject to error internal stress values determined at lower temperatures using this method are not considered reliable. It is believed that a more accurate method of determining internal stresses at any given temperature is by stress relaxation measurements.

6.22 Apparatus and Procedure

An Instron machine previously described for yield stress determinations (section 4.22) was used to determine the internal stress. Samples were loaded in compression at 0.02 inches per minute until plastic deformation occurred. The machine was stopped and the specimen relaxed i.e., the specimen is crept under a continually decreasing stress until all the thermal barriers are overcome. Because the internal stress is approached asymptotically with time, log of the slope of the relaxation curve verses load was plotted and the internal stress was determined at a slope equal to zero. The relaxation of the machine was investigated by removing the specimen and loading the platens at the temperatures and stresses to be investigated and then stopping the machine. No relaxation was detected.

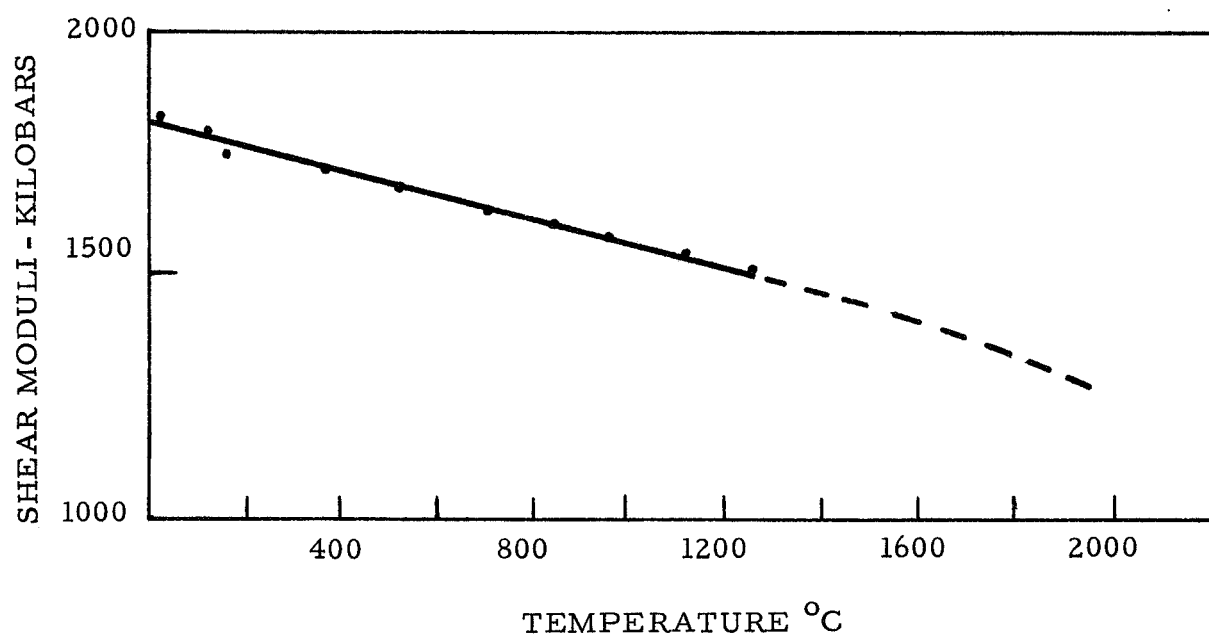


Figure 43. Shear Modulus of NbC as a Function of Temperature⁽⁵⁰⁾

6.23 Results and Discussion

A typical stress relaxation curve is shown in Figure 44. The internal stress is found to be approximately 65 percent of the applied stress at 2100°C, Figure 45. The value of the internal stress can be in error if either strain aging or recovery is taking place during relaxation. Strain aging is not believed to be occurring because upon reloading a yield point was not observed. Some recovery is undoubtedly occurring but the amount was not evaluated. Therefore the reported internal stresses may be slightly underestimated.

The relation between internal stress and strain was examined by successively straining and relaxing a single specimen. The results are given in Table 14. From the data obtained the internal stress can be described as increasing with the square root of strain (Figure 46) predicted previously in equation 23. This same relationship is expected to describe the internal stress as a function of strain in the transient region of creep. Also the internal stress at zero strain is in agreement with the internal stress determined from yield stress data (Figure 26) after correcting for the change in elastic modulus with temperature.

It can be seen from Figure 44 that τ^* is increasing slightly with increasing strain during a constant strain rate experiment. This is probably due to a decreasing activation area with increasing strain as

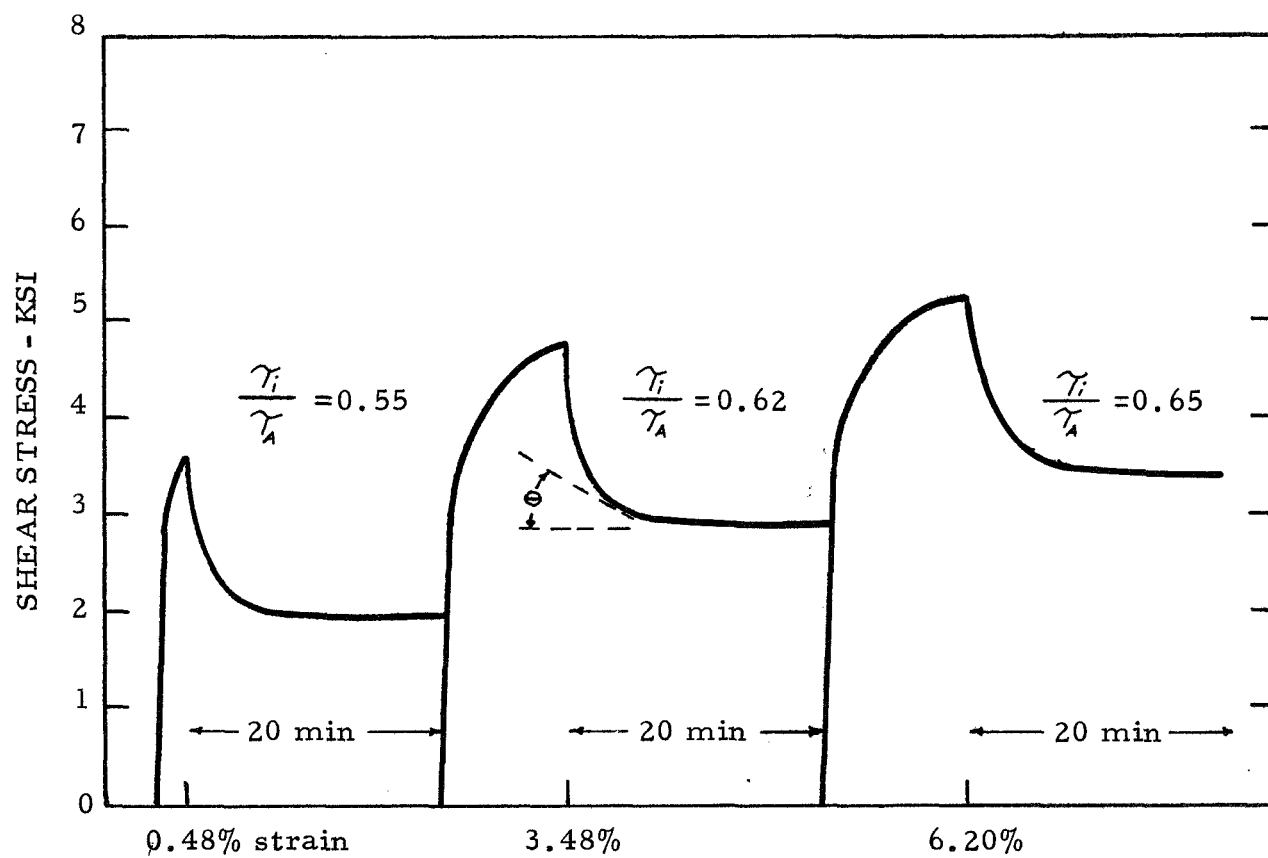


Figure 44. Schematic of Stress Relaxation Curves for NbC at 2100°C, 0.02/min

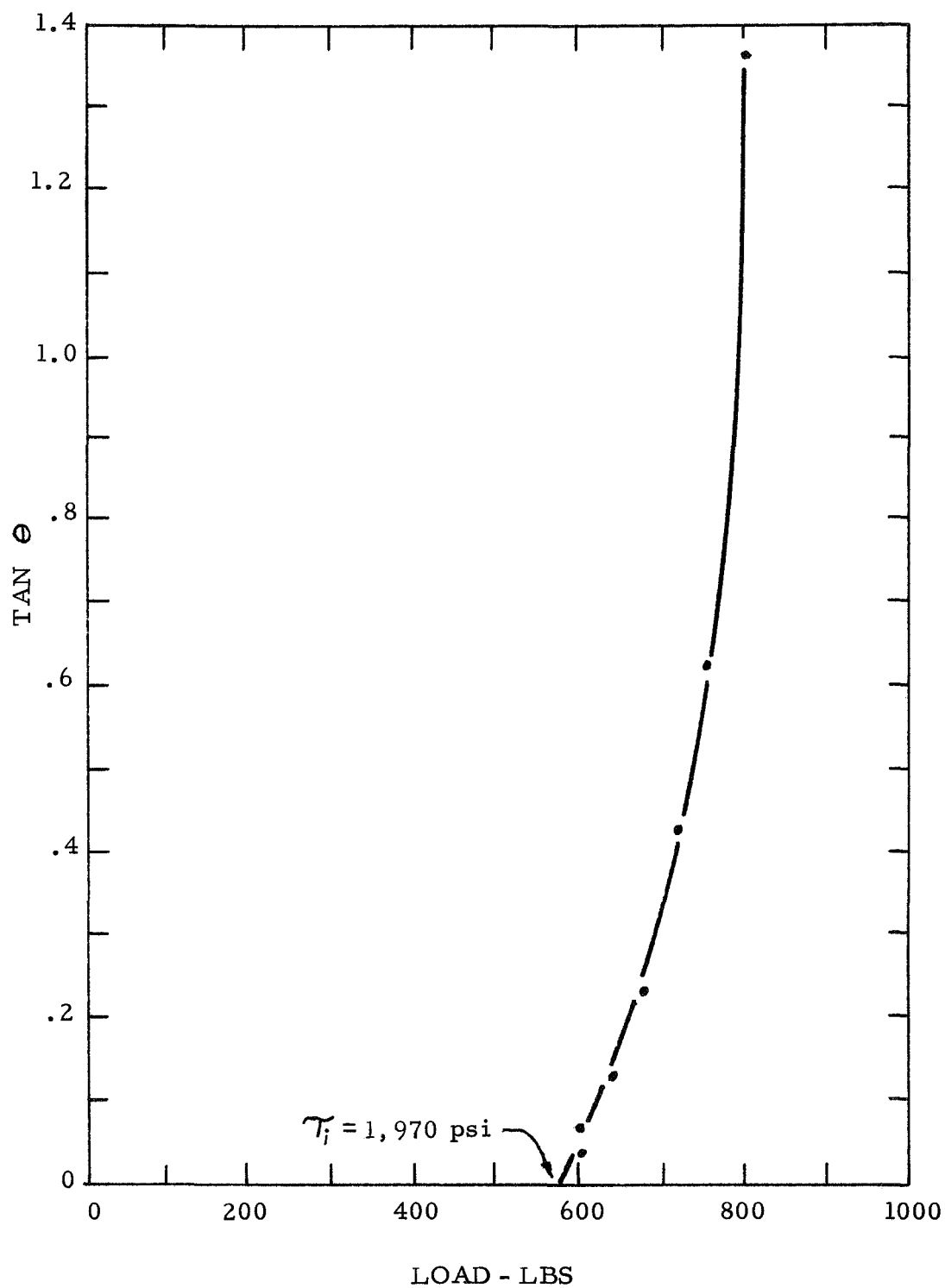


Figure 45. Determination of τ_i from Stress Relaxation Curve at 0.48% Strain, Figure 44, Cross-Sectional Area = 0.147 in²

TABLE 14

Internal Stresses in NbC Determined from Stress Relaxation Experiments

Specimen #4				Specimen #5				Specimen #3*			
Temp. (°C)	Strain (%)	γ_i (psi)	γ_A (psi)	Temp. (°C)	Strain (%)	γ_i (psi)	γ_A (psi)	Temp. (°C)	Strain (%)	γ_i (psi)	γ_A (psi)
2100	0.48	1,970	3,610	2100	0.48	1,780	2,830	2220	15.1	2,330**	3,000
"	3.48	2,990	4,770	"	2.37	2,340	3,800	"	17.2	3,200	4,650
"	6.20	3,450	5,310	"	8.32	3,340	4,770	"	18.7	3,370	4,950
2400	7.43	2,540	3,910	2400	10.9	2,280	3,570				
"	10.1	2,470	4,000								
"	12.9	2,520	4,070								
2100	14.7	3,640	5,220								
"	17.1	3,850	4,850								
"	19.4	3,760	5,900								

* Specimen stress relaxed after creep at 3,000 psi, Table 13.

$$** \frac{\gamma_i}{\gamma_A} = 78\%$$

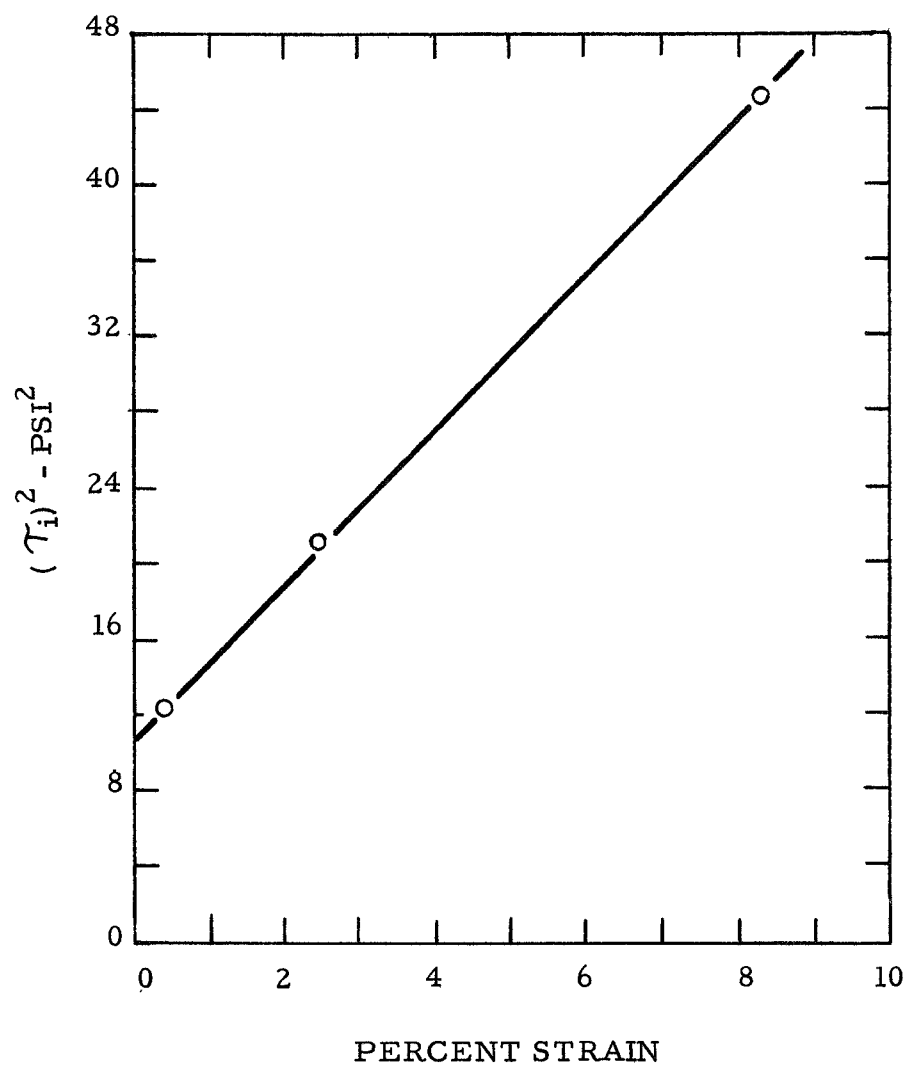


Figure 46. Internal Stress of NbC as a Function of Strain at 2100°C

shown previously in Tables 6 through 11. It is shown in equation 22 that when the strain rate is constant $A^* \bar{b} \gamma^*$ is also constant and A^* and γ^* are thus inversely proportional to each other.

The value of γ_i was determined on a specimen after being crept in the steady state region (Specimen #3, Table 13). The results are given in Table 14 and indicate that the internal stress is at least 78 percent of the applied stress during steady state creep at 2220°C.

6.3 Determination of the Activation Energy ΔH

6.3.1 Results and Discussion

From section 6.1 the activation energy, ΔH , can be expressed by the following expression:

$$\dot{\epsilon} = K_4 \exp \left(- \frac{\Delta H - V^* \gamma^*}{kT} \right) \quad (26)$$

Differentiating equation 26 with respect to temperature according to Conrad⁽⁵¹⁾ yields

$$\Delta H = kT^2 \left(\frac{\partial \ln \dot{\epsilon}}{\partial T} \right)_{\gamma} + kT^2 \left(\frac{\partial \ln \dot{\epsilon}}{\partial \gamma} \right)_{T} \frac{\gamma}{A} \frac{\partial A}{\partial T} + kT \left(\frac{\partial \ln \dot{\epsilon}}{\partial \ln \gamma^*} \right)_{T} \quad (27)$$

The first term describes the apparent activation energy, ΔQ ; the second term is the correction for the change in elastic modulus during a differential temperature test. The last term is the correction

for the stress dependence, γ^* , on the activation energy. The first term was evaluated by measuring the creep rate before and after a temperature change and the values were given previously in Table 13. The second term was approximated from the effect of strain rate on instantaneously changing stress; the results were given in Table 12. The temperature dependence of the shear modulus is given in Figure 43 and the internal stress was calculated in the preceeding section. The third term was determined from the change in the steady state creep rate after a change in applied stress. γ_i was assumed to be 78 per-cent of the applied stress as determined in the previous section.

Evaluating equation 27

$$\Delta H = 130 - 11.7 + 37 = 155 \text{ kcal/mole.}$$

The activation energy for chemical diffusion of carbon in niobium carbide has been determined⁽⁶⁾ to be 98 kcal/mole. The activation energy for self diffusion of carbon in NbC has not been measured. The difference in the activation energy for chemical and self diffusion has been estimated⁽⁵²⁾ for zirconium carbide to be 15 kcal/mole. If the same activity composition relationships also occur in niobium carbide the activation energy for self diffusion of carbon in NbC would be equal to approximately 115 kcal/mole.

The activation energy for self diffusion of niobium in NbC has not been measured. However it can be approximated using LeClaire's⁽⁵³⁾

relationship ($\Delta H = 38 \times m.p.$) to be equal to 143 kcal/mole.

Comparison of the activation energy for creep (155 kcal/mole) with that for diffusion indicates that ΔH_{NbC}^C is too low and that ΔH_{NbC}^{Nb} is in fair agreement considering that LeClaire's relationship is an empirical expression which is being extended for carbides. If it is assumed that deformation is controlled by niobium diffusion, three types of deformation mechanisms can be considered to be rate controlling, namely, viscous flow, climb and nonconservative motion of screw dislocations. Viscous flow is not considered a possibility since the measured stress dependence is not unity. For dislocation climb the activation area is expected to be near lb^{-2} and the measured activation areas are one to two orders of magnitude larger, Tables 6 through 11. Nonconservative motion of screw dislocations is a likely candidate since the activation area is consistent with this mechanism.

7.0 CONCLUSIONS

1. It was shown that the transition metal carbides can be made into test specimens that are one-hundred percent dense and of high purity and stoichiometry.
2. The hardness of substoichiometric carbides does not appear to be related to the defect (vacancy) concentration but can be explained in terms of carbon atoms donating electrons to d-metal orbitals in proportion to the carbon concentration.
3. The transition metal carbides were demonstrated to have unusually high strengths and creep resistance at temperatures above 1000°C . The strength persisted up to 0.75 of the melting point.
4. The yield stress is very temperature dependent. The elastic modulus has little temperature dependence indicating that the yield stress has a large effective stress, τ^* , even at temperatures greater than $0.5 T_{\text{mp}}$.
5. The activation area was shown to have a stress dependence consistent with thermally activated deformation mechanisms. The measured activation areas determined from constant strain rate tests were self-consistent with areas determined from

yield stress measurements. The areas were found to be larger than that expected for a Peierls or climb controlled process.

6. Internal stresses determined from stress relaxation measurements were in agreement with the internal stress determined from yield stress experiments after correcting for the temperature dependence of the elastic modulus.
7. The internal stress was found to increase in proportion to the square root of strain during constant strain rate experiments and to remain constant during steady state creep.
8. Extrapolating internal stress measurements as a function of strain back to zero percent strain indicates that the internal stress is not equal to zero at zero percent strain. Therefore $v = k(\tau)^m \neq k(\tau^*)^m$ for polycrystalline material as is assumed⁽⁵⁴⁾ for single crystals at their yield stress.
9. Stress relaxation experiments indicated that the internal stress during steady state creep was not equal to the applied stress and that a stress dependent activation energy was being measured. After correcting the activation energy for steady state creep it was found to be in agreement with the activation energy for self-diffusion.

10. The effective stress, τ^* , was considered to go to zero during logarithmic creep as creep rate approaches zero. The effective stress was not considered to approach zero for steady state creep because τ^* was considered the driving force for creep. The value of the internal stress, τ_i , was determined by τ^* and the rate of dynamic recovery.

8.0 SUGGESTIONS FOR FUTURE WORK

The effect of alloying the carbides with other carbides or intermetallics is a very promising area. Alloying the Group IVB with the Group VB monocarbides should produce a maximum in the hardness according to the model presented in Section 3.3. It has been shown⁽²⁷⁾ that boron addition to TiC and VC greatly increases their strength at elevated temperatures. Venables⁽⁵⁵⁾ has indicated that boron additions may be lowering the stacking fault energy. Martin⁽⁵⁶⁾ has found that the stacking fault energy of sub-stoichiometric TaC may be lowered by the presence of Ta₂C.

APPENDIX A
DERIVATION OF ACTIVATION VOLUME, EQUATION 10, p.62

From Figure 1 A

$$\Delta F = \Delta F_0 - \int_{\gamma_1}^{\gamma_2} F^* dx - \int_0^{\gamma_1} F(x) dx - \int_{\gamma_2}^{\infty} F(x) dx \quad (A 1)$$

Defining

$$\int_{\gamma_1}^{\gamma_2} F^* dx = V^* \gamma^* \quad (A 2)$$

equation A 1 becomes

$$\Delta F = \Delta F_0 - V^* \gamma^* - \int_0^{\gamma_1} F(x) dx - \int_{\gamma_2}^{\infty} F(x) dx \quad (A 3)$$

Taking the derivative of equation A3 with respect to stress yields

$$\begin{aligned} \frac{\partial(\Delta F)}{\partial \gamma^*} &= \frac{\partial(\Delta F_0)}{\partial \gamma^*} - \frac{\partial(V^*)}{\partial \gamma^*} \gamma^* - \frac{\partial \gamma^* V^*}{\partial \gamma^*} \\ &\quad - \frac{\partial}{\partial \gamma^*} \int_0^{\gamma_1} F(x) dx - \frac{\partial}{\partial \gamma^*} \int_{\gamma_2}^{\infty} F(x) dx \end{aligned} \quad (A 4)$$

Defining ΔF_0 to be independent of stress equation A4 can be written as

$$\frac{\partial(\Delta F)}{\partial \gamma^*} = \frac{\partial(V^*)}{\partial \gamma^*} \gamma^* - V^* - \frac{\partial}{\partial \gamma^*} \int_0^{\gamma_1} F(x) dx - \frac{\partial}{\partial \gamma^*} \int_{\gamma_2}^{\infty} F(x) dx \quad (A 5)$$

From Figure A2 it can be seen that

$$\frac{\partial(V^*)}{\partial \gamma^*} \gamma^* = \frac{\partial}{\partial \gamma^*} \int_0^{\gamma_1} F(x) dx - \frac{\partial}{\partial \gamma^*} \int_{\gamma_2}^{\infty} F(x) dx \quad (A 6)$$

Combining equations A5 and A6 yields

$$\frac{\partial (\Delta F)}{\partial \gamma^*} = -V^* \quad (\text{A } 7)$$

Equation 10

$$V^* = kT \frac{\partial \ln v / v_o}{\partial \gamma^*}$$

however is in slight error because it is derived assuming V^* to be independent of stress. V^* determined from strain rate changes is thus the mean value as indicated in Figure

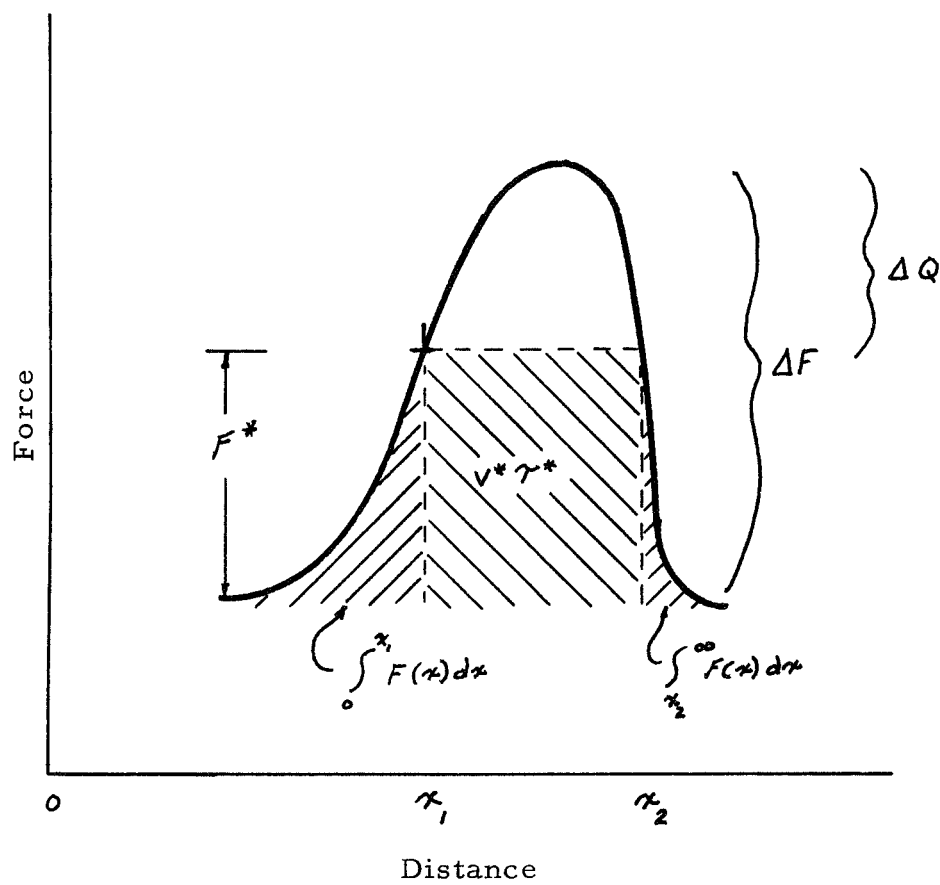


Figure 1 A. Force Versus Distance Curve Showing Relationship Between ΔF , ΔQ and $V^* \gamma^*$

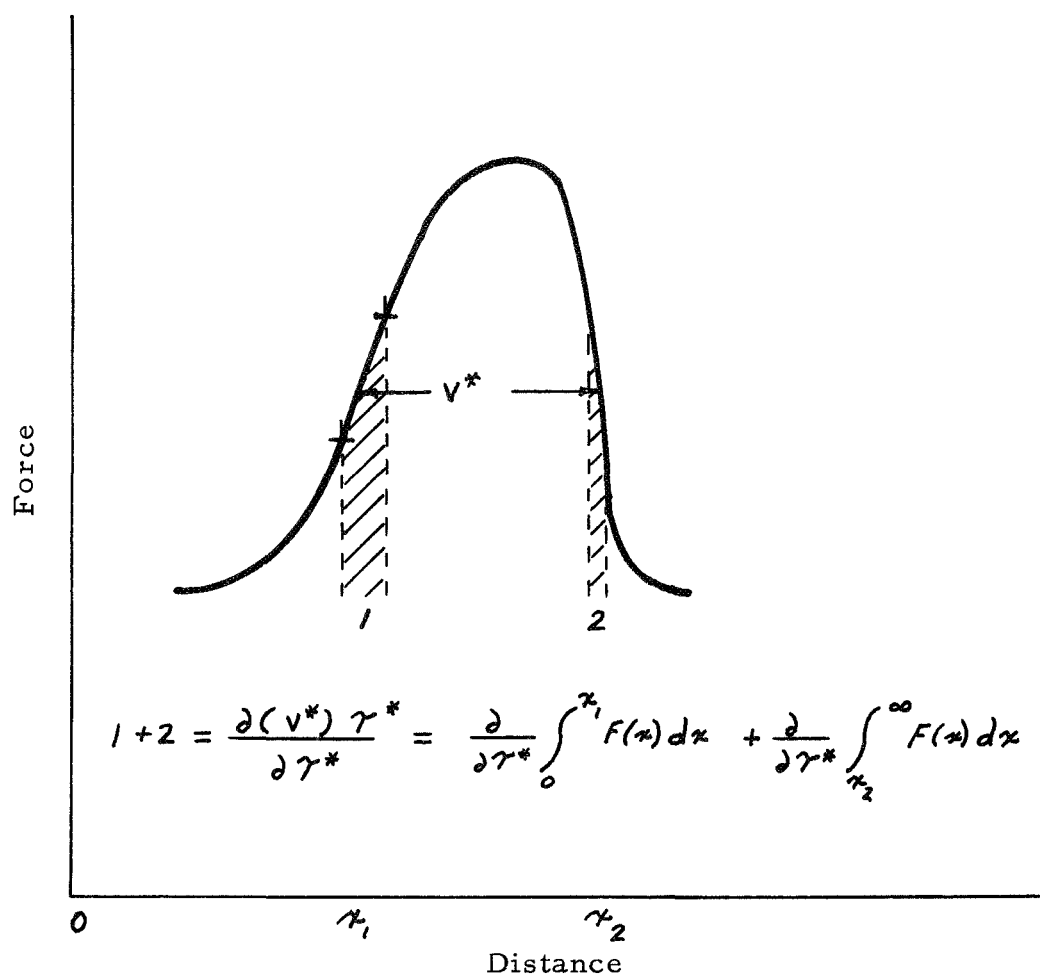


Figure 2 A . Force Versus Distance Curve Showing the Stress Dependence of the Activation Volume

BIBLIOGRAPHY

- 1.. Ryshkewitch, E., J. Am. Ceramic Soc., 36 (1953) 65.
2. Precht, W. and G.E. Hollox, J. of Crystal Growth 3,4 (1968) 818.
3. Adelsberg, L.M. and L.H. Cadoff, Trans. AIME, 239 (1967) 933.
4. Adelsberg, L.M., L.H. Cadoff and J.M. Tobin, Trans. AIME, 236 (1966) 972.
5. Adelsberg, L.M. and L.H. Cadoff, J. Am. Ceramic Soc., 51 (1968) 213.
6. Brizes, W.F., L.H. Cadoff and J.M. Tobin, J. of Nuclear Materials 20 (1966) 57.
7. Brizes, W.F., J. of Nuclear Materials 26 (1968) 227.
8. Rudy, E., C.P. Harmon and C.E. Brukl, Report AFML-TR-62-2, Part 1, Vol. 2, 1965.
9. Sara, R.V., C.E. Lowell and R.T. Dolloff, J. Am. Ceramic Soc., 48 (1965) 243.
10. Sara, R.V., Trans. Met. Soc. AIME, 233 (1965) 1683.
11. Storms, E.K. and R.J. McNeal, J. Phy. Chem. 66 (1962) 1401.
12. Storms, E.K. and N.H. Krikorian, J. Phy. Chem., 64 (1960) 1471.
13. Adelsberg, L.M., L.H. Cadoff and J.M. Tobin, J. Am. Ceramic Soc., 49 (1966) 573.
14. Rudy, E. and D.P. Harmon, Report No. AFML-TR-65-2 Part 1, Vol. V.
15. Brizes, W.F. and J.M. Tobin, J. Am. Ceramic Soc., 50 (1967) 115.
16. Lye, R.G. Atomic and Electronic Structure of Metals, ASM Seminar, Oct. 1966.

17. Brizes, W.F., Space Research Coordination Center Report No. 80, Univ. of Pittsburgh July 1968.
18. Williams, W.S. and R.G. Lye, Union Carbide Corp., ML-TDR-64-25, Part 11, 1965.
19. Santoro, G., Trans. AIME, 227 (1963) 1361.
20. Storms, F.K. and C.P. Kempter, J. of Chem. Phys., 42 (1965) 2043.
21. Fries, R.J. and L.A. Wahman, J. of Am. Ceramic Soc., 50 (1967) 475.
22. Kempter, C.P. and E.K. Storms, J. of Less-Common Metals 13 (1967) 443.
23. Froidevaux, C. and D. Rossier, J. Phys. Chem. Solids, 28 (1967) 1197.
24. de Novion, C.H., R. Lorenzelli and P. Costa, Compt. Rend., 263 (1966) 775.
25. Venables, J.D., D. Kahn and R.G. Lye, Phil. Mag., 18 (1968) 177.
26. Williams, W.S., J. Appl. Phys., 35 (1964) 1329.
27. Hollox, G.E., Mater. Sci. Eng., 3 (1968/69) 121.
28. Williams, W.S. and R.D. Schaal, J. Appl. Phys., 33 (1962) 955.
29. Hollox, G.E. and R.E. Smallman, J. Appl. Phys., 37 (1966) 818.
30. Kelly, A. and D.J. Rowcliffe, J. Amer. Ceram. Soc., 50 (1967) 253.
31. Steinitz, R., Nuclear Applications of Non-Fissionable Ceramics, American Nuclear Society, Illinois, 1966.
32. Santoro, G, Trans AIME, 227 (1963) 1361.
33. Johansen, H. A. and J.G. Cleary, J. Electrochem. Soc., 113 (1966) 378.

34. Williams, W.S., presented at International Conference on Semi-Metallic Compounds, Orsay, France, Sept. 1965, to be published.
35. Chaudhuri, A. R., J. R. Patel and L. G. Rubin, J. Appl. Phys., 33 (1962) 2736.
36. Kelly, A. and D. J. Rowcliffe, Phys. Stat. Sol. 14 (1966) K 29.
37. Norwick, A. S. and E. S. Machlin, J. App. Phy. 18 (1947) 79.
38. Li, J. C. M., Dislocation Dynamics p. 87, A. Rosenfield et. al. (ed.), McGraw-Hill, N. Y. 1967.
39. Conrad, H., L. Hays, G. Schoeck and H. Wiedersich, Acta Met. 9 (1961) 367.
40. Conrad, H., J. of Metals (1964) 582.
41. Conrad, H. and W. Hayes, Trans. ASM 56 (1963) 249.
42. Leipold, M. H. and T. H. Nielsen, J. Am. Ceramic Soc., 47 (1964) 419.
43. Keihn, F. and R. Kebler, J. Less-Common Metals, 6 (1964) 484.
44. Weertman, J., J. Appl. Phys. 28 (1957) 196.
45. Head, A. K., Phil. Mag., 4 (1959) 295.
46. Li, J. C. M., Disc. Faraday Soc., 38 (1964) 138.
47. Hirth, J. P. and J. Lothe, Canadian J. of Phy., 45 (1967) 800.
48. Garofalo, F., Fundamentals of Creep and Creep-Rupture in Metals, Macmillan, 1965.
49. Jonas, J. J., Acta Met., 4 (1969) 397.
50. Speck, D. A., Advanced Ceramic System for Rocket Nozzle Applications, Oct. 31, 1968, Dept. of the Navy, NO 0017-67-C-2406.
51. Conrad, H. and H. Wiedersich, Acta Met., 8 (1960) 128.

52. Brizes, W.F. and E.I. Salkovitz, Scripta Metallurgica, 3(1969)659.
53. LeClaire, A.D., Progress in Metal Physics, 1 (1949) 306.
54. Conrad, H., Acta. Met. 16 (1968) 713.
55. Venable, J., Phys. Stat. Sol. 65 (1961) 1596.
56. Martin, J.L. and B. Jouffrey, Le Journal De Physique 29 (1968) 911.